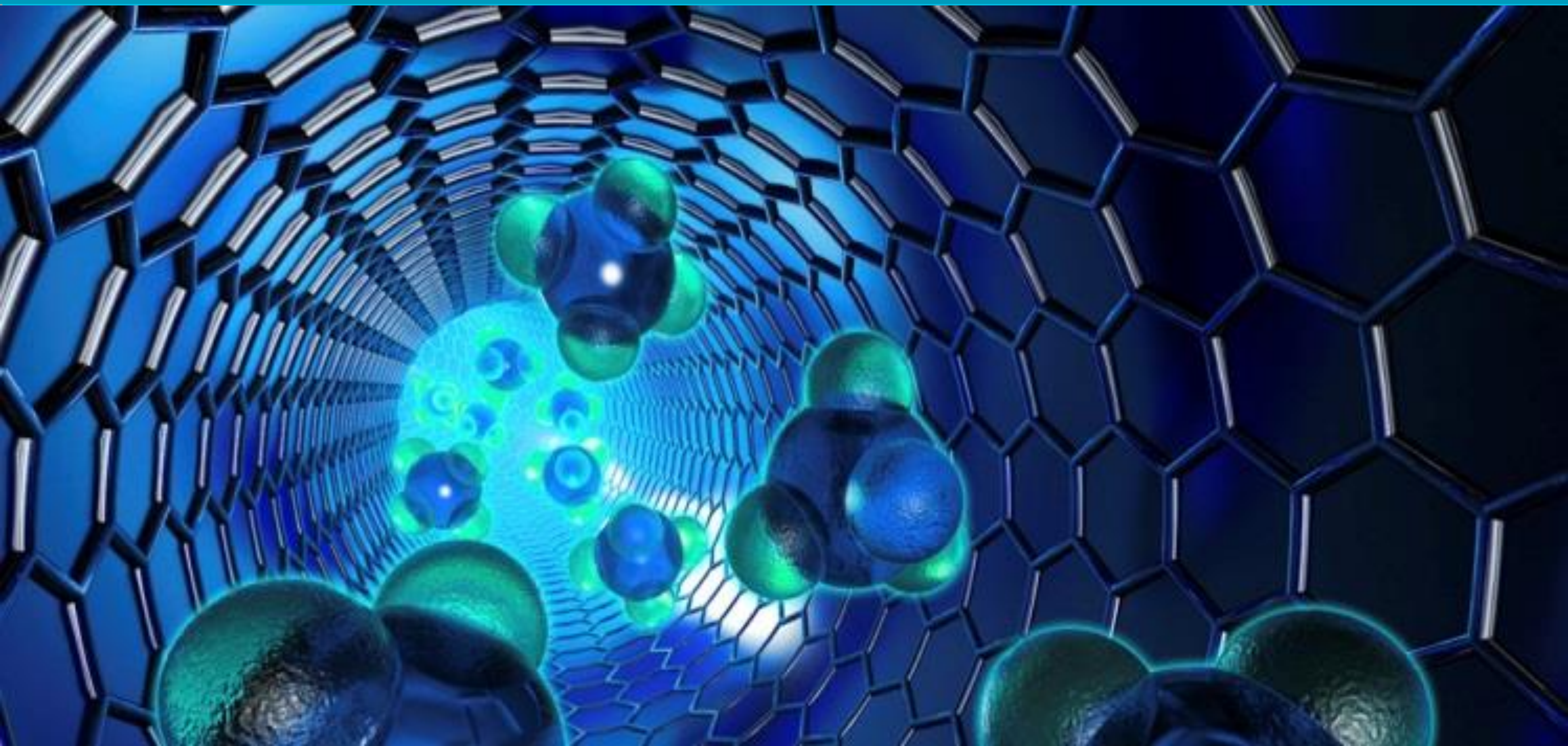


e-ISSN: 2602-277X

International Journal of Chemistry and Technology



Volume:3, Issue:1

28 June 2019

E - Journal

<http://dergipark.org.tr/ijct>

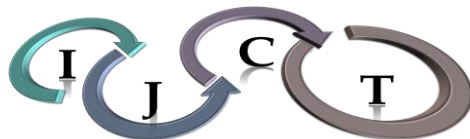


International Journal of Chemistry and Technology

JOURNAL INFO

Journal Name	International Journal of Chemistry and Technology
Journal Initial	IJCT
Journal Abbreviation	Int. J. Chem. Technol.
ISSN (Online)	2602-277X
Year of Launching	2017, August
Editor-in-Chief and Managing Editor	Prof. Dr. Bilal Acemioğlu
Manager of Publication	Assist. Prof. Mehmet Akyüz
Scope and Focus	Chemistry, Material Science, Technology
Review Type	Peer Review Double-Blinded
Ethical Rules	Plagiarism check, copyright agreement form, conflict of interest, ethics committee report
Access Type	Open Access
Publication Fee	Free
Article Language	English
Frequency of Publication	Biannually
Publication Issue	June, December
Publisher	Prof. Dr. Bilal Acemioğlu
Web Page	http://dergipark.org.tr/ijct
Contact E-mail address	ijctsubmission@gmail.com, ijctsubmission@yahoo.com
Contact Address and Executive address	Kilis 7 Aralik University, Faculty of Science and Arts, Department of Chemistry, 79000, Kilis
Contact Telephone	90 5535983054 (Editor-in-Chief), 90 530 3645222 (Manager of Publication), 90 532233 17 38 (Secretary)
Publication Date	28/12/2018
Technical Editor	Assist. Prof. Dr. Evrim Baran Aydın
Spelling Editor	Dr. Oğuzhan Koçer, MSc. Rabia Acemioğlu
Language (Grammar) Editor	Assit. Prof. Dr. Muhittin Kulak, Assist. Prof. Dr. Muhammet Karaman, Msc. Lawali Yabo Dambagi
Secretary	Dr. Oğuzhan Koçer, MSc. Rabia Acemioğlu

All detailed information including instructions for authors, aim and scopes, ethical rules, manuscript evaluation, indexing info, and manuscript template etc. can be found on the main web page of IJCT (<http://dergipark.org.tr/ijct>).



International Journal of Chemistry and Technology

Volume: 3, Issue: 1, 28 June 2019

Founder of IJCT

Prof. Dr. Bilal Acemioğlu

EDITORIAL BOARD

Editor-in-Chief

Prof. Dr. Bilal Acemioğlu

(Physical Chemistry, Kilis 7 Aralık University, Kilis, Turkey)

Associate Editors

Prof. Dr. İbrahim Demirtaş
(Organic Chemistry and Phytochemistry,
Çankırı Karatekin, University, Çankırı, Turkey)

Prof. Dr. Yuh-Shan Ho
(Chemical and Environmental Engineering,
Asia University, Taichung City, Taiwan)

Prof. Dr. M. Hakkı Alma
(Material Science and Technology,
K.Maraş Sütçü İmam/Iğdır University, Turkey)

Prof. Dr. Yahya Güzel
(Theoretical Chemistry and Polymer Chemistry,
Erciyes University, Kayseri, Turkey)

Prof. Dr. Ekrem Köksal
(Biochemistry, Erzincan Binali Yıldırım University,
Erzincan, Turkey)

Prof. Dr. Mustafa Arık
(Physical Chemistry, Atatürk University,
Erzurum, Turkey)

Prof. Dr. Fevzi Kılıçel
(Analytical Chemistry, Karamanoğlu Mehmet
Bey University, Karaman, Turkey)

Prof. Dr. Mehmet Sönmez
(Inorganic Chemistry, Gaziantep University,
Gaziantep, Turkey)



International Journal of Chemistry and Technology

Advisory Editorial Board

Prof. Dr. Harun Parlar
(Technical University of Munich, München,
Germany)

Prof. Dr. Shaobin Wang
(Curtin University, Perth, Australia)

Prof. Dr. Gelu Bourceanu
(Alexandru Ioan Cuza University, Romania)

Prof. Dr. Jon-Bae Kim
(College of Health Sciences, South Korea)

Prof. Dr. Rashid Ahmad
(University of Malakand, Chakdara, Pakistan)

Prof. Dr. Guang-Jie Zhao
(Beijing Forestry University, Beijing, China)

Prof. Dr. Jaine H. Hortolan Luiz
(Federal University of Alfenas, Unifal-MG, Brazil)

Prof. Dr. Papita Das
(Jadavpur University, Jadavpur, India)

Prof. Dr. Vagif Abbasov
(Nef-Kimya Prosesleri Institutu, Baku, Azerbaijan)

Prof. Dr. Atiqur Rahman
(Islamic University, Kushita, Bangladesh)

Prof. Dr. Mika Sillanpaa
(LUT Lappeenranta University of Technology,
Lappeenranta, Finland)

Prof. Dr. Salah Akkal
(University of Mentouri Consatntine,
Consatntine, Algeria)

Prof. Dr. Gilbert Kapche Deccaux
(University of Yaounde I, Yaounde, Cameroon)

Prof. Dr. Anatoli Dimoglu
(Düzce University, Düzce, Turkey)

Prof. Dr. Ahmet Çakır
(Kilis 7 Aralik University, Kilis, Turkey)

Prof. Dr. M. Salih Ağırtaş
(Yüzüncü Yıl University, Van, Turkey)

Prof. Dr. Nurullah Saraçoğlu
(Atatürk University, Erzurum, Turkey)

Prof. Dr. Rahmi Kasımoğulları
(Dumlupınar University, Kütahya, Turkey)

Prof. Dr. Ahmet Baysar
(Inonu University, Malatya, Turkey)

Prof. Dr. Hamdi Temel
(Dicle University, Diyarbakır, Turkey)

Prof. Dr. Ö. İrfan Küfrevioğlu
(Atatürk University, Erzurum, Turkey)

Prof. Dr. Ömer Şahin
(Siirt University, Siirt, Turkey)

Prof. Dr. Mehmet Çiftçi
(Bingöl University, Bingöl, Turkey)

Prof. Dr. Mehmet Uğurlu
(Sıtkı Kocman University, Muğla, Turkey)

Prof. Dr. Şükrü Beydemir
(Anadolu University, Eskişehir, Turkey)

Prof. Dr. Ramazan Solmaz
(Bingol University, Bingöl, Turkey)

Prof. Dr. Mahfuz Elmastaş
(Health Sciences University, İstanbul, Turkey)

Prof. Dr. Mehmet Doğan
(Balıkesir University, Balıkesir, Turkey)

Prof. Dr. Giray Topal
(Dicle University, Diyarbakır, Turkey)

Prof. Dr. Birgül Yazıcı
(Cukurova University, Adana, Turkey)



International Journal of Chemistry and Technology

Advisory Editorial Board

Prof. Dr. Mehmet Muhtar Kocakerim
(Çankırı Karatekin University, Çankırı, Turkey)

Prof. Dr. Murat Alanyalıoğlu
(Atatürk University, Erzurum, Turkey)

Prof. Dr. T. Abdulkadir Çoban
(Erzincan Binali Yıldırım University, Erzincan, Turkey)

Prof. Dr. İsmet Kaya
(18 Mart University, Çanakklae, Turkey)

Prof. Dr. Barbaros Nalbantoğlu,
(Yıldız Technical University, İstanbul, Turkey)

Prof. Dr. Ömer Işıldak
(Gaziosmanpaşa University, Tokat, Turkey)

Prof. Dr. Halim Avcı
(Kilis 7 Aralık University, Kilis, Turkey)

Prof. Dr. Ahmet Tutar
(Sakarya University, Sakarya, Turkey)

Prof. Dr. Duygu Ekinci
(Atatürk University, Erzurum, Turkey)

Prof. Dr. Metin Bülbül
(Dumlupınar University, Kütahya, Turkey)

Assoc. Prof. Dr. Şenay Şimşek
(North Dakota State University, Fargo, USA)

Assoc. Prof. Chin-Hung Lai (Chung Shan
Medical University, Taiwan)

Assoc. Prof. Niyaz M. Mahmoodi,
(Institute for Color Science and Technology,
Tehran, Iran)

Assoc. Prof. Dr. Mahjoub Jabli
(University of Monastir, Monastir, Tunisia)

Assoc. Prof. Dr. Ali Kara
(Uludağ University, Bursa, Turkey)

Assoc. Prof. Dr. Metin Açıkyıldız
(Kilis 7 Aralık University, Kilis, Turkey)

Assoc. Prof. Dr. Muhammet Köse
(Sütçü İmam University, K.Maraş, Turkey)

Assoc. Prof. Dr. Mustafa Karataş
(Aksaray University, Aksaray, Turkey)

Assoc. Prof. Dr. Serhan Uruş
(Sütçü İmam University, K.Maraş, Turkey)

Assoc. Prof. Dr. Murat Saraçoğlu
(Erciyes University, Kayseri, Turkey)

Assoc. Prof. Dr. Murat Sadıkoğlu
(Gaziosman Paşa University, Tokat, Turkey)

Assoc. Prof. Dr. Mustafa Özdemir
(Süleyman Demirel University, Isparta, Turkey)

Assist. Prof. Dr. Mutasem Z. Bani-Fwaz
(King Khalid University, Asir-Abha, Saudi Arabia)

Assist. Prof. Masood Ayoub Kaloo
(Govt. Degree College Shopian, J &K, India)

Dr. Zineb Tribak
(Sidi Mohamed Ben Abdellah University, Fez
Morocco)

Assist. Prof. Dr. Bakhtiyor Rasulev
(North Dakota State University, Fargo, USA)

Dr. Ramadan E. Ashery
(Damanhour University, Egypt)

Dr. Sameer Ahmed Awad
(University of Anbar, Ramadi, Iraq)



International Journal of Chemistry and Technology

Reviewers for December 2019, Vol: 3, Issue: 1

- | | |
|---|--|
| Prof. Dr. Muhammet Kasım Şener
(Yıldız Technical University, İstanbul, Turkey) | Prof. Dr. Zümriye Aksu
(Hacettepe University, Ankara, Turkey) |
| Prof. Dr. İbrahim Demirtaş
(Çankırı Karatekin University, Çankırı, Turkey) | Prof. Dr. Kani Arıcı
(Kilis 7 Aralık University, Kilis, Turkey) |
| Prof. Dr. Ali Erdoğan
(Yıldız Technical University, İstanbul, Turkey) | Prof. Dr. Mustafa Teke
(Sıtkı Koçman University, Muğla, Turkey) |
| Prof. Dr. Ramazan Erenler
(Tokat Gaziosmanpaşa University, Tokat, Turkey) | Assoc. Prof. Dr. Şerife Yalçın
(Harran University, Şanlıurfa, Turkey) |
| Prof. Dr. Muhammet Muhtar Kocakerim
(Çankırı Karatekin University, Çankırı, Turkey) | Assoc. Prof. Dr. Metin Açıkyıldız
(Kilis 7 Aralık University, Kilis, Turkey) |
| Assoc. Prof. Dr. Mustafa Özdemir
(Süleyman Demirel University, Isparta, Turkey) | Assoc. Prof. Dr. Murat Saraçoğlu
(Erciyes University, Kayseri, Turkey) |
| Assoc. Prof. Dr. Reşit Yıldız
(Mardin Artuklu University, Mardin, Turkey) | Assoc. Prof. Dr. Nizamettin Demirkıran
(İnönü University, Malatya, Turkey) |
| Assoc. Prof. Dr. Başak Doğru Mert
(Adana Bilim ve Teknoloji University, Adana, Turkey) | Assist Prof. Dr. Evrim Baran Aydın
(Kilis 7 Aralık University, Kilis, Turkey) |
| Assist Prof. Dr. Mutasem Z. Bani-Fwaz
(King Khalid University, Saudi Arabia) | Assist. Prof. Dr. Mehmet Akyüz
(Kilis 7 Aralık University, Kilis, Turkey) |
| Dr. Neşe Keklikçioğlu Çakmak
(Sivas Cumhuriyet University, Sivas, Turkey) | Dr. İbrahim Halil Gecibesler
(Bingöl University, Bingöl, Turkey) |



International Journal of Chemistry and Technology

TABLE OF CONTENTS

Research Articles	Pages
1. Investigation of theoretical properties of 1-Acetyl-3-(<i>p</i> -methylbenzyl)-4-(3-methyl-2-thienylmethyleneamino)-4,5-dihydro-1 <i>H</i> -1,2,4-triazol-5-one molecule (1-Asetil-3-(<i>p</i> -metilbenzil)-4-(3-metil-2-thienilmetilenamino)-4,5-dihidro-1 <i>H</i> -1,2,4-triazol-5-ön molekülünün teorik özelliklerinin incelenmesi) Gül Kotan, Bedrettin Savaş, Haydar Yüksek	1-10
2. Total phenolic and flavonoid contents and antioxidant capacity of home-made Isabella grape (<i>Vitis labrusca</i> L.) vinegar (Ev yapımı Isabella üzümü (<i>Vitis labrusca</i> L.) sirkesinin toplam fenolik ve flavonoid içerikleri ve antioksidan kapasitesi) Sinem Aydın, Cavidan Demir Gökışık	11-16
3. A Corrosion Study: Use of Thionine dye having structurally metachromatic influence (Bir korozyon çalışması: Yapısal olarak metakromatik etkiye sahip olan tiyonin boyasının kullanılması) Demet Özkır	17-25
4. The theoretical investigation of HOMO, LUMO, thermophysical properties and QSAR study of some aromatic carboxylic acids using HyperChem programming (HyperChem programı kullanarak bazı aromatik karboksilik asitlerin HOMO, LUMO, termoplastik özellikleri ve QSAR incelemesinin teorik araştırılması) Ajoy Kumer, Md Nuruzzaman Sarker, Sunanda Paul	26-37
5. A study on leaching kinetics of chalcopyrite in $\text{KNO}_3 + \text{H}_2\text{SO}_4$ medium (Kalkopiritin $\text{KNO}_3 + \text{H}_2\text{SO}_4$ ortamındaki liçing kinetiği üzerine bir çalışma) Harun Dikme, Soner Kuşlu, Özlem Karagöz	38-45
6. Synthesis of tetrakis (4-(2-phenylprop-2-yl) phenoxy) substituted phthalocyanines using a new practical method (Yeni pratik bir yöntem kullanarak tetrakis (4-(2-fenilprop-2-il) fenoksi) süstitüentli ftalosiyanınların sentezi) Mehmet Salih Ağirtaş, Cihan Durmuş, Beyza Cabir	46-51
7. Optimization, isotherm and kinetics studies of the adsorption of azo dyes on eggshell membrane (Yumurta kabuğu zarı üzerine azo boyaların adsorpsiyonunun optimizasyon, izoterm ve kinetik incelemeleri) Ayşe Dinçer, Mervecan Sevildik, Tülin Aydemir	52-60
8. Stress behaviours of viscoelastic flow around square cylinder (Kare silindir etrafındaki viskoelastik akışın stres davranışları) Guler Bengusu Tezel, Kerim Yapıcı, Yusuf Uludag	61-66

Short Communication	Pages
9. Enhancing the adsorption of disinfection by-products onto activated carbon using TiO ₂ nanoparticles (TiO ₂ nanopartikülleri kullanılarak dezenfeksiyon yan ürünlerinin aktif karbon üzerine adsorpsiyonunun artırılması) Rafat Moustafa, Ahmed Hesham	67-71
10. Rapid isolation of rosmarinic acid from <i>Ocimum basilicum</i> using flash chromatography (Flash kromatografi kullanarak Reyhan bitkisinden rozmarinik asitin hızlı izolasyonu) Hüseyin Akşit, Mehmet Keçeci, İbrahim Demirtaş, Nusret Genç	72-76



Investigation of theoretical properties of 1-Acetyl-3-(*p*-methylbenzyl)-4-(3-methyl-2-thienylmethyleneamino)-4,5-dihydro-1*H*-1,2,4-triazol-5-one molecule

Gül KOTAN^{1*}, Bedrettin SAVAŞ¹, Haydar YÜKSEK²

at end page

¹Kars Vocational School, Kafkas University, Kars, 36100, Turkey

²Department of Chemistry, Faculty of Science and Letters, Kafkas University, Kars, 36100, Turkey

Received: 24 October 2018; Revised: 25 December 2018; Accepted: 09 January 2019

*Corresponding author e-mail: gulkemer@hotmail.com

Citation: Kotan, G.; Savaş, B.; Yüksek, H. *Int. J. Chem. Technol.* 2019, 3 (1), 1-10.

ABSTRACT

In this study, firstly, 1-acetyl-3-(*p*-methylbenzyl)-4-(3-methyl-2-thienylmethyleneamino)-4,5-dihydro-1*H*-1,2,4-triazol-5-one molecule was optimized by using the B3LYP/DFT631G (d) and HF/631G (d) basis sets. Then, the veda4f program was used in defining of IR data theoretically. IR (infrared) vibrational frequency values with two different basis sets of molecule was calculated in gas phase and multiplied by adjustment scale factors. Infrared spectra of molecule according to these values obtained were formed. Furthermore, ¹H-NMR and ¹³C-NMR isotropic shift values were calculated by GIAO method. Experimental and theoretical values of analyzed molecule were inserted into the graphic according to equation of $\delta_{exp} = a + b \cdot \delta_{calc}$. The standard error values were found via SigmaPlot program with regression coefficient of *a* and *b* constants. Finally, bond angles, bond lengths, mulliken atomic charges, HOMO-LUMO energy, $E_{LUMO}-E_{HOMO}$ energy gap (ΔE), electronegativity (χ), electron affinity (*A*), global hardness (η), softness (σ), ionization potential (*I*), total energy of the molecule, dipole moment and thermodynamic properties were calculated with Gaussian 09W program.

Keywords: Gaussian G09W, Veda4f, HOMO-LUMO, GIAO

1-Asetil-3-(*p*-metilbenzil)-4-(3-metil-2-thienilmetilenamino)-4,5-dihidro-1*H*-1,2,4-triazol-5-on molekülünün teorik özelliklerinin incelenmesi

ÖZ

Bu çalışmada, öncelikle, 1-Asetil-3-(*p*-metilbenzil)-4-(3-metil-2-thienilmetilenamino)-4,5-dihidro-1*H*-1,2,4-triazol-5-on molekülü B3LYP/DFT631G (d) and HF/631G (d) temel setleri kullanılarak optimize edilmiştir. Sonra, Veda 4f programı teorik olarak IR verilerini belirlemede kullanılmıştır. Molekülün iki farklı temel seti ile IR (infrared) titreşim frekans değerleri gaz fazında hesaplanmış ve uygun skala faktörleri ile çarpılmıştır. Elde edilen bu değerlere göre molekülün infrared spektrumları çizilmiştir. Ayrıca, ¹H- ve ¹³C-NMR isotropik kayma değerleri GIAO metoduna ile hesaplanmıştır. Analiz edilen molekülün deneysel ve teorik değerleri $\delta_{exp} = a + b \cdot \delta_{calc}$ eşitliğine göre grafiğe geçirilmiştir. Standart hata değerleri *a* ve *b* sabitlerinin regresyon katsayısı ile SigmaPlot programı kullanılarak bulunmuştur. Son olarak, bağ açıları, bağ uzunlukları, mulliken atomik yükleri, HOMO-LUMO enerjisi, $E_{LUMO}-E_{HOMO}$ kapasitesi (ΔE_g), elektronegatiflik (χ), elektron yoğunluğu (*A*), global sertlik (η), yumuşaklık (σ), iyonizasyon potansiyeli (*I*), molekülün toplam enerjisi, dipol moment ve termodinamik özellikleri Gaussian 09W programı ile hesaplanmıştır.

Anahtar Kelimeler: Gaussian G09W, Veda4f, HOMO-LUMO, GIAO.

1. INTRODUCTION

Schiff bases are of the fundamental compounds for organic chemistry. These compounds include -C=N- (azomethine group). They are, generally, synthesized by condensation of active -C=O- and -NH₂ containing compounds.¹ Their derivatives of 1,2,4-triazoles have

also been found to possess pharmacological activities.²⁻⁵ When heteroatoms such as sulfur, oxygen, nitrogen are added the structure of the Schiff base compounds, the biological activity increases.⁶ The most known biological activities of them were anti-viral activity,⁷ anti-fungal,⁸ anti-oxidant,⁹ anti-inflammmatory,¹⁰ anti-bacterial,¹¹ anti-tumor,¹² anti-cancer,^{13,14} trypano-

DOI: <http://dx.doi.org/10.32571/ijct.474279>

E-ISSN:2602-277X

somal,¹⁵ anti-proliferative¹⁶ and antibiotics.¹⁷ In the past years, by increases and trends in development of computational chemistry, theoretically properties of Schiff bases have been investigated. Quantum chemical calculations have been used commonly to theoretically estimate the structure, electronic properties, thermodynamics, spectroscopy of molecular systems. The aim of this study is to compare the calculated theoretical values with experimental values and to determine which of the DFT and HF methods close to experimental values.

2. MATERIALS AND METHODS

2.1. Computational Details

The quantum chemical calculations provide support for spectroscopic studies and experimental structures.¹⁸⁻²³ Firstly, the density functional theoretical (DFT) and Hatree Fock (HF) calculations of compounds were optimized at the Becke-Lee-Parr hybrid exchange correlation three-parameter functional (B3LYP) level with standard 6-31G(d) basis set.²⁴ All calculations reported in this work were carried out with the Gaussian 09 program.²⁵ Then, from the most stable structure of the optimized molecule, electronegativity (χ), Mulliken charges, the lowest unoccupied molecular orbital (LUMO) and the highest occupied molecular orbital (HOMO), bond lengths, electron affinity (A), global hardness (η), softness (σ), ionization potential (I), chemical potential (Pi), Nucleophilic index (IP), electrophilic index(ω), total energy of the molecule, thermodynamics properties (thermal energies (E), thermal capacity (CV), entropy (S), dipole moments, $E_{\text{LUMO}}-E_{\text{HOMO}}$ energy gap (ΔE_g) were calculated with HF/631G (d) and DFT631G (d) basis sets. Moreover, IR data were calculated theoretically using the veda4f program.²⁶ Experimental data were obtained from the literature.²⁷ The calculated and the experimental data were compared with accuracy of values found by regression analysis. Theoretical IR data are multiplied with chosen scala factors.²⁸ The data obtained according to DFT and HF method are formed using theoretical infrared spectrum. Finally, ¹H-NMR and ¹³C-NMR isotropic shift values were calculated with the method of gauge including atomic orbital GIAO²⁵ using the program package Gaussian G09. Experimental and theoretical parameters of investigated molecules were inserted into the graphic according to the equation of $\delta_{\text{exp}} = a + b \cdot \delta_{\text{calc}}$. The standard error and regression coefficient (a, b) were found by SigmaPlot program.

2.1.1. Optimized geometries

1-Acetyl-3-(*p*-methylbenzyl)-4-(3-methyl-2-thienylmethyl- hyleneamino)-4,5-dihydro-1*H*-1,2,4-triazol-5-one was optimized by means of DFT(B3LYP)/HF methods with 6-31G(d) basis set. The chemical formula

and the optimized geometric structure of molecule is shown in Figures 1 and 2.

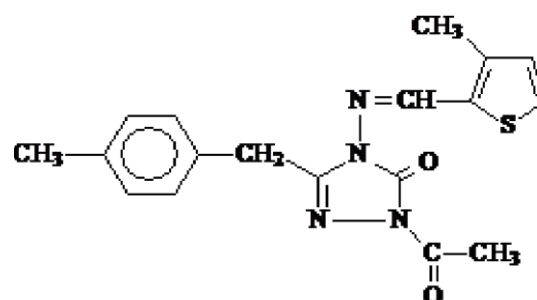


Figure 1. The chemical formula of the molecule.

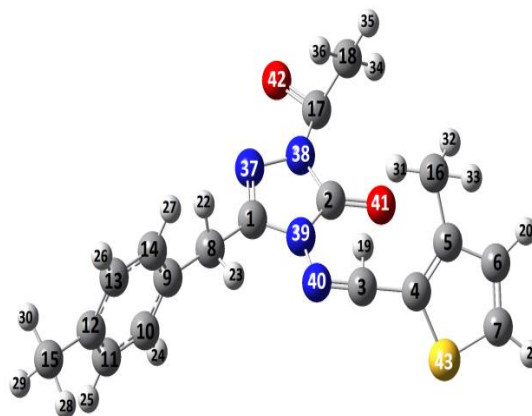


Figure 2. The optimized structure of the molecule.

2.2. The R² values of the compound

The experimental and calculated results are summarized in Table 1. A linear correlation in the experimental and theoretical values (proton and carbon chemical shifts ratios) was observed and shown in Figure 3. There is such a relationship between R-values of target compound: DFT 6-31G(d) DMSO: ¹H: 0,9978, ¹³C: 0,9974, HF 6-31G(d)DMSO: ¹H: 0,8212 ¹³C: 0,8387 (Table 2).

2.3. FT-IR study of molecule

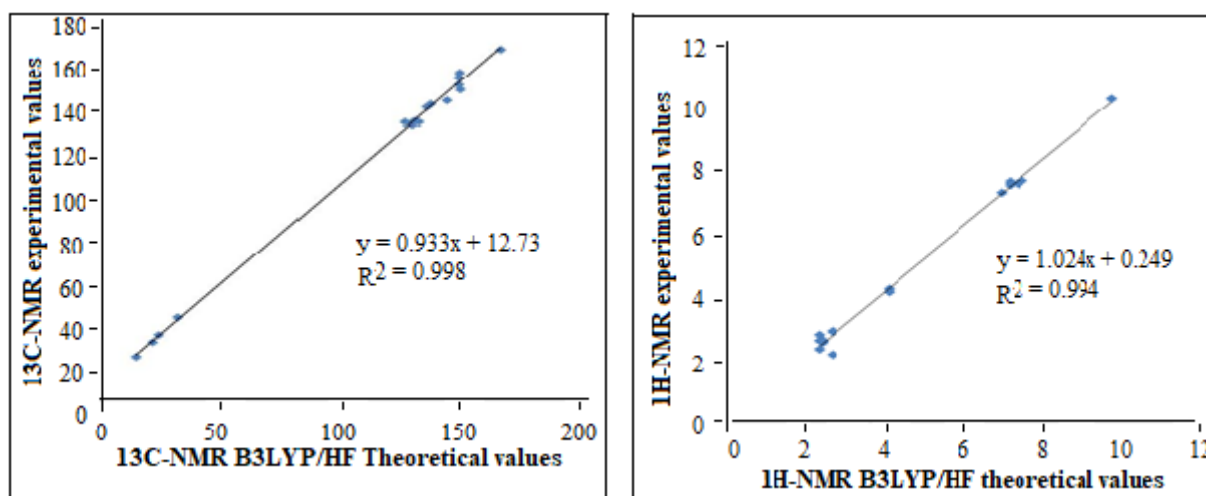
Theoretical IR data were calculated from veda4f programme, and scala vibration values were obtained. Theoretical IR data were multiplied with appropriate scala factors respectively 0.9613, 0.8929 for DFT/ HF 631G(d) basis sets. The data was found positively. The structure was stable according to the obtained result. IR spectra were drawn with data obtained according to HF and DFT methods. Theoretical IR values were compared with experimental IR values and listed in Table 3.

Table 1. ^{13}C and ^1H -NMR (DMSO) isotropic chemical shifts (δ/ppm)

No	Exp.	DFT/dmso	Differ/DFT	HF/dmso	Differ/HF	No	Exp.	DFT/dmso	Differ/DFT	HF/dmso	Differ/HF
C1	148,59	154,34	-5,75	146,83	1,76	H19	9,73	10,34	-0,61	9,57	0,16
C2	149,21	156,68	-7,47	150,19	-0,98	H20	6,90	7,35	-0,45	6,84	0,06
C3	149,47	148,59	0,88	146,09	3,38	H21	7,42	7,73	-0,31	7,45	-0,03
C4	143,88	143,55	0,33	126,60	17,28	H22	4,05	4,37	-0,32	3,48	0,57
C5	148,87	150,89	-2,02	143,76	5,11	H23	4,05	4,27	-0,22	3,60	0,45
C6	132,07	133,76	-1,69	123,56	8,51	H24	7,11	7,59	-0,48	7,58	-0,47
C7	135,41	140,55	-5,14	133,51	1,90	H25	7,32	7,62	-0,30	7,11	0,21
C8	31,55	43,35	-11,80	27,56	3,99	H26	7,32	7,67	-0,35	7,34	-0,02
C9	126,25	133,66	-7,41	126,40	-0,15	H27	7,11	7,70	-0,59	7,58	-0,47
C10	131,02	134,25	-3,23	127,38	3,64	H28	2,29	2,93	-0,64	2,14	0,15
C11	129,25	132,85	-3,60	124,78	4,47	H29	2,29	2,48	-0,19	1,69	0,60
C12	137,04	141,85	-4,81	134,32	2,72	H30	2,29	2,75	-0,46	2,19	0,10
C13	129,36	132,97	-3,61	125,52	3,84	H31	2,37	2,69	-0,32	2,07	0,30
C14	129,79	133,96	-4,17	126,61	3,18	H32	2,37	2,76	-0,39	2,04	0,33
C15	21,04	31,80	-10,76	18,23	2,81	H33	2,37	2,75	-0,38	1,99	0,38
C16	14,13	24,96	-10,83	12,46	1,67	H34	2,62	3,03	-0,41	2,35	0,27
C17	166,46	167,50	-1,04	160,67	5,79	H35	2,62	3,05	-0,43	2,36	0,26
C18	23,55	35,12	-11,57	22,90	0,65	H36	2,62	2,31	0,31	1,82	0,80

Table 2. The correlation values for chemical shifts of the molecule

	^{13}C				^1H			
	R	S. error	a	b	R	S. error	a	b
DFT	0,9974	3,0761	2,6820	0,01859	0,9978	2,6352	2,1076	0,0158
HF	0,8387	1,5023	0,9695	0,15994	0,8212	1,5816	0,9775	0,1756

**Figure 3.** The correlation graphs for B3LYP/HF 631G(d) chemical shifts of the molecule.

2.4. Molecular geometry

The molecular geometric parameters such as bond lengths, bond angles, Mulliken atomic charges were calculated by using the HF and DFT/B3LYP methods with 6-31G(d) basis sets, dipole moments, total energies, and the obtained data are precondition in Tables 4-8. According to these results, the N37-N38, N37-C1, C2-O41, N38-C2, N39-C1, N39-C2 bond lengths in the triazole ring are calculated with DFT/HF 6-31G(d) methods 1.39/1.38, 1.29/1.26,

1.22/1.19, 1.39/1.37, 1.39/1.38, 1.40/1.37 Å (Table 4). In the literature, the N=C, N-N, C=O bond lengths are measured as 1.280, 1.404, 1.212 Å.^{29, 30} The calculated C9-C10, C10-C11, C11-C12, C12-C13, C13-C14 bond lengths of benzene rings in this compound are [1.39/1.38 Å], [1.39/1.38 Å], [1.40/1.38 Å], [1.39/1.39 Å] and [1.39/1.38 Å], respectively. The Ar(C)-Ar(C) bond lengths of benzene rings are generally observed at 1.34-1.53 Å in the literature.^{31,32} The calculated C-H bond lengths of the compound are about 1.09, and the C-H bond lengths in the literature is 1.09 Å.^{31,32} Also, the calculated N38-C2 bond length in 1,2,4-triazole-5-one ring is [1.39/1.37 Å]. It has been recorded to have bond

DOI: <http://dx.doi.org/10.32571/ijct.474279>

E-ISSN:2602-277X

length between single bonded N-N and double bonded N=N due to resonance. The same bond length in the literature is recorded between 1.29-1.47 Å.^{31,32} When compared with the bond lengths in the literature, the results show that the molecular structure is very well. The Mulliken atomic charges³³ were calculated by using the Hartree Fock (HF) and DFT/B3LYP methods with 6-

31G(d) basis sets. The electronegative oxygen (O) and nitrogen (N) atoms have negative atomic charge values. The carbon atoms surrounded by electronegative atoms have positive atomic charge values. The C1 atom surrounded by two electronegative atoms (N37, N39) and C2 atom which is surrounded by three electronegative atoms (N38, N39, O41) have the highest positive charges values. All hydrogen atoms of the compound have positive atomic charge values (Table 6).

Table 3. Significant vibrational frequencies (cm⁻¹)

Vibration Types	scaled dft	scaled hf	Vibration Types	scaled dft	scaled hf
τ CCCC(19), τ NCCN(15), τ CNNC(39)	10	4	δ HCH(11), τ HCCC(51), τ CCCC(10)	835	854
τ HCCC(70)	15	7	δ HCH(21), τ HCCN(59)	845	887
τ CCCC(17), τ CCNN(31), τ NCCN(29)	21	18	ν NN(12), ν NC(15), δ NNC(19)	855	892
δ CCN(41), δ CNN(30), δ CCC(12)	28	24	ν NN(27), δ HNN(10), τ HCCN(28)	960	1005
τ HCCN(68), τ CNNC(17)	37	25	ν CC(16), δ HCS(34), δ HCC(31)	976	1012
τ CNCN(20), τ CCCC(14)	40	34	ν CC(11), ν NC(20), ν NN(16), δ CNN(15)	977	1016
τ CNNC(11), τ CCCC(17), τ CNNC(24)	56	53	δ HCS(13), δ HCC(14), δ CCC(13)	980	1022
δ CNN(12), δ CCC(17), δ NNC(22)	71	66	ν NC(39)	1011	1029
δ CCN(16), δ CCC(19)	77	87	ν NN(22), δ CNN(24)	1022	1038
δ CCC(11), τ CCCC(15), τ NNCN(11)	96	108	δ HNN(65)	1024	1048
τ CCCC(12), τ CCCC(19), τ NCCN(30)	120	125	τ HCCC(62)	1034	1049
τ HNNC(20), τ CNNC(17), τ NCNN(16)	133	143	ν CC(12), δ HCS(14), δ HCC(10), δ HCH(23)	1040	1052
δ CCN(38), δ CCC(34)	134	167	ν CC(14), δ HCH(56)	1063	1071
τ CCCC(10), τ CCNN(29), τ SCCC(21),	145	174	δ HCH(56)	1075	1080
δ OCN(18), δ CNN(10), δ NNC(13), δ CCC(15)	188	197	ν CC(16), ν NC(12), δ HCH(12)	1111	1086
δ CCC(24)	193	202	δ HCH(77), τ HCCN(22)	1115	1099
τ HNNC(59), τ ONNC(10)	200	210	ν CC(25), δ HCH(19)	1129	1105
τ CCCC(17), τ CCNN(12), τ SCCC(49)	219	215	ν NN(18), δ NNC(10)	1131	1119
ν CC(21), δ SCC(29)	230	231	ν OC(10), ν CC(10), δ CNN(27), ν NC(21)	1147	140
ν NC(12), δ OCN(37), δ NNC(10), δ CCN(13)	244	250	ν SC(44), δ SCC(26)	1149	1146
ν NN(10), ν CC(21), δ CNN(29)	252	256	τ HCCS(82), τ SCCC(10)	1152	1155
τ HCCS(15), τ CCCC(30), τ SCCC(10)	305	303	ν CC(12), δ HCS(10), δ CCC(17), τ HCCC(17)	1177	1178
τ HNNC(12), τ NCNN(54), τ CNNC(11)	312	304	τ HCNN(93)	1179	1189
ν SC(22), δ CCC(17)	328	327	δ HCH(12), δ NNC(15), τ HCCN(36)	1201	1197
ν CC(10), ν SC(14), δ CCC(24), δ SCC(16)	337	349	ν CC(10), τ HCCC(35)	1236	1203
τ HCCS(80)	358	379	δ HCH(11), τ HCCC(51), τ CCCC(10)	1244	1210
τ ONNC(81)	386	382	δ HCH(21), τ HCCN(59)	1265	1254
ν NN(18), δ NNC(10)	397	405	ν NN(12), ν NC(15), δ NNC(19)	1269	1256
ν OC(10), ν NC(21), ν CC(10), δ CNN(27)	407	429	ν NN(27), δ HNN(10), τ HCCN(28)	1273	1265
ν SC(44), δ SCC(26)	428	431	ν CC(12), δ HCS(10), δ CCC(17), τ HCCC(17)	1280	1282
τ HCCS(82), τ SCCC(10)	432	434	τ HCNN(93)	1251	1298
ν CC(12), δ HCS(10), δ CCC(17), τ HCCC(17)	446	449	δ HCH(12), δ NNC(15), τ HCCN(36)	1313	1326
τ HCNN(93)	453	461	ν CC(10), τ HCCC(35)	1331	1368
δ HCH(12), δ NNC(15), τ HCCN(36)	458	469	δ HCH(11), τ HCCC(51), τ CCCC(10)	1352	1395
ν CC(10), τ HCCC(35)	479	484	τ HCCN(22)	1377	1400
δ HCH(11), τ HCCC(51), τ CCCC(10)	497	493	δ HCH(24), τ HCCC(28)	1388	1414
δ HCH(21), τ HCCN(59)	512	522	δ HCH(58), τ HCCC(14)	1415	1437
ν NN(12), ν NC(15), δ NNC(19)	528	543	δ HCH(75), τ HCCC(22)	1420	1441
ν NN(27), δ HNN(10), τ HCCN(28)	554	567	δ HCH(79), τ HCCC(22)	1423	1451
ν CC(16), δ HCS(34), δ HCC(31)	591	591	δ HCC(10), δ HCC(10)	1436	1453
ν CC(11), ν NC(20), ν NN(16), δ CNN(15)	601	601	δ HCH(38)	1448	1460
δ HCS(13), δ HCC(14), δ CCC(13)	608	617	ν CC(65), δ HCC(10)	1467	1488
ν NC(39)	635	643	ν NC(11), δ HCN(17)	1469	1490
ν NN(22), δ CNN(24)	638	663	ν NC(52)	1473	1495
δ HNN(65)	672	686	ν CC(53), δ HCC(10)	1555	1590
τ HCCC(62)	674	691	ν OC(10)	1564	1590
ν CC(12), δ HCS(14), δ HCC(10), δ HCH(23)	678	701	ν NC(10), ν OC(72)	1566	1610
ν CC(14), δ HCH(56)	695	717	ν CH(83)	1570	1617
δ HCH(56)	699	734	ν CH(92)	1591	1623
ν CC(16), ν NC(12), δ HCH(12)	707	742	ν CH(100)	1593	1632
δ HCH(77), τ HCCN(22)	711	745	ν CH(100)	1595	1679
ν CC(25), δ HCH(19)	726	760	ν CH(82)	1612	1716
ν SC(44), δ SCC(26)	745	774	ν CH(92)	1754	1774
τ HCCS(82), τ SCCC(10)	751	776	ν CH(54)	1760	1803
ν CC(12), δ HCS(10), δ CCC(17), τ HCCC(17)	771	792	ν CH(50)	2941	2886
τ HCNN(93)	775	802	ν CH(83)	3004	2951
δ HCH(12), δ NNC(15), τ HCCN(36)	792	806	ν CH(92)	3016	2956
ν CC(10), τ HCCC(35)	793	835	ν CH(100)	3056	3006

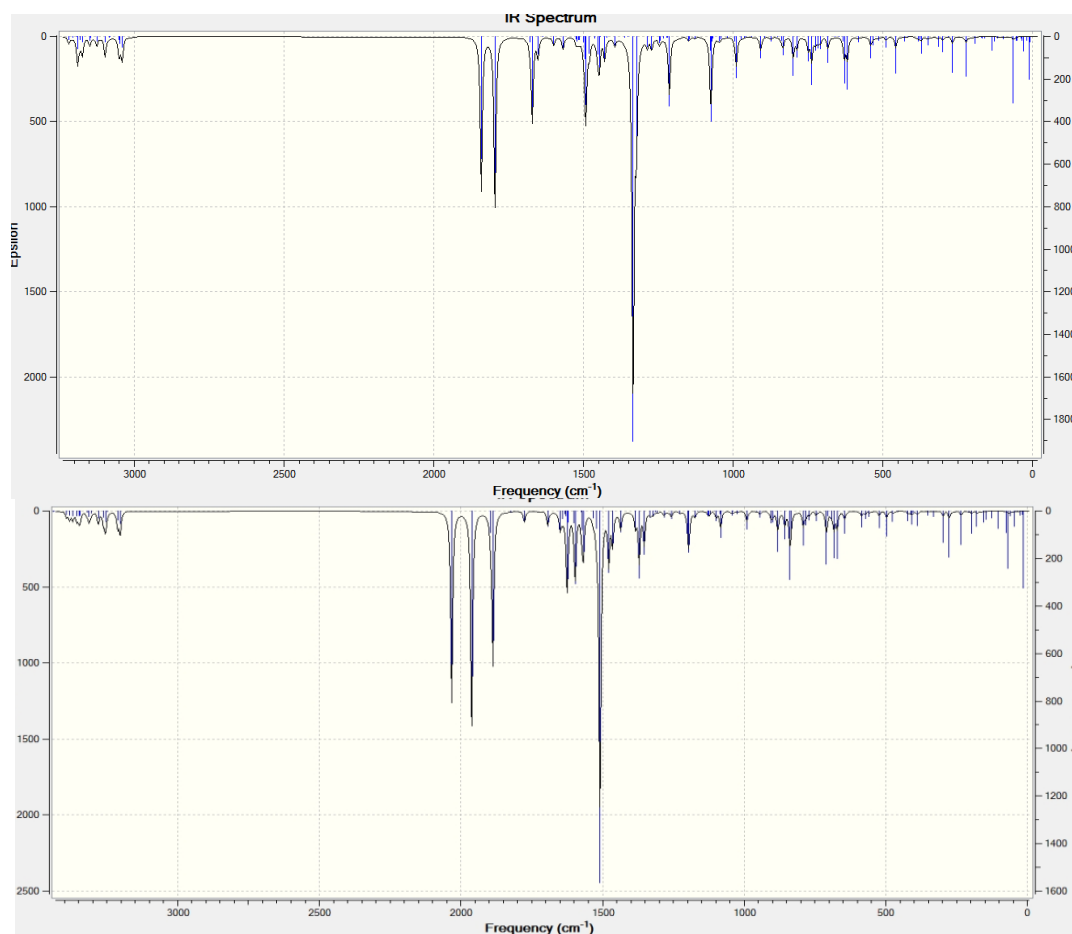


Figure 4. Theoretical IR spectrums simulated with DFT/631G(d)(a) ,HF/ 631G(d)(b).

Table 4. Bond lengths (\AA) theoretical data

Bond Lengths	B3LYP	HF	Bond Lengths	B3LYP	HF
C(1)-C(8)	1,500	1,496	C(12)-C(15)	1,511	1,511
C(1)-N(37)	1,294	1,265	C(15)-H(28)	1,098	1,083
C(1)-N(39)	1,392	1,380	C(15)-H(29)	1,095	1,086
N(37)-N(38)	1,393	1,382	C(15)-H(30)	1,094	1,085
N(38)-C(2)	1,398	1,373	C(17)-O(42)	1,207	1,183
N(38)-C(17)	1,428	1,408	C(17)-C(18)	1,510	1,506
C(2)-N(39)	1,402	1,375	C(18)-H(34)	1,093	1,081
C(2)-O(41)	1,223	1,199	C(18)-H(35)	1,093	1,081
N(39)-N(40)	1,374	1,368	C(18)-H(36)	1,090	1,079
N(40)-C(3)	1,293	1,261	C(3)-H(19)	1,086	1,071
C(8)-H(22)	1,096	1,082	C(3)-C(4)	1,442	1,457
C(8)-H(23)	1,097	1,081	C(4)-C(5)	1,387	1,358
C(8)-C(9)	1,513	1,520	C(5)-C(6)	1,429	1,438
C(9)-C(10)	1,399	1,383	C(5)-C(16)	1,505	1,506
C(10)-H(24)	1,087	1,075	C(6)-H(20)	1,085	1,085
C(10)-C(11)	1,392	1,388	C(6)-C(7)	1,367	1,343
C(10)-H(25)	1,087	1,076	C(7)-H(21)	1,082	1,071
C(11)-C(12)	1,401	1,385	C(7)-S(43)	1,729	1,719
C(12)-C(13)	1,399	1,393	C(4)-S(43)	1,755	1,741
C(13)-H(26)	1,087	1,076	C(16)-H(31)	1,092	1,080
C(13)-C(14)	1,394	1,380	C(16)-H(32)	1,097	1,085
C(14)-H(27)	1,087	1,076	C(16)-H(33)	1,096	1,085

Table 5. Bond angles ($^{\circ}$) theoretical data

bond angles	B3LYP	HF	bond angles	B3LYP	HF
N(37)-C(1)-N(39)	111,89	111,65	C(12)-C(15)-H(29)	111,43	111,10
N(37)-N(38)-C(2)	112,37	111,69	C(12)-C(15)-H(30)	111,42	111,15
N(37)-N(38)-C(17)	119,03	119,29	H(28)-C(15)-H(29)	107,12	107,81
C(17)-N(38)-C(2)	128,58	129,01	H(28)-C(15)-H(30)	107,35	107,85
N(38)-C(2)-O(41)	129,81	129,35	H(29)-C(15)-H(30)	107,93	107,41
O(41)-C(2)-N(39)	127,99	127,85	N(38)-C(2)-N(39)	102,18	102,79
N(37)-C(1)-C(8)	126,34	124,46	N(38)-N(37)-C(1)	105,21	105,66
N(39)-C(1)-C(8)	121,76	123,85	C(2)-N(39)-N(40)	130,57	130,07
C(1)-C(8)-H(22)	107,90	106,26	C(1)-N(39)-N(40)	121,08	121,29
C(1)-C(8)-H(23)	107,78	109,11	N(39)-N(40)-C(3)	118,94	119,69
C(1)-C(8)-C(9)	113,96	112,53	N(40)-C(3)-H(19)	122,03	122,53
H(22)-C(8)-H(23)	105,15	108,17	H(19)-C(3)-C(4)	118,17	117,65
H(22)-C(8)-C(9)	110,75	110,31	C(3)-C(4)-C(5)	127,41	126,86
H(23)-C(8)-C(9)	110,84	110,27	C(3)-C(4)-S(43)	120,97	121,21
C(9)-C(10)-H(24)	119,62	119,88	C(4)-C(5)-C(6)	111,71	111,64
C(9)-C(10)-C(11)	120,79	120,70	C(4)-C(5)-C(16)	125,96	127,17
H(24)-C(10)-C(11)	119,58	119,41	H(31)-C(16)-H(32)	107,62	107,86
C(10)-C(11)-H(25)	119,43	119,14	H(31)-C(16)-H(33)	107,63	107,75
H(25)-C(11)-C(12)	119,46	119,74	H(32)-C(16)-H(33)	107,05	107,46
C(10)-C(11)-C(12)	121,10	121,11	C(16)-C(5)-C(6)	122,32	121,17
C(11)-C(12)-C(13)	117,88	117,94	C(5)-C(6)-C(7)	113,401	113,09
C(12)-C(13)-H(26)	119,47	119,57	H(20)-C(6)-C(7)	123,46	123,82
C(12)-C(13)-C(14)	121,08	121,09	C(6)-C(7)-S(43)	112,31	112,40
H(26)-C(13)-C(14)	119,43	119,32	C(6)-C(7)-H(21)	127,73	127,31
C(13)-C(14)-H(27)	119,54	119,68	H(21)-C(7)-S(43)	119,95	120,28
H(27)-C(14)-C(9)	119,63	119,62	C(4)-S(43)-C(7)	90,97	90,93
C(12)-C(15)-H(28)	111,35	111,31			

Table 6. The calculated mulliken charges data of the molecule

	DFT	HF		DFT	HF
C1	0,566	0,657	H23	0,187	0,225
C2	0,860	1,116	H24	0,125	0,219
C3	0,085	0,130	H25	0,123	0,198
C4	-0,230	-0,327	H26	0,122	0,200
C5	0,172	0,077	H27	0,124	0,225
C6	0,130	-0,183	H28	0,163	0,174
C7	-0,337	-0,407	H29	0,161	0,179
C8	-0,441	-0,405	H30	0,157	0,178
C9	0,184	0,003	H31	0,175	0,190
C10	-0,160	-0,212	H32	0,173	0,190
C11	-0,177	-0,232	H33	0,172	0,191
C12	0,181	0,042	H34	0,191	0,211
C13	-0,179	-0,219	H35	0,191	0,213
C14	-0,169	-0,205	H36	0,180	0,210
C15	-0,531	-0,508	N37	-0,310	-0,302
C16	-0,535	-0,514	N38	-0,445	-0,684
C17	0,579	0,753	N39	-0,437	-0,650
C18	-0,521	-0,571	N40	-0,318	-0,312
H19	0,218	0,290	O41	-0,542	-0,514
H20	0,144	0,214	O42	-0,421	-0,649
H21	0,180	0,240	S43	0,283	0,337
H22	0,187	0,232			

Table 7. The calculated dipole moments data of the molecule

Dipol Moment	B3LYP	HF
μ_x	0.4376	0.4753
μ_y	-2.9185	-3.3217
μ_z	2.1723	0.1502
μ_{Toplam}	3.6644	3.3589

Table 8. The calculated total energy data B3LYP/HF of the molecule

Enerji (a.u.)	B3LYP	HF
	-1464.3804	-1457.1220

2.5. Electronic properties of molecule

The HOMO-LUMO energy gap in compound is 4.21; 10.68 e.v. All these parameters such as global chemical potential (μ), global hardness (η), the electronegativity (χ), ionization potential (I), chemical potential (Pi), Nucleophilic index (IP), electrophilic index (ω) have been determined for the target compound using 6-31G (d) basis set (Table 9).

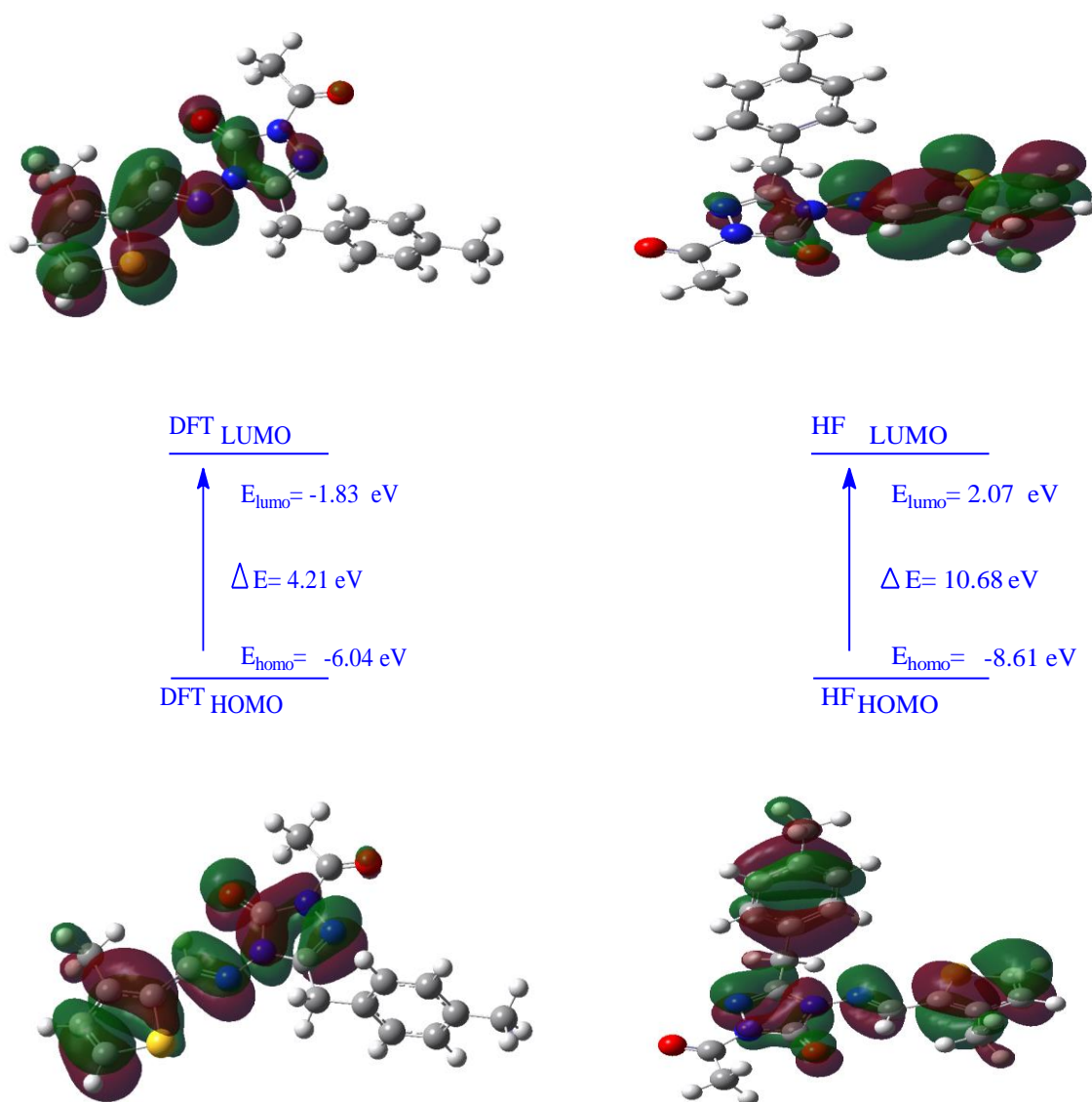
**Figure 5.** HOMO-LUMO energy gap.

Table 9. The electronic structure parameters of the molecule (HF 631G(d))

		Hatree	eV	kcal/mol	kJ/mol
	LUMO	0,07637	2,07808	47,9224	200,509
	HOMO	-0,31677	-8,61953	-198,774	-831,68
A	Electron affinity	-0,07637	-2,07808	-47,9224	-200,509
I	Ionization potential	0,31677	8,61953	198,774	831,68
ΔE	Energy gap	0,39314	10,6976	246,697	1032,19
χ	Electronegativity	0,1202	3,27073	75,4259	315,585
Pi	Chemical potential	-0,1202	-3,27073	-75,4259	-315,585
ω	Electrophilic index	0,001420026	0,03864	0,89107	3,72828
IP	Nucleophilic index	-0,02362771	-0,64293	-14,8265	-62,0346
S	Molecular softness	5,0872	138,428	3192,26	13356,6
η	Molecular hardness	0,19657	5,34881	123,348	516,095

2.6. Investigation of thermodynamics properties of compound

Thermodynamic parameters are shown in Table 10. Thermodynamic parameters of molecule were calculated 233.044 K and 1 atm of pressure. Also, the standard thermodynamic functions of enthalpy H^0 , heat capacity CV^0 and entropy S^0 were obtained at the B3LYP/DFT/HF631G(d) level.

Table 10. The calculated thermodynamic parameters of the molecule

	DFT	HF
Rotational temperatures (Kelvin)		
A	0.01331	0.00948
B	0.00501	0.00772
C	0.00375	0.00477
Rotational constants (GHZ)		
A	0.27733	0.19759
B	0.10443	0.16088
C	0.07804	0.09934
Thermal Energies E (kcal/mol)		
Translational	0.889	0.889
Rotational	0.889	0.889
Vibrational	223.632	239.054
Total	225.410	240.831
Thermal Capacity CV (cal/mol-K)		
Translational	2.981	2.981
Rotational	2.981	2.981
Vibrational	82.425	76.126
Total	88.386	82.088
Entropy S (cal/mol-K)		
Translational	43.487	43.487
Rotational	36.207	35.875
Vibrational	99.970	90.736
Total	179.664	170.098
Zero-point correction (Hartree/Particle)	0.334969	0.361125
Thermal correction to Energy	0.359213	0.383789
Thermal correction to Enthalpy	0.360157	0.384733
Thermal correction to Gibbs Free Energy	0.274793	0.303914
Sum of electronic and zero-point Energies	-1464.045482	-1456.760883
Sum of electronic and thermal Energies	-1464.021237	-1456.738219
Sum of electronic and thermal Enthalpies	-1464.020293	-1456.737275
Sum of electronic and thermal Free Energies	-1464.105658	-1456.818094
Zero-point vibrational energy (Kcal/mol)	210.19598	226.60957

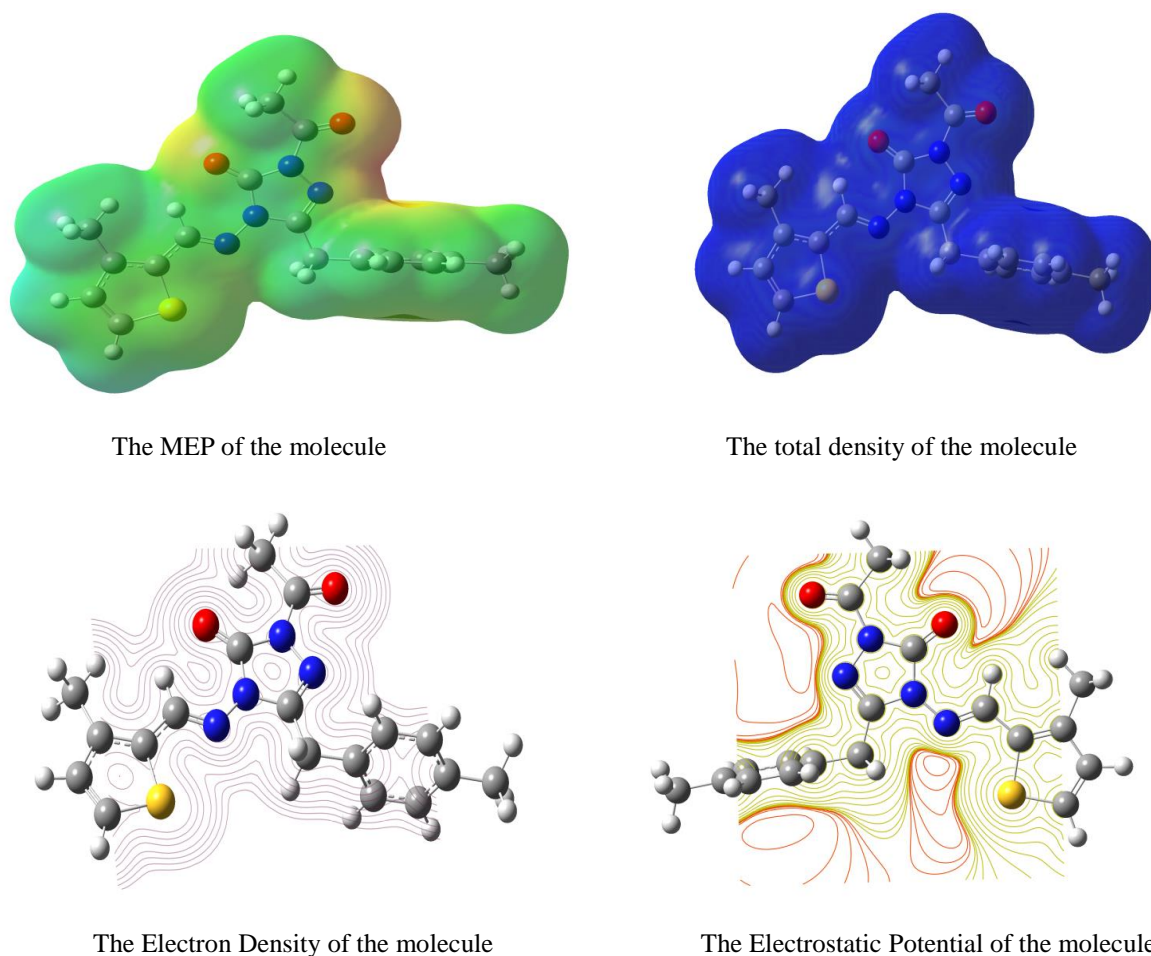


Figure 6. The calculated molecular surfaces of the molecule.

3. CONCLUSIONS

Spectroscopic parameters such as ^{13}C and ^1H -NMR, IR and geometrical parameters were calculated by HF and DFT methods with the 6-31G(d) basis sets of the program package Gaussian G09W. These calculations were compared with the experimental findings. The chemical shifts in the calculations $^{13}\text{C}/^1\text{H}$ -NMR and IR values were found that this data approximately fitted to the experimental data. Experimental and theoretical ^{13}C and ^1H chemical shifts ratios between according to R^2 and a, b values linear a correlation were observed. In addition, Theoretical infrared vibration values were determined with Veda4f program and important results. Furthermore, total energy of the molecule, global hardness (η), bond lengths, softness (σ), LUMO-HOMO, $E_{\text{LUMO}}-E_{\text{HOMO}}$ energy gap (ΔE_g), mulliken charges, thermodynamics properties, dipole moments, ionization potential (I), electron affinity (A), electronegativity (χ) were calculated with B3LYP/ HF/DFT631G (d) basis sets.

Conflict of interest

Authors declare that there is no a conflict of interest with any person, institute, company, etc.

REFERENCES

1. Das, K.; Datta, A.; Nandi, S.; Mane, S.B.; Mondal, S.; Massera, C.; Sinha, C.; Hung, C.H.; Askun, T.; Çelikboyun, P.; Cantürk, Z.; Garribba, E.; Akitsu, T.; *Inorg.Chem. Front.* **2015**, 749-762.
2. Zahid, H.C.; Sajjad, H.S.; Moulay, H.Y.; Taibi, B.H. *Eur. J. Med. Chem.* **2010**, 45, 2739-274.
3. Balram, S.; Mahendra, S.R.; Rambabu, S.; Anil B.; Sanjay, S. *Eur. J. Med. Chem.* **2010**, 45, pp. 2938-2942.
4. Wang, B. L.; Shi, Y. X.; Ma, Y.; Liu, X. H.; Li, Y. H.; Song, H.B.; Li, B.J.; Li, Z. M. *J. Agric. Food Chem.* **2010**, 58, 5515-5522.

DOI: <http://dx.doi.org/10.32571/ijct.474279>

E-ISSN:2602-277X

5. Hu, G. Q.; Wang, G. Q.; Duan, N. N.; Wen, X. Y.; Cao, T. Y.; Xie, S. Q.; Huang, W.L. *Acta Pharm. Sin. B.*, **2012**, 3, 312-317.
6. Young, D. W. *Heterocyclic Chemistry*, Frst ed., Longman group Ltd., London, 1975.
7. Kumar, K. S.; Ganguly, S.; Veerasamy, R.; De Clercq, E. *Eur. J. Med. Chem.* **2010**, 45 (11), 5474-5479.
8. Patel, R. V.; Park, S. W. *Eur. J. Med. Chem.* **2014**, 71, 24-30.
9. Shanty, A. A.; Philip, J. E.; Sneha, E. J.; Kurup, M. R. P.; Balachandran, S.; Mohanan, P. V. *Bioorg. Chem.* **2017**, 70, 67-73.
10. Pontiki, E.; Hadjipavlou-Litina, D.; Chaviara, A. *J. Enzym. Inhib. Med. Chem.* **2008**, 23 (6), 1011-1017.
11. Mari, S. K.; Bantwal, S. H.; Nalilu, S. K. *Eur. J. Med. Chem.*, **2008**, 43, 309-314.
12. Boraie, A. T. A.; Gomaa, M. S.; Ashry, S. H.; Duerkop, A. *Eur. J. Med. Chem.*, **2017**, 125, 360-371.
13. Bensaber, S. M.; Allafe, H.; Ermeli, N. B.; Mohamed, S. B.; Zetrini, A. A.; Alsabri, S. G.; Erhuma, M.; Hermann, A.; Jaeda, M. I.; Gbaj, A. M. *Med. Chem. Res.* **2014**, 23 (12), 5120-5134.
14. Sinha, A., Banerjee, K., Banerjee, A., Das, S., Choudhuri, S. K. *J. Organomet. Chem.* **2014**, 772, 34-41.
15. Papadopoulou, M. V.; Bloomer, W. D.; Rosenzweig, H.S.; Chatelain, E.; Kaiser, M.; Wilkinson, S. R.; McKenzie, C.; Ioset, J. R. *J. Med. Chem.* **2012**, 55, 5554-5565.
16. Li, Y. H.; Zhang, B.; Yang, H. K.; Li, Q.; Diao, P. C.; You, W. W.; Zhao, P. L. *Eur. J. Med. Chem.* **2017**, 125, 1098-1106.
17. Xia, Z. P.; Wang, X. D.; Wang, P. F.; Zhou, Y.; Zhang, J. W.; Zhang, L.; Zhou, J.; Zhou, S. S.; Ouyang, H.; Lin, X.Y.; Mustapa, M.; Reyinbaike, A.; Zhu, H. L. *Eur. J. Med. Chem.*, **2014**, 80, 92-100.
18. Yüksek, H.; Gürsoy, Ö.; Çakmak, İ.; Alkan, M. *Magn. Reson. Chem.* **2005**, 43, 585-587.
19. Yüksek, H.; Çakmak, İ.; Sadi, S.; Alkan, M. Baykara, H. *Int. J. Mol. Sci.* **2005**, 6, 219-229.
20. Yüksek, H.; Alkan, M.; Bahçeci, Ş.; Çakmak, İ.; Ocak, Z.; Baykara, H.; Aktaş, Ö.; Ağyel, E. *J. Mol. Struc.* **2008**, 873, 142-148.
21. Yüksek, H.; Alkan, M.; Çakmak, İ.; Ocak, Z.; Bahçeci, Ş.; Calapoğlu, M.; Elmastaş, M.; Kolomuç, A.; Aksu, H. *Int. J. Mol. Sci.* **2008**, 9, 12-32.
22. Gökçe, H.; Bahçeli, S.; Akyıldırım, O.; Yüksek, H.; Gürsoy-Kol, Ö. *Lett. Org. Chem.* **2013**, 10 (6), 395-441.
23. Gökçe, H.; Akyıldırım, O.; Bahçeli, S.; Yüksek, H.; Gürsoy-Kol, Ö. *J. Mol. Struc.* **2013**, 1056-1057, 273-284.
24. Frisch, M. J.; Trucks, G. W.; Schlegel, H. B.; Scuseria, G. E.; Robb, M. A.; Mennucci, B.; Petersson, G. A.; Nakatsuji, H.; Caricato, M.; Li, X. et al. Gaussian 09, Revision C.01, Gaussian, Inc., Wallingford, CT. **2009**. 200.
25. Wolinski, K.; Hilton, J. F. Pulay, P. *J. Am. Chem. Soc.* **1990**, 112, 512.
26. Jamróz, M. H. *Vibrational Energy Distribution Analysis: VEDA 4 program*, Warsaw, 2004.
27. Gürsoy-Kol, Ö.; Yüksek, H.; İslamoğlu, F. *J. Chem. Soc. Pakistan* **2013**, 35(4), 1179-1190.
28. Merrick, J. P.; Moran, D.; Radom, L. *J. Phys. Chem.* **2007**, 111 (45), 11683-11700.
29. Ocak, N.; Çoruh, U.; Kahveci, B.; Şaşmaz, S.; Vazquez-Lopez, E. M.; Erdönmez, A. *Acta Cryst. Sec. E.* **2003**, 59(6), 750-752.
30. Ustabas, R.; Çoruh, U.; Sancak, K.; Ünver, Y.; Vazquez-Lopez, E.M. *Acta Cryst. Sec. E.* **2007**, 63, 2982-3051.
31. Fessenden, R. J.; Fessenden, J. S. *Organic Chemistry*, Third Edition, Brooks, Cole Publishing Company, California, 1986.
32. İkizler, A. A. *Organik Kimyaya Giriş*, Dördüncü Baskı, KTÜ Basımevi, Trabzon, Türkiye, 1996, 398 (in Turkish).
33. Mulliken, R S. *J. Chem Phys.* **1955**, 23, 1833-1840.

ORCID

ID <https://orcid.org/0000-0002-4507-9029> (G. Kotan)ID <https://orcid.org/0000-0002-6620-5493> (B. Savaş)ID <https://orcid.org/0000-0003-1289-1800> (H. Yüksek)



Total phenolic and flavonoid contents and antioxidant capacity of home-made Isabella grape (*Vitis labrusca* L.) vinegar

Sinem AYDIN^{1,*}, Cavidan DEMİR GÖKİŞİK²

on the last page

¹Department of Biology, Faculty of Science and Arts, Giresun University, 28100, Giresun, Turkey

²Department of Food Engineering, Faculty of Engineering, Giresun University, 28100, Giresun, Turkey

Receive, 18 September 2018; Revised: 21 January 2019; Accepted: 22 January 2019

*Corresponding author e-mail: sinem.aydin@giresun.edu.tr

Citation: Aydın, S.; Cavidan, D. G. *Int. J. Chem. Technol.* 2019, 3 (1), 11-16.

ABSTRACT

Vitis vinifera is commonly consumed and utilized to produce juice, which has health benefits. The purpose of the current study is to determine antioxidant activity of the vinegar obtained from *V. vinifera*. While total phenolic content was found as 160.23 ± 0.007 µg GAE/ml, total flavonoid content was determined as 298 ± 0.069 µg CE/ml. Moreover, total antioxidant capacity was detected as 113.12 ± 0.011 µg AAE/ml. CUPRAC activity and DPPH radical scavenging activity of the vinegar was higher than standards (BHT for CUPRAC activity, BHT and Rutin for DPPH activity). The grape vinegar exhibited lower ABTS radical scavenging activity than standards (BHT and Rutin). Both ABTS and DPPH radical scavenging activity of the grape vinegar and standards (BHT and Rutin) increased with the increasing concentration. ABTS activity of the vinegar ranged between 27.47% and 63.72%. This study reveals that grape vinegar possess significant antioxidant properties and may be an alternative to synthetic antioxidant agents.

Keywords: Phenolic content, antioxidant activity, *Vitis labrusca*, vinegar.

Ev yapımı Isabella üzümü (*Vitis labrusca* L.) sirkesinin toplam fenolik ve flavonoid içerikleri ve antioksidan kapasitesi

ÖZ

Vitis vinifera sağlığa yararlı olan meyve suyu üretiminde kullanılmakta ve sıklıkla tüketilmektedir. Mevcut araştırmanın amacı *V. vinifera*'dan elde edilen sirkenin antioksidan aktivitesini belirlemektir. Total fenolik içeriği 160.23 ± 0.007 µg GAE/ml olarak bulunurken; toplam flavonoid içeriği 298 ± 0.069 µg CE/ml olarak saptanmıştır. Ayrıca, total antioksidan kapasitesi 113.12 ± 0.011 µg AAE/ml olarak belirlendi. Sirkenin CUPRAC aktivitesi ve DPPH radikal süpürme aktivitesi standartlardan (CUPRAC aktivitesi için BHT, DPPH aktivitesi için BHT ve Rutin) daha yüksektir. Üzüm sirkesi standartlardan daha düşük bir ABTS radikal süpürme aktivitesi sergiledi. Üzüm sirkesinin ve standartların hem ABTS hemde DPPH süpürme aktiviteleri artan konsantrasyonlarla artmıştır. Sirkenin ABTS aktivitesi 27.47% ve 63.72% arasında değişmiştir. Bu çalışma üzüm sirkesinin önemli antioksidan özelliklere sahip olduğunu ve sentetik antioksidan ajanlara alternatif olabileceğini ortaya koymaktadır.

Anahtar Kelimeler: Fenolik içerik, Antioksidan aktivite, *Vitis labrusca*, sirke.

1. INTRODUCTION

Vinegar forms after fermentation process. Vinegar mainly includes carbohydrates-rich foods.¹ Ethyl alcohol provides partial oxidation during the conversion

of wine or fruit juice into vinegar, and then acetaldehyde is generated. Finally, the acetaldehyde is converted into acetic acid.²

For more than 2000 years, the vinegar has been utilized for flavoring and preserving foods, curing

wounds, struggling infections, cleaning surfaces, and controlling diabetes.³ Daily intake of the vinegar was recorded to protect against some illnesses, such as hypertension, obesity and hyperlipidemia. Besides this the vinegar has also some healthy features such as promoting recovery, adjusts blood glucose, blood pressure, helps digestion, induces the appetite, and helps calcium absorption.⁴

Acetic acid and other components which found in vinegar might be attributed to its therapeutic impact¹. Natural vinegar contains various medicinal components such as carbohydrate, organic acid (e.g. acetic, formic, gallic acid catechin, lactic and malic), alcohols and amino acid and peptides, vitamins and minerals salts.⁵ Friedman and co-workers have revealed that some properties of the vinegar such as acidity, alcohol content, and content of polyphenolic compounds like tannins and resveratrol might have antimicrobial effects against foodborne microorganisms.⁴

The ingestion of the vinegar is stated to be linked with satiety and to decrease intake of subsequent meals, which this situation can contribute to weight loss.⁶ Recently, vinegar has an importance in gastronomy and its quality is protected by title of origin in different vinegar-producing areas. Vinegar is generally utilized as an ingredient in the food, and it is a suitable solvent for the essential oils of herbs and spices in the salads or meals.⁴

An antioxidant can be explained as any substance that inhibits oxidative damage to a target molecule. An antioxidant have the ability to scavenge free radicals. Antioxidant compounds such as phenolic acids, polyphenols and flavonoids scavenge free radicals, so they inhibit the oxidative mechanisms that cause to degenerative illnesses.⁷ Recent studies has demonstrated that bioactive compounds found in the vinegar may reduce degenerative diseases through antioxidant effects.⁸

In this study, antioxidant activity of home-made vinegar which prepared from fragrant black grapes (isabella) grown in Black Sea, Giresun region was investigated.

2. MATERIALS AND METHODS

2.1. Chemicals

Butylated hydroxytoluen (BHT), 2,2'-azinobis (3-ethylbenzthiazoline-6-sulfonic acid) (ABTS) were purchased from Fluka Chemical Co. (Buchs, Switzerland). 2,2-diphenyl-1-picryl-hydrazyl (DPPH), gallic acid, catechin, neocuproine, CuCl_2 , ammonium acetate, sulfuric acid, sodium phosphate, ammonium

molybdate, ascorbic acid and rutin were obtained from Sigma Chemical Co. (St. Louis, MO, USA).

2.2. Preparation of the vinegar

Fragrant black grapes (isabella) used in the production of the vinegar, grown in Giresun region, were collected from Giresun-Piraziz-Gökçeali Village in November 2017. Grapes which used for production of vinegar were also collected and brought to the laboratory. The washed grape dices were taken into a large clean container and 3 times as much water was added. Clean and untreated village water was used. It was kept in the dark for 30 days and shaken for oxygenation. After 30 days, it was drained, and the mouth was closed with cloth for 60 days. Then it was kept in the dark for maturation. After 90 days, the formation of the vinegar was completed and analyzes were made.

2.3. Total phenolic content

Total phenolic content of the vinegar was examined by Folin-Ciocalteu assay. Total phenolic contents of grape vinegar were determined in accordance with the method of Slinkard and Singleton (1977) utilizing gallic acid standard. Shortly, 0.1 ml vinegar was diluted with 4.5 ml distilled water. Then, 0.1 ml Folin-Ciocalteu reagent (previously diluted 3- fold with distilled water) was put into the mixture. After 3 minutes, 0.3 ml Na_2CO_3 (2%) was added. The absorbance was measured at 760 nm after incubating the mixture for 90 min. Total phenolic content of the extracts was expressed as μg gallic acid equivalents (GAE)/ml by using the calibration curve.⁹ The tests were performed in triplicate.

2.4. Total flavonoid content

0.25 ml vinegar, 1.25 ml distilled water and 75 μl NaNO_2 (5%) were mixed and vortexed. After 6 min, 150 μl of $\text{AlCl}_3 \cdot 6\text{H}_2\text{O}$ (10%) was added and the mixture was kept at room temperature for 5 min. Then, 0.5 ml NaOH (1M) and 725 μl distilled water added the mixture. Absorbance was measured at 510 nm. Catechin was used as standard and the results were expressed as μg catechin equivalent (CE)/ml.¹⁰ The tests were performed in triplicate.

2.5. Antioxidant activity

2.5.1. ABTS radical scavenging activity

ABTS⁺ solution was prepared by mixing 7.4 mM ABTS and 2.6 mM potassium persulfate, and the mixture was kept at room temperature for 12 h in the dark to complete reaction. Then, ABTS⁺ solution diluted with

methanol to obtain an absorbance of 0.700 ± 0.02 units at 734 nm.²³ Vinegar (150 μ l) was allowed to react with 2850 μ l of the ABTS⁺ solution for 2 h in a dark, and the absorbance was measured at 734 nm.¹¹ The tests were performed in triplicate. The ABTS radical scavenging activity was calculated using the following equation.

ABTS radical scavenging activity (% inhibition):

$$[(A_0 - A_1) / A_0] \times 100 \quad (1)$$

A_0 = Absorbance of control, A_1 = Absorbance of sample.

2.5.2. DPPH radical scavenging activity

Appropriate dilution series (50-200 μ g ml⁻¹) were added 1.5 ml of a 6×10^{-5} M methanolic solution of DPPH. After vortexing the tubes, the tubes were incubated in the dark. After 30 minutes, the absorbance was read at 517 nm. Synthetic antioxidant reagents BHT and rutin were used as positive control.¹² The tests were performed in triplicate. The DPPH radical scavenging activity was calculated using the following equation:

DPPH radical scavenging activity (% inhibition):

$$[(A_0 - A_1) / A_0] \times 100 \quad (2)$$

A_0 = Absorbance of control, A_1 = Absorbance of sample.

2.5.3. Total antioxidant capacity

Phosphomolybdenum method was used to determine total antioxidant capacity of the vinegar.¹³ 0.3 ml vinegar

and 3000 μ l reagent (contains 0.6 M sulfuric acid, 28 mM sodium phosphate and 28 M ammonium molybdate) was mixed and incubated at 95 °C for 90 min. Then, Absorbance was read at 695 nm. Ascorbic acid was used as the standard. The total antioxidant capacity was expressed as μ g ascorbic acid equivalent (AAE)/ml. The tests were performed in triplicate.

2.5.4. Cupric reducing antioxidant capacity (CUPRAC)

0.5 ml vinegar (prepared in 250-1000 μ g ml⁻¹), 1.0 ml CuCl₂ solution, 1 ml neocuproine solution and 1.0 ml ammonium acetate buffer were mixed in a test tube. Tubes were vortexed and stored in a dark place for 30 min. Absorbance was measured at 450 nm. BHT was utilized as standard antioxidant substance.¹⁴

3. RESULTS AND DISCUSSION

Phenols improve the status of various oxidative stress biomarkers. Phenols have many antioxidative mechanisms such as scavenge free radicals, break radical chain reactions, reducing peroxides, and stimulate the antioxidative defense enzyme activities.¹⁵

Flavonoids are secondary plant metabolites which are responsible for producing yellow and other pigments in the plants. Moreover, flavonoids exhibit significant activities in humans.¹⁶

Total phenolic and flavonoid contents, total antioxidant capacity are given in Table 1. Total phenolic and flavonoid contents, total antioxidant capacity of the grape vinegar were determined as 160.23 ± 0.007 μ g GAE/ml, 298 ± 0.0069 μ g CE/ml and 113.12 ± 0.011 μ g AAE/ml, respectively. DPPH, ABTS scavenging activi-

Table 1. Total phenolic, total flavonoid contents and total antioxidant capacity of the grape vinegar

	Total Phenolic Content (μ g GAE/ml)	Total Flavonoid Content (μ g CE/ml)	Total Antioxidant Capacity (μ g AAE/ml)
Grape Vinegar	160.23 ± 0.007	298 ± 0.0069	113.12 ± 0.011

ties and CUPRAC activity of the grape vinegar are demonstrated in Table 2. Grape vinegar exhibited strong DPPH radical scavenging activity even better than the standards such as BHT and Rutin. DPPH activity of the vinegar is illustrated in Figure 1. DPPH activity of the vinegar ranges between 83.66% to 95.81%. DPPH activity of the vinegar increases with the increasing concentrations. The activity was increased in the following order: Grape vinegar > Rutin > BHT.

Grape vinegar exhibited the weak ABTS radical scavenging activity. ABTS activity of the vinegar was summarized in Figure 2. Contrary to DPPH scavenging activity, standards have higher activity than vinegar in

ABTS assay. ABTS radical scavenging activity of the grape vinegar and standards increase with the increasing concentrations. ABTS activity of the vinegar ranges from 27.47% to 63.72%.

Moreover, vinegar demonstrated high CUPRAC activity when compared with DPPH and ABTS scavenging activities. Vinegar possess CUPRAC activity better than BHT which used as standard. There are some studies about antioxidant ability of vinegars from Isabella grapes (*Vitis labrusca*) in literatures. For example, Machado and co-workers¹⁷ found total phenolic contents of organic grape (*V. labrusca*) vinegar, Grape (*V. labrusca*) vinegar organic 5% enriched with grape

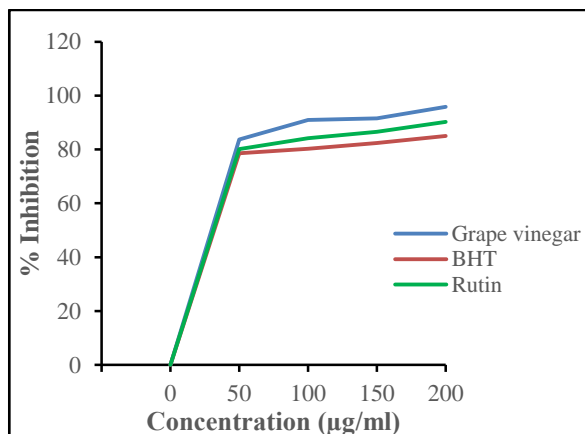


Figure 1. DPPH radical scavenging activity of the vinegar and standards.

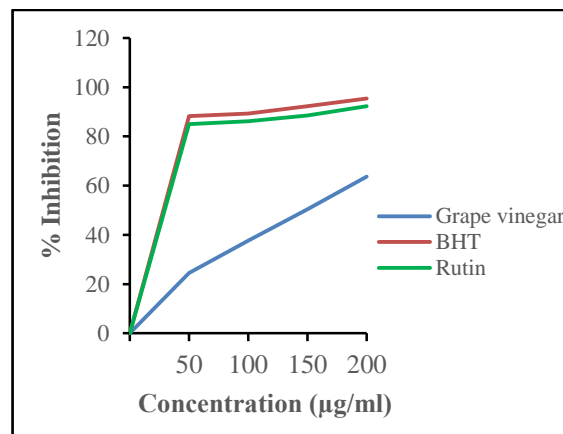


Figure 2. ABTS scavenging activity of the vinegar and standards.

Table 2. DPPH and ABTS scavenging activities of the grape vinegar (% inhibition)

	Concentration ($\mu\text{g ml}^{-1}$)	DPPH radical scavenging activity (% inhibition)	ABTS radical scavenging activity (% inhibition)	Concentration ($\mu\text{g ml}^{-1}$)	CUPRAC Activity
Grape vinegar	50	83.66±0.006	27.47±0.014	250	1.1273±0.003
	100	91.00±0.014	37.65±0.028	500	1.9936±0.078
	150	91.52±0.005	50.40±0.018	750	2.5125±0.039
	200	95.81±0.005	63.72±0.006	1000	2.5328±0.02
BHT	50	78.62±0.005	88.28±0.04	250	0.7026±0.003
	100	80.29±0.002	89.32±0.006	500	0.7151±0.026
	150	82.35±0.001	92.33±0.004	750	0.8822±0.010
	200	85.05±0.003	95.45±0.008	1000	0.9810±0.004
Rutin	50	80.17±0.003	84.94±0.048	-	-
	100	84.22±0.004	86.14±0.019	-	-
	150	86.54±0.003	88.46±0.010	-	-
	200	90.25±0.005	92.23±0.006	-	-

seeds and grape (*V. labrusca*) vinegar organic 10% enriched with grape seeds which prepared from grapes in Brazil as 23.62 ± 0.4 mg gallic acid/ml, 39.78 ± 0.29 mg gallic acid/ml and 24.80 ± 2.05 mg gallic acid/ml, respectively. Moreover, it was found that total flavonoid contents of organic grape vinegar, grape vinegar organic 5% enriched with grape seeds and grape vinegar organic 10% enriched with grape seeds as 0.110 ± 0.007 mg quercetin/ml, 0.118 ± 0.007 mg quercetin/ml and 0.124 mg quercetin/ml, respectively.¹⁷ In our study, it was determined total phenolic and flavonoid contents of grape vinegar as 160.23 ± 0.007 μ g GAE/ml and 298 ± 0.0069 μ g CE/ml. These different results might be attributed to use grapes from different geological areas. Machado and co-workers¹⁷ also stated that IC₅₀ values of DPPH activity of the grape vinegar organic grape vinegar, grape vinegar organic 5% enriched with grape seeds and grape vinegar organic 10% enriched with grape seeds as 6.70 μ g ml⁻¹, 9.01 μ g ml⁻¹ and 7.07 μ g ml⁻¹, respectively.¹⁴

Cottica and co-workers recorded that total phenolic content of grape (*V. labrusca*) vinegar as 162.91 ± 5.98 mg GAE/100 g⁻¹ and EC₅₀ value of DPPH activity of grape vinegar as 136.23 ± 0.82 μ g ml⁻¹.¹⁸

Kelebek and co-workers stated that antioxidant activity of grape vinegars changed between 5.39% and 14.43% according to DPPH assay while the values ranged from 7.72% to 17.96% with respect to ABTS assay, respectively.¹⁹ In our study, DPPH activity of the vinegar ranges between 83.66% to 95.81% and ABTS activity of the vinegar ranged from 27.47% to 63.72%. This difference could be explained by using vinegars obtained from grapes collected from different geographical locations and using different grape species when preparing vinegar.

Different vinegar types also have antioxidative properties. For example, Hafzan and co-workers investigated homemade and commercial dated vinegars. As a result of the study, it was concluded that homemade dated vinegar showed generally higher antioxidant activity than commercial dated vinegar.²⁰ Budak searched the antioxidative ability of pomegranate vinegar.²¹ Tagliazucchi and co-workers revealed the antioxidant potential of balsamic vinegar.²² Poiana and co-workers also studied the antioxidative effect of apple vinegars.²³

4. CONCLUSIONS

According to the data obtained, it can be concluded that grape vinegar has strong antioxidant activity. The findings of the current study confirm and improve the information on health-promoting and food safety-related potentials of grape vinegar. These results might associate with the chemical composition of the grape and repre-

sent a mechanism underlying the traditional use of *Vitis labrusca* vinegar.

Conflict of interest

Authors declare that there is no a conflict of interest with any person, institute, company, etc.

REFERENCES

- Samad, A.; Azlan, A.; İsmail, A. *Curr. Opin. Food Sci.* **2016**, 8, 56-61.
- Vinegar, **1996**. Encyclopedia.com <https://www.encyclopedia.com/science-and-technology/chemistry/organic-chemistry/vinegar> (accessed September 15, 2018).
- Johnston, C. S.; Gaas, C. A. *Med. Gen. Med.* **2006**, 8(2), 61-83.
- Bakir, S. Investigating the Phenolic Content and In Vitro Bioaccessibility of Some Vinegars, and Changes in Antioxidant Activity During Grape and Apple Vinegar Processing, Istanbul Technical University. <https://polen.itu.edu.tr/bitstream/11527/2191/1/14382.pdf> (Accessed December 12, 2018).
- Akanksha, S.; Sunita; M. *Asia. J. Sci. Technol.* **2017**, 8 (12), 1-3.
- Johnston, C. S. Medicinal uses of vinegars. Watson, R.R., Ed.; Academic Press, USA, 2009; pp 433-443.
- Pour, B. M.; Jothy, S. L.; Latha, L.Y.; Chen, Y.; Sasidharan, S. *Asian Pac. J. Trop. Biomed.* **2012**, 2 (12), 960-965.
- Ali, Z.; Wang, Z.; Amir, R. M.; Younas, S.; Wali, A.; Adowa, N.; Ayim, I. 2018. *Int. J. Vitam. Nutr. Res.* **2017**, 86(3-4), 1-12.
- Slinkard, K.; Singleton, V.L. *Am. J. Enol. Vitic.* **1977**, 28, 49-55.
- Zhishen, J.; Mengcheng, T.; Jianming, W. *Food Chem.* **1999**, 64, 555-559.
- Arnao, M.B.; Cano, A.; Acosta, M. *Food Chem.* **2001**, 73, 239-244.
- Brand-Williams, W.; Cuvelier, M.; Berset, C. *LWT - Food Sci. Technol.* **1995**, 28, 25-30.
- Prieto, P.; Pineda, M.; Aguilera, M. *Anal. Biochem.* **1999**, 269, 337-341.

14. Özyürek, M.; Bektaşoğlu, B.; Güçlü, K.; Apak, R. *Anal. Chim. Acta* **2009**, 636 (1), 42-50.
15. Assia, B.; Khennouf, S.; Bouaziz, A.; Baghiani, A.; Dahamna, S.; Amira, S.; Arrar, L. *Der Pharm. Chem.* **2016**, 8(12), 88-99.
16. Rebeya, A.; Belghith, S. I.; Baghdikian, B.; Leddet, V. M.; Mabrouki, F.; Olivier, E.; Cherif, J. K.; Ayadi, M. *T. J. Appl. Pharm. Sci.* **2014**, 5(01), 052-053.
17. Machado, M.M.; Montagner, G.F.F.S.; Boligon, A.; Athayde, M.L.; Rocha, M.I.U.M.; Lera, J.P.B.; Bello, C.; Cruz, I.B.M. *Quim Nova* **2011**, 34(5), 798-803.
18. Cottica, S. M.; Morais, D. R.; Rotta, E. M.; Sargi, S.C.; Silva, F. L. N.; Sawaya, A. C. H. F.; Eberlin, M. N.; Visentainer, J. V. *J. Food Sci. Eng.* **2013**, 3, 341-348.
19. Kelebek, H.; Kadiroğlu, P.; Demircan, N. B.; Selli, S. 2017. Screening of bioactive components in grape and apple vinegars: Antioxidant and antimicrobial potential https://www.researchgate.net/publication/316602437_Screening_of_Bioactive_Components_in_Grape_and_Apple_Vinegar's_Antioxidant_and_Antimicrobial_Potential (accessed August 15, 2018).
20. Hafzan, Y.; Saw, J. W.; Fadzilah, I. *Int. Food Res. J.* **2017**, 24(6), 2557-2562.
21. Budak, N. H. *Agro Food Ind. Hi-Tech.* **2015**, 26, 68-72.
22. Tagliazucchi, D.; Verzelloni, E.; Conte, A. *Eur. Food Res. Technol.* **2008**, 227, 835.
23. Poiana, M. A.; Gergen, I.; Moigradean, D.; Taru, V.; Dogaru, D. *Bulletin USAMV-CN*, **2007**, 476-481.

ORCID

 <https://orcid.org/0000-0002-0484-7191> (S. Aydin)

 <https://orcid.org/0000-0001-7273-3156> (C. Demir Gökisik)



A Corrosion Study: Use of Thionine dye having structurally metachromatic influence

Demet ÖZKİR*

ID at end page

Department of Chemistry, Faculty of Arts & Science, Niğde Ömer Halisdemir University, 51200, Niğde, Turkey

Received: 17 January 2019; Revised: 18 February 2019; Accepted: 19 February 2019

*Corresponding author e-mail: dozkir@ohu.edu.tr

Citation: Özkır, D. *Int. J. Chem. Technol.* 2019, 3 (1), 17-25.

ABSTRACT

In the present study, it was examined the inhibition performance of Thionine, which has metachromatic properties and is generally used as a vital dye for different staining of nucleus and cytoplasm, on mild steel in acidic medium as a different application area which is not existed in the literature. In order to understand how Thionine interacts with the mild steel surface, different types of adsorption isotherms were plotted and it was seen obeyed the Langmuir isotherm. The test results revealed that as the inhibitor concentration increased at each temperature, the corrosion current density (i_{corr}) values diminished and accordingly, the inhibition efficiencies ($\eta\%$) increased slightly. The results indicated that the Thionine molecules continued to be adsorbed onto the metal surface to some extent, even when elevated to high temperatures. Thermodynamic adsorption parameters revealed a strong and chemical interaction between Thionine and mild steel. It was determined that the Thionine acted as a mixed-type inhibitor on the mild steel surface. Finally, field emission scanning electron (FESEM) and atomic force microscopy (AFM) analyses were performed to determine the surface characteristics.

Keywords: Thionine, adsorption, acidic corrosion, FESEM.

Bir korozyon çalışması: Yapısal olarak metakromatik etkiye sahip olan tiyonin boyasının kullanılması

ÖZ

Bu çalışmada, genellikle nükleus ve sitoplazmanın farklı şekillerde boyanması için metakromatik özelliğe sahip ve hayati bir boya olarak kullanılan Tiyonin'in, farklı bir kullanım alanı olarak literatürde mevcut olmayan asidik ortamdaki yumuşak çelik üzerine inhibisyon performansı incelendi. Yumuşak çelik yüzeyi ile Tiyonin'in ne şekilde etkileştiğini anlamak için farklı tür adsorpsiyon izotermi çizildi ve Langmuir izotermine uyduğu görüldü. Deney sonuçları, her sıcaklıkta inhibitör derişimi arttıkça korozyon akım yoğunluğu (i_{corr}) değerlerinin düştüğünü ve buna bağlı olarak da inhibisyon etkinliği değerlerinin ($\% \eta$) de bir miktar yükseldiğini göstermiştir. Sonuçlar, Tiyonin moleküllerinin yüksek sıcaklıklara çıktığında bile, bir dereceye kadar metal yüzeyine adsorplanmaya devam ettiğini göstermiştir. Termodinamik adsorpsiyon parametreleri, Tiyonin ile yumuşak çelik arasında güçlü ve kimyasal bir etkileşimin olduğunu ortaya çıkarmıştır. Tiyoninin, yumuşak çelik yüzeyinde karma tip bir inhibitör görevi gördüğü tespit edildi. Son olarak, yüzey karakteristiklerinin belirlenmesi için alan emisyon taramalı elektron mikroskobu (FESEM) ve atomik kuvvet mikroskobu (AFM) analizleri yapıldı.

Anahtar Kelimeler: Tiyonin, adsorpsiyon, asidik korozyon, FESEM.

1. INTRODUCTION

The first thing that comes to mind when matter is mentioned is metals, polymers and ceramics. Metals can be classified as ferrous and non-ferrous. In this study, ferrous material is used as a priority. Ferrous materials are both steel and cast iron.¹ Mild steel and its alloys are

mainly made of iron and carbon, and certain properties can be achieved by adding further alloying elements.² There are more than 3500 diverse steel grades covering unique physical, chemical and environmental characteristics, according to the World Steel Association.³ Mild steel is one of the most preferred materials in terms of usage and processability in

industry. Mild steels have advantages compared to other materials due to the fact that they are easily accessible and not expensive. In addition to being preferred in most applications, mild steels are also highly sensitive to aggressive environments such as acidic media. The primary purpose of reducing sensitivity in acidic environments is to thoroughly isolate the metal from the medium.^{4,5}

Among the most commonly used metal isolation methods, there is the application of organic inhibitors. Organic inhibitors exhibit high corrosion resistance due to their non-toxicity, having a large molecular structure and their including of heteroatoms with unpaired electron pairs such as nitrogen, sulphur and oxygen.^{6,7} These unpaired electrons facilitate the adsorption of inhibitors to the metal surface. When the inhibitors are added generally an acidic solution, they prevent from the dissolution of the metal. Dyes are also used as corrosion inhibitors such as compounds of organic origin. Dye solutions are also used as corrosion inhibitors in the corrosion process and their discharges to the environment are prevented.^{8,9} In one of recent studies done, the potential of being a good corrosion inhibitor for metals in acidic solutions as an additional usage field of dyes has been investigated.¹⁰⁻¹⁴

Thionine has been often utilized as a sensitizer in photographic processes, laser components and chemotherapy. Thionine is also used to stain the nucleus and cytoplasm in different ways and is called as a vital dye. Thionine chloride is a powerful metachromatic dye greatly utilized for biological staining¹⁵ is acknowledged as an electron-shuttling for bioelectricity production.¹⁶ The term of metachromatic was expressed to portray the colour alterations passed through certain substances when the temperature is elevated by Ackroyd in 1876.¹⁷ The first application in the biological circumstances was realized in the mast cell staining by Ehrlich in 1879.¹⁸ Metachromatic dyes are divided into two types as cationic and anionic. Thionine chloride is among the most widely used cationic metachromatic dye classes. Anionic ones are used less than cationic dyes.¹⁹ Thionine related molecules chemically possess abilities to intervene electron transport. Thionine chloride (3,7-diaminophenothiazin-5-ium chloride), shown in Figure 1, is a type of phenothiazine dye that has been thoroughly explored due to their quirky physicochemical properties. A wide range of studies and applications area of Thionine have been encountered,^{15,20,21} but no study has been observed which will report the influence of inhibitor performance for mild steel in 1.0 M HCl solution. Therefore, this paper is an original study. This current study was designed to survey a dye whether will act as inhibitor that does not contain azo group in its structure and has a metachromatic effect. In other words,

Thionine's inhibitor performance was evaluated with potentiodynamic polarization measurement technique at a temperature range of 298 K–328 K in hydrochloride acid solution and a different perspective was provided to

be used as an alternative commercial inhibitor in industrial applications. The effect of temperature on the adsorption behaviour of the Thionine molecule was also clarified by some thermodynamic parameters such as adsorption free energy (ΔG_{ads}°), adsorption equilibrium constant (K_{ads}), corrosion activation energy (E_a^*). In the last step of the study, inhibitor behaviour on metal surface was investigated by FESEM and AFM techniques.

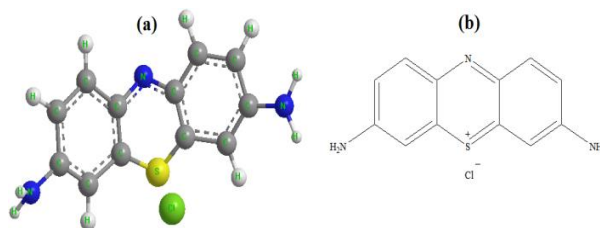


Figure 1. Three-dimensional ball & stick model (a) and chemical structure (b) of Thionine chloride inhibitor.

2. EXPERIMENTAL DETAILS

Corrosion tests were conducted on the surface of the mild steel whose chemical composition was 0.01040 Mo; 0.01900 S; 0.00222 Nb; 0.21700 Cu; 0.40900 Mn; 0.00198 Co; 0.07890 Ni; 0.08400 C; 0.01620 Sn; % 0.01100 P; 0.06030 Cr; 0.10200 Si; 0.01100 V and the rest was Fe (wt.%). The surface area of the mild steel electrode is 0.5024 cm². The surface areas of the working electrodes that will come into contact with the solution were left exposed, the entire surface was first covered with epoxy and then with polyester. Prior to all electrochemical measurements, the mild mild steel electrodes were sanded with 600 and 1000 grids of emery paper respectively, polished with alumina solution, and then cleaned in acetone and distilled water to immerse in test solutions. Experimental measurements were carried out using the classical three electrode technique by the CHI 660B model electrochemical analyser. Mild steel, whose chemical composition is given above, has been used as working electrode. Platinum (Pt), which is used as counter electrode in the study, was cut 1 x 1 cm in size from the pure platinum plate and after it was attached with Pt-wire, only the Pt plate was left out and connected with a copper wire in a glass tube. Finally, Ag/AgCl was used as the reference electrode for potentiodynamic polarization measurements. All electrochemical measurements were performed in the representative experimental set-up (see Figure 2).

The system was allowed to equilibrate for 1 hour before each measurement and then the test measurements were carried out. The electrochemical behaviour of mild steel was evaluated by Tafel extrapolation method for five different concentrations (1.0×10^{-5} M – 1.0×10^{-3} M) of 1.0 M HCl solution in the 298 K – 328 K temperature range. Corrosion current density (i_{corr}) values were determined by plotting the semi-logarithmic

current-potential curves against the potential (V) after measuring the open circuit potential (E_{corr}) of the mild steel with the reference electrode (Ag/AgCl). For this purpose, at the scanning rate of 1 mV/s, first to the cathodic direction (-350 mV) and then to the anodic direction (+350 mV) were scanned.

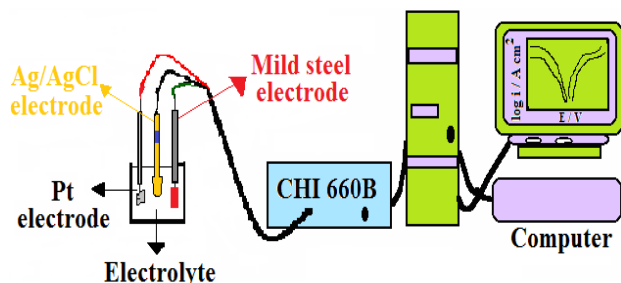


Figure 2. Representative experimental set-up obtained of potentiodynamic polarization spectra.

To obtain information about surface morphologies, surface roughness and surface elasticities of mild steel electrodes immersed into 1.0 M HCl media without and with 1.0×10^{-3} M Thionine for 120 h, the detailed surface images with FESEM (ZEISS GeminiSEM 500 model with computer controlled) and AFM (Veeco Multimode 8 Nanoscope 3D model) analyses were examined.

3. RESULTS AND DISCUSSION

3.1. Evaluation of potentiodynamic polarization tests

Potentiodynamic polarization curves in the absence and the presence of the Thionine with various concentrations (1.0×10^{-5} M – 1.0×10^{-3} M) for mild steel electrode are given in Figure 3. These curves are only for 298 K and 328 K. In addition, potentiodynamic polarization parameters obtained from these curves are given in Table 1.

The values of $\eta\%$ were calculated from the potentiodynamic polarization curves according to the following equation.²²

$$\eta (\%) = \left(\frac{i_{corr} - i'_{corr}}{i_{corr}} \right) \times 100 \quad (1)$$

Where i_{corr} and i'_{corr} are uninhibited and inhibited corrosion current density values, respectively. The E_{corr} values were measured as -0.475 V and -0.484 V in 1.0 M HCl solution and i_{corr} values were calculated as 265 and $2536 \mu\text{A cm}^{-2}$ at 298 K and 328 K, respectively (see Figure 3, Table 1). As the inhibitor was added to the anodic potentials except for a few values and ranged

from -0.460 V to -0.479 V. The values of i_{corr} in the acidic medium, the corrosion potentials shifted to more inhibited media decreased for each temperature compared to the values in the uninhibited solution.

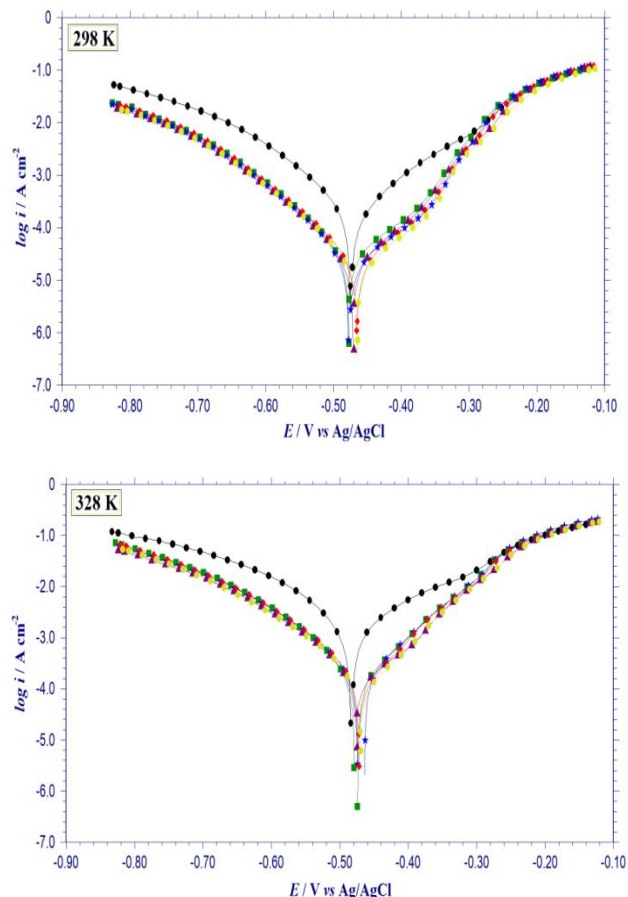


Figure 3. Potentiodynamic polarization curves obtained at 298 K and 328 K temperatures in 1.0 M HCl solutions with and without Thionine.

This reveals that the anodic dissolution of the mild steel and the cathodic reduction of the hydrogen ions are inhibited. For the same temperature in all solutions, the corrosion current density values decreased as the inhibitor concentration increased, and accordingly the inhibition efficiency values rose. The i_{corr} values boosted as temperature increased in both inhibited and uninhibited solutions. In other words, as the ionic conductivity enhances when the temperature is increased from 298 to 328 K, the current density values have boosted in both uninhibited and inhibited media. While the cathodic Tafel constant ($-\beta_c$) values ranged from 108 mV dec^{-1} to 157 mV dec^{-1} in uninhibited solutions, they ranged from 91 mV dec^{-1} to 116 mV dec^{-1} in inhibited solutions. The fact that the calculated cathodic Tafel constants do not alter significantly except for a few

Table 1. Potentiodynamic polarization parameters of mild steel in 1.0 M HCl solution containing various concentrations of Thionine at four different temperatures

Thionine Concentration (M)	Temperature (K)	E_{corr} (V/ Ag/AgCl)	$-\beta_c$ (mV dec ⁻¹)	i_{corr} ($\mu\text{A cm}^{-2}$)	η (%)
Blank	298	-0.475	108	265	-
	308	-0.487	109	440	-
	318	-0.488	128	1296	-
	328	-0.484	157	2536	-
1.0×10^{-5}	298	-0.477	91	34	87.2
	308	-0.470	100	70	84.1
	318	-0.478	107	175	86.5
	328	-0.479	110	296	88.3
5.0×10^{-5}	298	-0.478	93	32	87.9
	308	-0.463	102	61	86.1
	318	-0.467	106	150	88.4
	328	-0.474	114	286	88.7
1.0×10^{-4}	298	-0.466	94	28	89.4
	308	-0.463	98	51	88.4
	318	-0.465	110	130	90.0
	328	-0.472	110	260	89.7
5.0×10^{-4}	298	-0.470	93	24	90.9
	308	-0.474	99	49	88.9
	318	-0.460	106	109	91.6
	328	-0.475	114	241	90.5
1.0×10^{-3}	298	-0.464	92	21	92.1
	308	-0.465	96	47	89.3
	318	-0.466	106	106	91.8
	328	-0.469	116	216	91.5

values in media with and without the Thionine indicates that the hydrogen formation mechanism is neither affected by the addition of inhibitor nor by the temperature.

As seen from Figure 3, the increase in the concentration of the Thionine in the acidic medium reduced both the anodic and cathodic current density and did not change the corrosion potential much. Therefore, it can be said that the Thionine molecule acts as a mixed-type inhibitor in the 1.0 M HCl medium.^{23,24} The addition of the Thionine to the medium decreased the current value to approximately -0.25 V in the anodic part. After this potential, it was no matter how much the potential was increased in all the concentrations of the Thionine, and therefore it did not change that of the solution obtained without the inhibitor. This can be explained by desorption of the Thionine molecules adsorbed to the electrode surface.²⁵

Furthermore, the cathodic polarization curves are parallel (Figure 3), indicating that no change has occurred with the addition of the Thionine molecule in the hydrogen formation mechanism and that the reduction of the hydrogen ions is carried out by means of a charge transfer mechanism at all temperatures.²⁶

As can be seen from Table 1, slight changes in the inhibitor efficiency values with the rise of the temperature drawn attention to the stronger adsorption (chemisorption) of the Thionine molecule on the mild steel surface. This result can be interpreted as the fact that adsorption of the Thionine molecules and the corrosion products formed together give the inhibition of the mild steel surface together.

3.2. Evaluation of adsorption isotherm and inhibition mechanism

Considering that the molecular adsorption at the mild steel/solution interface is mainly depended on a mechanism in the form of corrosion inhibition, the relationship between the metal surface and the inhibitor has been identified by different adsorption isotherms for the Thionine. It has been determined that obey to which type isotherm of the adsorption. Five different isotherms such as Langmuir, Flory-Huggins, Temkin, Frumkin and Freundlich were tested for the adsorption of the Thionine by using surface coverage fraction (θ) values obtained from the potentiodynamic polarization measurements.

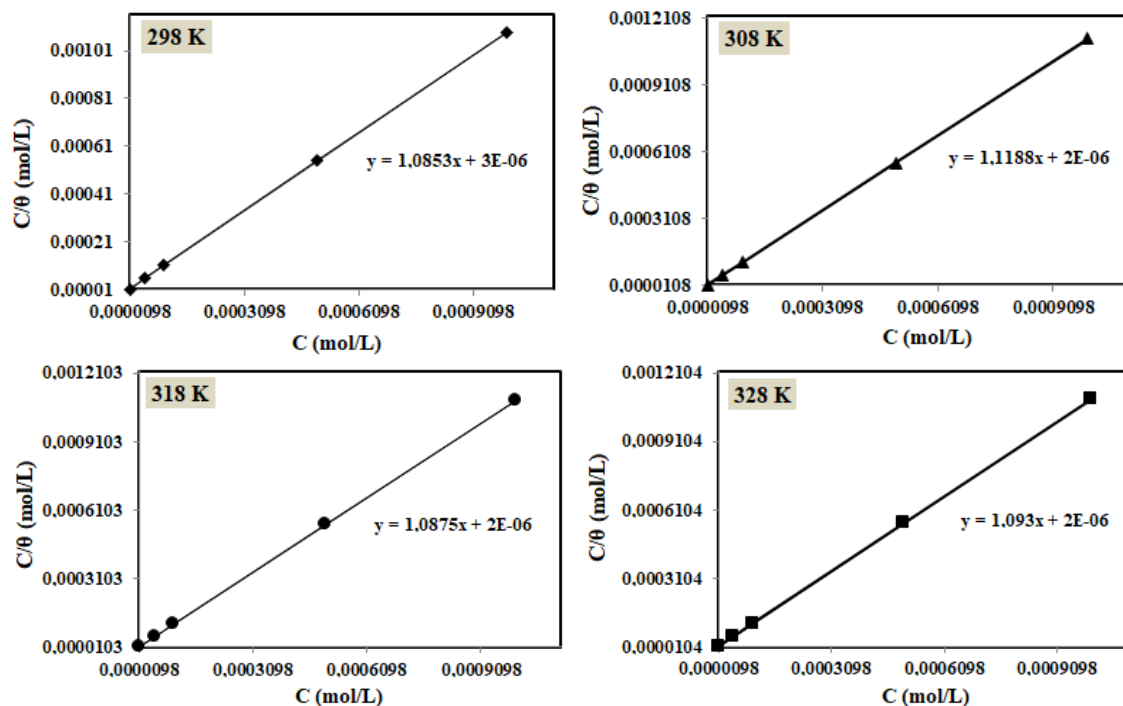


Figure 4. Langmuir adsorption isotherm curves obtained at different temperatures of Thionine inhibitor in 1.0 M HCl solution.

Among these, the best regression constant (R^2) value was obtained by the Langmuir adsorption isotherm presented in Equations (2)²⁷ and (3).²⁸

$$\frac{C}{\theta} = \frac{1}{K} + C \quad (2)$$

Where C is the Thionine concentration and K is the adsorption equilibrium constant of the adsorption process.

$$K_{ads} = \frac{1}{55.5} \exp\left(-\frac{\Delta G_{ads}^{\circ}}{RT}\right) \quad (3)$$

Where 55.5 is the molar concentration of water, R is the universal gas constant, and T is absolute temperature (in Kelvin). The plots of the Langmuir adsorption isotherms in the 298 K-328 K ranges for the five different concentrations of the Thionine are given in Figure 4, and the thermodynamic parameters such as (K_{ads}) and (ΔG_{ads}°) calculated from these isotherms are submitted in Table 2.

The values of adsorption free energy not higher than -20 kJ mol^{-1} are generally noticed in case of physical adsorption mechanism, where the interacting forces are completely electrostatic (weak) interactions. ΔG_{ads}° values, more negative than -40 kJ mol^{-1} , are characteristic for chemical adsorption mechanism.

Table 2. Thermodynamic parameters of Thionine calculated from Langmuir adsorption isotherms

Temperature (K)	K	ΔG_{ads}° (kJ mol ⁻¹)
298	333333.3	-41.46
308	500000.0	-42.46
318	500000.0	-42.46
328	500000.0	-42.46

This mechanism is constituted of chemical bonds between unpaired π -orbitals in the nitrogen, sulphur atoms, and π -electrons in the aromatic rings and unoccupied d-orbitals of the Fe metal.^{29,30} Negative ΔG_{ads}° values at all temperatures clarify that adsorption is spontaneous. Since all ΔG_{ads}° values calculated according to Eq. (3) are more negative than -40 kJ mol^{-1} (see Table 2), it can be said that the adsorption of the Thionine is both spontaneous and chemical adsorption.^{31,32}

As a result, it can be concluded that the calculated K_{ads} values are too large and ΔG_{ads}° values get negative values than -40 kJ mol^{-1} , and that they show inhibitor influence with the interactions that perform the charge transfer to make coordinated bonding from the Thionine molecule to the mild steel surface. This is also a clear indication that the layer formed on the mild steel surface is stable.

3.3. Evaluation of activation energy with Arrhenius equation

In order to examine the preventative effect of the Thionine on the corrosion of mild steel with uninhibited and inhibited solutions at each temperature, the Arrhenius equation in Eq. (4) was utilized.

$$\ln(i_{corr}) = \ln A - \frac{E_a}{RT} \quad (4)$$

Where, A is the pre-exponential factor, E_a is activation energy, i_{corr} is corrosion rate, and R is the gas constant. E_a values were calculated from slope of the plot of $\ln(i_{corr})$ against $1/T$ (see Figure 5) and the obtained values are shown in Table 3. The E_a^* value was found as $63.71 \text{ kJ mol}^{-1}$ in the uninhibited medium and it was lower in the Thionine containing medium than in the uninhibited medium (Table 3).

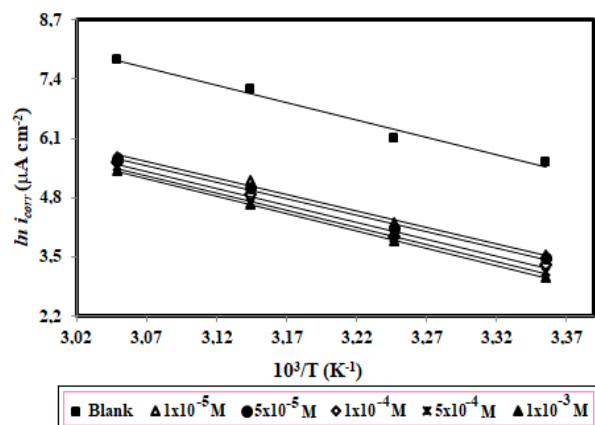


Figure 5. Arrhenius plots obtained in uninhibited and inhibited media.

Accordingly, the activation energy values obtained due to the dissolution of the metal in the solution containing the Thionine is lower than the uninhibited solution, it can be interpreted that the inhibitor molecules have protective effect on the surface with the corrosion products as a result of the dissolution of the metal and as chemically adsorbed to the metal surface with increasing temperature and forming a protective film on the surface.

According to literature findings, low or unchanged E_a^* values in inhibited solutions compared to the acidic medium indicate the chemical adsorption, otherwise physical adsorption.³³

3.4. Evaluation of surface characteristics of mild steel electrodes by FESEM and AFM analyses

Surface characteristics of mild steel electrodes have been identified by using FESEM and AFM analyses for

120 h. Figure 6 reveals both the FESEM and AFM images of uninhibited mild steel surfaces. Both images clearly spill that the surfaces in blank solution are vigorously disrupted.

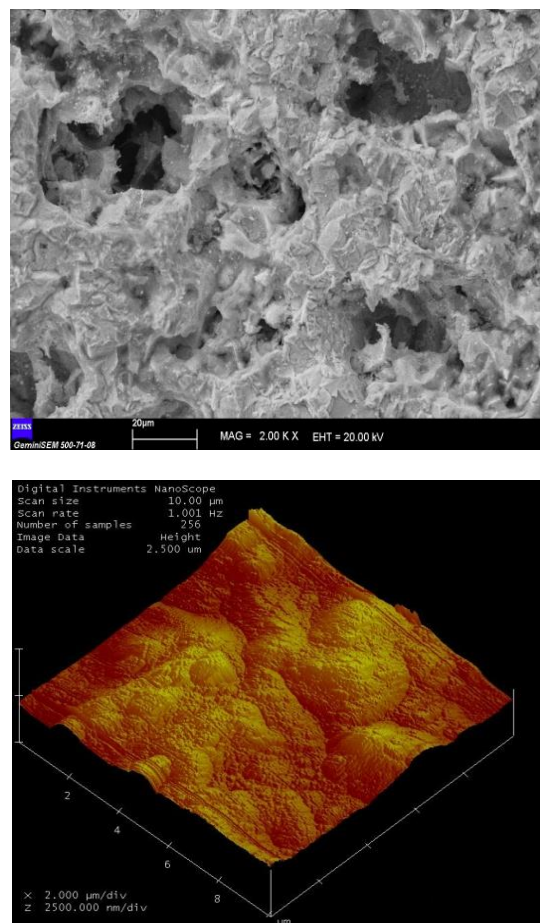


Figure 6. FESEM and AFM images of mild steel electrode immersed in 1.0 M HCl solution for 120 h.

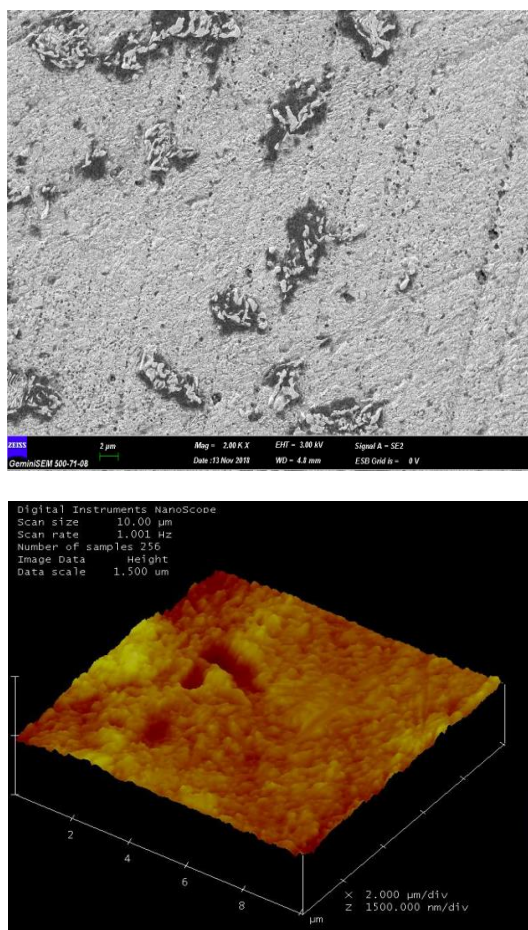
The most important feature that makes FESEM superior to SEM is that it has very high resolution. In both images of the blank solution, large dark spots are monitored in pit appearance. In this case, the electrode immersed in the blank solution is clearly oxidized and the surface is deteriorated. The AFM image of the mild steel in Figure 6 was highly affected by the corrosive solution and turned into a rough surface with large cavities. The average roughness (R_a) value of the electrode surface in the blank solution was measured as about 198 nm.

Referring to Figure 7, when an optimum concentration ($1.0 \times 10^{-3} \text{ M}$) of the Thionine was added to the medium, the cavities in the blank solution began to decrease and close.

As clearly seen from Figure 7, the surface has a smoother and straighter appearance.

Table 3. E_a^* values calculated in uninhibited and inhibited solutions

Thionine Concentration (M)	Blank	1.0×10^{-5}	5.0×10^{-5}	1.0×10^{-4}	5.0×10^{-4}	1.0×10^{-3}
E_a^* (kJ mol ⁻¹)	63.71	60.26	60.67	61.84	62.65	63.44

**Figure 7.** FESEM and AFM images of mild steel electrode immersed in 1.0 M HCl solution containing 1.0×10^{-3} M for 120 h.

This may be interpreted to show the protective effect by covering the mild steel surface just like a blanket due to the structure of the Thionine molecules. It is shown that a good preventative film layer on metal surface and also verifies the high inhibition performance. The average surface roughness value of the mild steel with 1.0×10^{-3} M the Thionine added the medium was determined to be approximately 39 nm (Figure 7). When the Thionine was added to the acidic medium, the R_a value was very small. This is another proof that the surface is smoother in the inhibited medium.

4. CONCLUSIONS

In the present study, in order to determine the effect of temperature on the corrosion behavior of the mild steel in the hydrochloric acid medium of the Thionine, the following results are summarized by electrochemical measurements:

- Thionine, which does not contain azo group in its structure and has a metachromatic effect, has been designed to be used as a commercial inhibitor at different temperatures against the corrosion of mild steel in the hydrochloric acid solution and as a result showed a high inhibitory performance.
- Electrochemical behavior of mild steel by potentiodynamic polarization (Tafel extrapolation); semi-logarithmic current-potential plots were investigated in four different temperatures in uninhibited and inhibited media. The Thionine molecule has behaved as a mixed-type inhibitor in this medium, since the increase in Thionine concentration in the acidic medium decreases both anodic and cathodic current density.
- It was determined by the surface coverage fraction values obtained from the potentiodynamic polarization measurements that the Thionine molecule was adsorbed on the mild steel surface according to the Langmuir isotherm.
- It is evidence that the Thionine molecules are chemically adsorbed onto the mild steel surface, as the activation energy value determined in the uninhibited medium is greater than the solutions containing the Thionine molecule.
- The ΔG_{ads}° values calculated at all temperatures were more negative than -40 kJ mol⁻¹, which confirmed that the Thionine molecule was adsorbed spontaneously and effectively to the mild steel surface.
- FESEM and AFM analyses verify that mild steel still has a smooth surface after immersed for 120 h in 1.0 M HCl including Thionine in comparison with blank

solution. The lower R_a value in the inhibitor-containing medium than in the uninhibited one may be put forward as a proof that the Thionine dye is very well protected by the mild steel surface.

- In the light of these experimental results, Thionine is suitable for use as an inhibitor in mild steel in the hydrochloric acid solution.

Conflict of interest

Author declares that there is no a conflict of interest with any person, institute, company, etc.

REFERENCES

- <https://nptel.ac.in/courses/113106032/16%20-%20Properties%20and%20Applications%20of%20Materials.pdf> (Retrieved December 17, 2018).
- Vitos, L.; Zhang, H.L.; Lu, S.; Al-Zoubi, N.; Johansson, B.; Nurmi, E.; Ropo, M.; Punkkinen, M.P.J.; Kokko, K. *Alloy Steel: Properties and Use First-Principles Quantum Mechanical Approach to Stainless Steel Alloys*. In: Morales E.V. (Eds). Croatia, Intech Open Access Publisher, 2011, Chap 1.
- The Balance, Steel Grades and Properties. What Are the Different Types of Steel? Adres: <https://www.thebalance.com/steel-grades-2340174> (Retrieved December 17, 2018).
- El-raouf, M.A.; El-Azabawy, O.E.; El-Azabawy, R.E. *Egypt. J. Pet.* **2015**, 24, 233–239.
- Gong, W.; Yin, X.; Liu, Y.; Chen, Y.; Yang, W. *Prog.Org. Coat.* **2019**, 126, 150–161.
- Asaad, M.A.; Ismail, M.; Tahir, M.Md.; Huseien, G.F.; Raja, P.B.; Asmara, Y.P. *Constr. Build. Mater.* **2018**, 188, 555–568.
- Al-Amierya, A.A.; Ahmed, M.H.O.; Abdullah, T.A.; Gaaz, T.S.; Kadhum, A.A.H. *Results Phys.* **2018**, 9, 978–981.
- Javadian, S.; Darbasizadeh, B.; Yousefi, A.; Ektefa, F.; Dalir Jamal Kakemam, N. *J. Taiwan Ins. Chem. Engin.* **2017**, 71, 344–354.
- Palanisamy, K.; Kannan, P.; Sekar, A. *Surf. Interfaces*, **2018**, 12, 50–60.
- Madkour, L.H.; Kaya, S.; Kaya, C.; Guo, L. *J. Taiwan Inst. Chem. E.* **2016**, 68, 461–480.
- Pareek, S.; Jain, D.; Hussain, S.; Biswas, A.; Shrivastava, R.; Parida, S.K.; Kisan, H.K.; Lgaz, H.; Chung, Ill-Min.; Behera, D. *Chem. Eng. J.* **2019**, 358, 725–742.
- Madkour, L.H.; Kaya, S.; Guo, L.; Kaya, C. *J. Mol. Struct.* **2018**, 1163, 397–417.
- El Nemr, A.; Moneer, A.A.; Khaled, A.; El Sikaily, A.; El-Said, G.F. *Mater. Chem. Phys.* **2014**, 144, 139–154.
- Singh, A.; Lin, Y.; Liu, W.; Yu, S.; Pan, J.; Ren, C.; Kuanhai, D. *J. Ind. Eng. Chem.* **2014**, 20, 4276–4285.
- Chen, B.Y.; Xu, B.; Yueh, P.L.; Han, K.; Qin, L.J.; Hsueh, C.C. *J. Taiwan Ins. Chem. Engin.* **2015**, 51, 63–70.
- Ho, P.I.; Kumar, G.G.; Kim, A.R.; Kim, P.; Nahm, K.S. *Bioelectrochemistry*, **2011**, 80, 99–104.
- Ackroyd, W. *Chem. News* **1876**, 33, 60.
- Ehrlich, P.; *Arch. Anat. Physiol.* **1879**, 36, 166–169.
- Pradeep D'mello, A.X.; Sylvester, T.V.; Ramya, V.; Britto, F.P.; Shetty, P.K.; Jasphin, S. *Int. J. Adv. Health Sci.* **2016**, 2-10, 12–17.
- Khayyat, S.A.; Akhtar, M.S.; Umar, A.; *Mater. Lett.* **2012**, 81, 239–241.
- Rahimnejad, M.; Najafpour, G.D.; Ghoreyshi, A.A.; Shakeri, M.; Zare, H. *Int. J. Hydrogen Energ.* **2011**, 36, 13335–13341.
- Umoren, S.A.; AlAhmary, A.A.; Gasem, Z.M.; Solomon, M.M. *Int. J. Biol. Macromol.* **2018**, 117, 1017–1028.
- Tasić, Ž.Z.; Petrović Mihajlović, M.B.; Radovanović, M.B.; Simonović, A.T.; Antonijević, M.M. *J. Mol. Struct.* **2018**, doi: 10.1016/j.molstruc.2018.01.031.
- Solmaz, R. *Corros. Sci.* **2014**, 79, 169–176.
- Özkır, D.; Kayakırlmaz, K.; Bayol, E.; Gürten, A.A.; Kandemirli, F. *Corros. Sci.* **2012**, 56, 143–152.
- Chauhan, D.S.; Ansari, K.R.; Sorour, A.A.; Quraishi, M.A.; Lgaz, H.; Salghi, R. *Int. J. Biol. Macromol.* **2018**, 107, 1747–1757.
- Özkır, D. *J. Electrochem. Sci. Technol.* **2019**, 10 (1), 37–54.

DOI: <http://dx.doi.org/10.32571/ijct.514287>

E-ISSN:2602-277X

28. Özkar, D. *OHU J. Eng. Sci.* **2018**, 7(2), 993–1003.
29. Wysocka, J.; Cieslik, M.; Krakowiak, S.; Ryl, J. *Electrochim. Acta* **2018**, 289, 175–192.
30. Obot, I.B.; Obi-Egbedi, N.O.; Umoren, S.A. *Corros. Sci.* **2009**, 51, 276–282.
31. Popova, A.; Sokolova, E.; Raicheva, S.; Christov, M. *Corros. Sci.* **2003**, 45, 33–58.
32. Noor, E.A. and Al-Moubaraki, A.H. *Mater. Chem. Phys.* **2008**, 110, 145–154.
33. Singh, D.K.; Ebenso, E.E.; Singh, M.K.; Behera, D.; Udayabhanu, G.; John, R.P. *J. Mol. Liq.* **2018**, 250, 88–99.

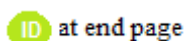
 ORCID

 <https://orcid.org/0000-0002-8096-5755> (D. ÖZKIR)



The theoretical investigation of HOMO, LUMO, thermophysical properties and QSAR study of some aromatic carboxylic acids using HyperChem programming

Ajoy KUMER¹, Md Nuruzzaman SARKER², Sunanda PAUL³



¹Department of Chemistry, European University of Bangladesh, Dhaka-1216, Bangladesh

²Department of Physics, European University of Bangladesh, Dhaka-1216, Bangladesh

³Department of Biochemistry and Molecular Biology, University of Chittagong, Chittagong, Hathazari-3443, Bangladesh

Received: 03 November 2018, Revised: 05 March 2019; Accepted: 07 March 2019

*Corresponding author e-mail: kumarajoy.cu@gmail.com

Citation: Kumer, A.; Sarker, M. N.; Paul, S. *Int. J. Chem. Technol.* 2019, 3 (1), 26-37

ABSTRACT

Growing the molecular mechanism of chemicals, thermochemical and biological interactions is considered as the ultimate goal of computational chemistry. Some thermodynamic parameters such as free energy, entropy, dipole moment, binding energy, nuclear energy, electronics energy, heat of formation, and QSAR (quantitative structure activity relationship) properties of molecules like charge density, surface area grid, volume, LogP, polarizability, refractivity, molecular mass, and reactivity properties of molecules like HOMO (the highest occupied molecular orbital), LUMO (the lowest unoccupied molecular orbital), HUMO (the highest unoccupied molecular orbital)-LUMO gap, ionization potential and electron affinity were determined using the HyperChem 8.0.10 program. The computed QSAR parameters have a significant role in the estimation of the biological activity and metabolism in the human body.

Keywords: HyperChem 8.0.10, aromatic carboxylic acid, QSAR, HOMO-LUMO.

HyperChem programı kullanarak bazı aromatik karboksilik asitlerin HOMO, LUMO, termoplastik özellikleri ve QSAR incelemesinin teorik araştırılması

ÖZ

Kimyasalların moleküler mekanizmasını geliştirmek, termokimyasal ve biyolojik etkileşimler hesaplamalı kimyanın temel amacı olarak düşünülmektedir. Moleküllerin serbest enerjisi, entropisi, dipol momenti, bağlanma enerjisi, nükleer enerjisi, elektronik enerjisi, oluşum ısısı gibi bazı termodinamik parametreleri ve yük yoğunluğu, yüzey alanı ızgarası, hacim, LogP, polarizasyon, kırılma, moleküler kütle gibi QSAR (kantitatif yapı aktivite ilişkisi) özellikleri, ve HOMO (en yüksek dolu moleküler orbital), ve LUMO (en düşük boş moleküler orbital), HUMO (en yüksek boş moleküler orbital)-LUMO enerji aralığı, iyonlaşma potansiyeli ve elektron afinitesi gibi reaktivite özellikleri, HyperChem 8.0.10 programı kullanılarak belirlenmiştir. Hesaplanan QSAR parametreleri, insan vücudundaki biyolojik aktivite ve metabolizmanın tahmininde önemli bir role sahiptir.

Anahtar Kelimeler: HyperChem 8.0.10, aromatik karboksilik asit, QSAR, HOMO-LUMO.

1. INTRODUCTION

Benzoic acid is a colorless crystalline solid and a simple aromatic carboxylic acid,¹ which was for a long time known as the source of a large number of synthesis of organic compounds.²⁻³ Benzoic acid occurs naturally in many plants and serves as an intermediate in the

biosynthesis of many secondary metabolites.⁴⁻⁵ Salts and esters of benzoic acid known as benzoates are used as food preservatives,⁶⁻⁷ manufacture of alkyl resins and drilling mud additive, a rubber polymerization activator and retardant⁸ and it has a great effect on growth performance, nutrient digestibility, nitrogen balance, gastrointestinal microflora and parameters of microbial

metabolism in piglets.⁹ Many organic compounds were synthesized from benzoic acid in field of industries. Its use in the production of glycol benzoates for the application of plasticizer in adhesive formulations is increasing.¹⁰⁻¹² About 65% yield was obtained for traditional process. Most of the commercial benzoic acid is converted directly to phenol and caprolactam.¹³⁻¹⁴ In United States of America, the production capacity of benzoic acid is estimated at 139,000 tons per year, which are used for both of the domestic and industrial uses as raw materials.

Benzoic acid is converted to its salts and esters for use as a preservative application in foods, drugs, and personal product. In case of the treatment of fungal skin disease, benzoic acid is the vital component of benzoin resin and ointments and other diseases such as tinea, ringworm, and athlete's foot.¹⁵⁻¹⁷ On the other hand, the 2-nitrobenzoic acid, 2-chlorobenzoic acid, 2-methylbenzoic acid, and 2-hydroxybenzoic acids are the derivative of benzoic acid which is widely used in food industry, the pharmaceutical industry, chemical industry, agricultural land and with research purpose.¹⁸⁻¹⁹ Due to estimate, the chemical and physical properties are a way of time and money. To save the time and cost, computational chemistry is the best tools to evaluate the chemical and biological properties.

Accordingly, an intimate relationship between the structure of a compound, in physicochemical, chemical reactivity, bioactivity, and biodegradation study should be computationally established as a "road map" of expectations, conditions of use, prediction and prevention.²⁰⁻²¹ In this context, the computational methods for modeling the chemical-biological interaction of a compound with organisms have become known as quantitative structure-activity relationships (QSAR) methods have come to the forefront.²¹⁻²³ Especially in the last two decade, a regulatory framework in variety of mareas such as, toxicological,²⁴⁻²⁵ assessment of metabolic genotoxicity, screening of chemicals with bioaccumulation potential,²⁶ food and organic chemicals safety have been performed by computational analysis, and also thermophysical properties have been determined using computational programmes to save money and time. Considering their molecular structural relationship, HOMO, LUMO, and quantum chemical properties, and LogP plays a role in the determination of the chemical reactivity, biological activity and hydrophobicity and hydrophobicity of chemicals in relation with living cells activity and associated mechanistic interactions.

1.1. Theoretical background

1.1.1. Fundamentals of thermodynamics

Thermodynamics is a branch of physics and physical chemistry where describe the properties of the general

macroscopic physical systems and their theory of evolution, and it calculates all types of changes and heat in the physical and chemical processes.²⁷ The different activities of living occur with the conservation of energy which is governed by the physical law of altering one form of energy to another.²⁸

A thermodynamic system consists of definite macroscopic region or space in the universe. This system has a specific volume consisting of molecules and atoms with continuous movement and concussion by the interaction with the external surrounding. The internal properties and its interaction with the surrounding determine the system behavior.²⁹

The thermodynamics systems are of three types taking into account the interaction with the external environment which are: (i) Closed system: only the transfer of energy but not mass across the boundary. (ii) Open system: Transfer of both mass and energy across the boundary. (iii) Isolated system: Do not transfer both mass and energy across the boundary.

From above all three, a thermodynamic system of all living organisms is the open system and biological process is the irreversible thermodynamic process where the change of energy and mass take place. A thermodynamic system, when steady state, is called an equilibrium system where all the parameters do not vary with respect to time, and change by the surrounding involving the mass transport. A thermodynamic system can switch from initial state through the intermediate state to final state which is called transformation of state or thermodynamics process.³⁰⁻³¹

Some properties like temperature (T), refractive index (n), density (ρ) and hardness of an object (η) are intensive properties, and also some properties like the mass (m), and the volume (V) are extensive properties. Surface area and some external parameters dependence of the thermodynamic system on the environment like pressure, temperature, density, electrical polarization, the coefficient of the tension of a liquid.³²

1.1.2. Molecular modeling

Molecular modeling which is a useful implement in many fields such as chemistry, physics, biology, medicine, and pharmacy allows graphical representation of a molecular configuration and calculation of physicochemical properties and biological properties. In the pharmacological researchs, drug design, biological chemistry, and molecular biology, to do continuous researchs and design new molecules by molecular modeling of computational software has become easy. Instigated in various molecular modeling programs, these methods are used to determine the properties of drugs, and bioactive molecule found in the draft before the actual synthesis. Molecular modeling methods are numerous, mostly relying on the principles of quantum mechanics and Schrödinger's equation solving.³³

DOI: <http://dx.doi.org/10.32571/ijct.478179>

ISSN:2602-277X

The most important methods that are used in molecular modeling programs are *ab-initio* methods, semi-empirical methods,³⁴ Density function theory.³⁵

The most important methods of semi-empirical: AM1, PM3. In addition of the methods mentioned above, in recent years there was an expansion of the two methods, the method of molecular dynamics and Monte Carlo method, which refers to theoretical models that takes an intermediate between theory and experiment, called numerical methods.³⁶

Among the most used molecular modeling programs, the common software is named Spartan, Gaussian, and HyperChem. Most molecular modeling techniques are worked based on the principles of quantum mechanics and Schrödinger's equation solving. Depending on the parameters molecular system has been studied that is intended to be obtained by choosing one or another method.³⁷

2. COMPUTING MATERIALS AND METHODS FOR SIMULATION

HyperChem 8.0.1 is a path of molecular modeling program which permits to build and analyze different molecular structures and determine their physicochemical, thermo-chemical, and biological properties. To performing this work, a high core i7 computer, and HyperChem software were used.

The PM3 method is derived from Parametric Method number 3 from computational chemistry and included in the semi-empirical method for the quantum calculation of molecular structure. PM3 was used the Hamiltonian and it is parameterized to reproduce a large number of molecular properties.³⁸

In order to create the spatial chemical structure of each calculated molecule, the two-dimensional structure of the molecule shall be built step-by-step by drawing. Then hydrogen atoms are automatically added from building option and chemical structure is automatically adjusted from model build option. In the first step, the optimization of main structure, bond length, bond order, and partial charges were obtained.

For optimization, MP3 from semi empirical method was ran up and running the option computing using the algorithm Polak–Ribiere was done with maximum gradient set at 0.001 kcal mol⁻¹ for calculation of free energy, entropy, dipole moment, binding energy, nuclear energy, electronics energy, heat of formation, the energy of frontier orbitals, HOMO (Highest Occupied Molecular Orbital) and LUMO (Lowest Unoccupied Molecular Orbital), and QSAR properties of molecules like charge density, surface area grid, volume, LogP, polarizability, refractivity, molecular mass.

3. RESULTS AND DISCUSSION

3.1. Optimized structure

A representation of the molecular structure optimized which contains the values of the reactivity indices is called the reactive molecular diagram. The optimized structure of optimized molecules using the HyperChem 8.0.10 software is represented in [Figures 1 and 2](#).

The symmetry is a very powerful tool established on the basis of HyperChem. The benzoic acid, 2-nitrobenzoic acid, 2-chlorobenzoic acid, 2-methylbenzoic acid, and 2 hydroxybenzoic acids are considered as the class symmetry, the molecules of this group are planar and they have only one element of symmetry and the plane of the molecule.

3.2 The atomic charges computed by HyperChem

It is seen from [Figure 3](#) that the negative charges are located near C and O atoms (the highest negative value is -0.404 in O, -0.10 atom) and the positive charges are located near H atoms (the highest positive value is 0.450).

3.3. Bond length

In general, the bond length between two atoms is approximately the sum of the covalent radii of the two atoms. For covalent bonds, bond energies and bond lengths depend on many factors like electron affinities, sizes, electro-affinity of atoms involved in the bond, differences in their electronegativity, and the overall structure of the molecule shown in [Figure 4](#). There is a general trend in that the shorter the bond length, the higher the bond energy. Similar bond length indicates the similarity and molecular symmetry.

3.4. Bond order

The higher the bond order indicates the stronger the pull between the two atoms and the shorter the bond length. The shorter bond length indicates the higher required energy. Bond orders in different molecules optimized by HyperChem are shown in [Figure 5](#).

3.5. HOMO-LUMO

The energy levels of the molecular orbitals order HOMO (Highest Occupied Molecular Orbital) and LUMO (Lowest Unoccupied Molecular Orbital) for different aromatic carboxylic acid molecules give information on the possible electronic transition. The HOMO and LUMO also indicate the electrophilic and nucleophilic attraction in the molecule. The LUMO-HOMO gap is the most important parameter for the chemical reactivity. The shorter LUMO-HOMO gap is considered as the high reactivity, they are highlighted in [Figure 6](#) (color: green is the positive value and blue is the negative value).³⁹⁻⁴⁰

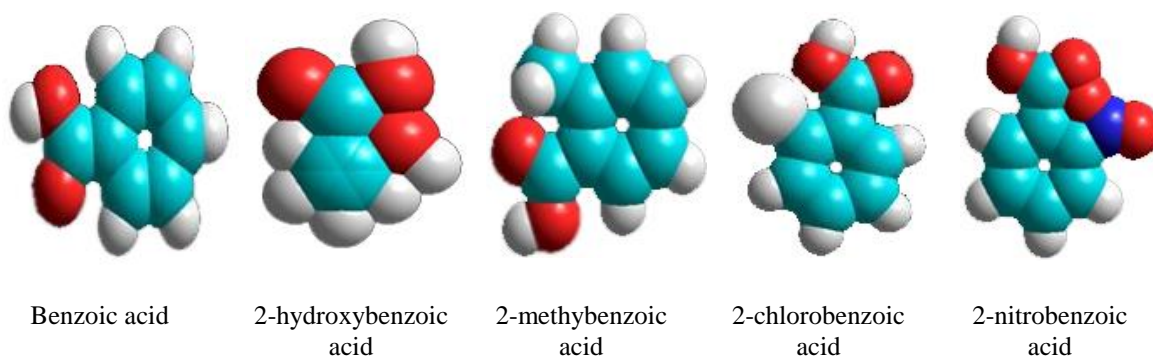


Figure 1. Optimized structure representing ball shape, Color: Red is oxygen, cyan is carbon, white is hydrogen, nitrogen is blue, chlorine is white in large size.

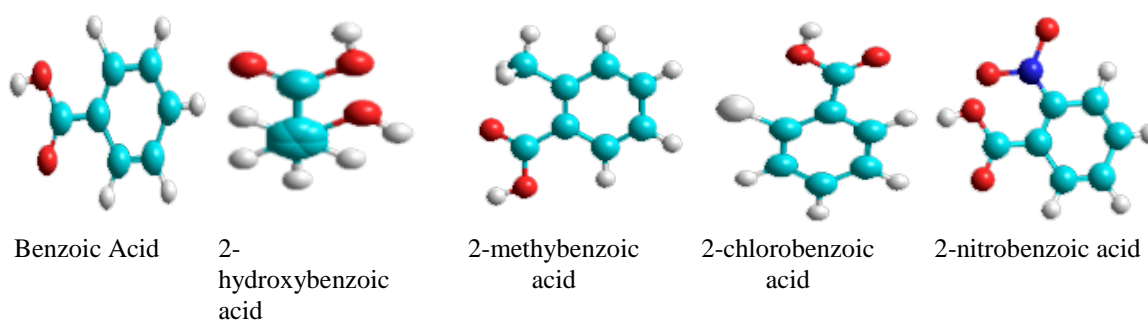


Figure 2. Optimized structure in the cylinder shape, Color: Red is oxygen, cyan is carbon, white is hydrogen, nitrogen is blue, chlorine is white in large size.

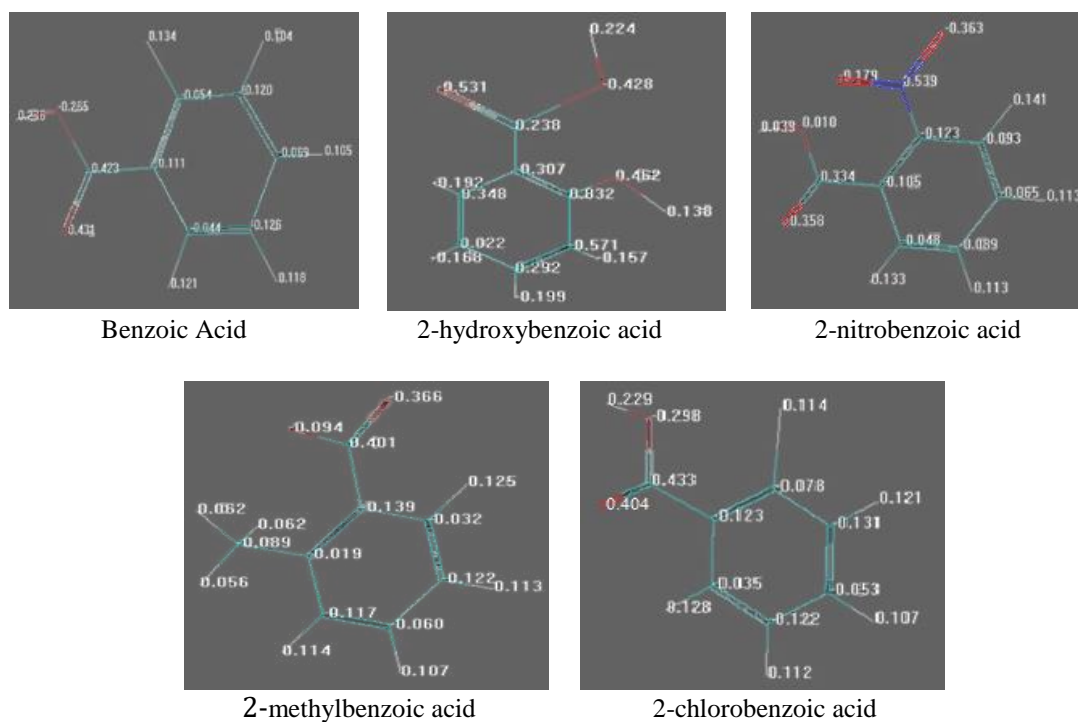


Figure 3. The atomic charges in the molecules computed by HyperChem.

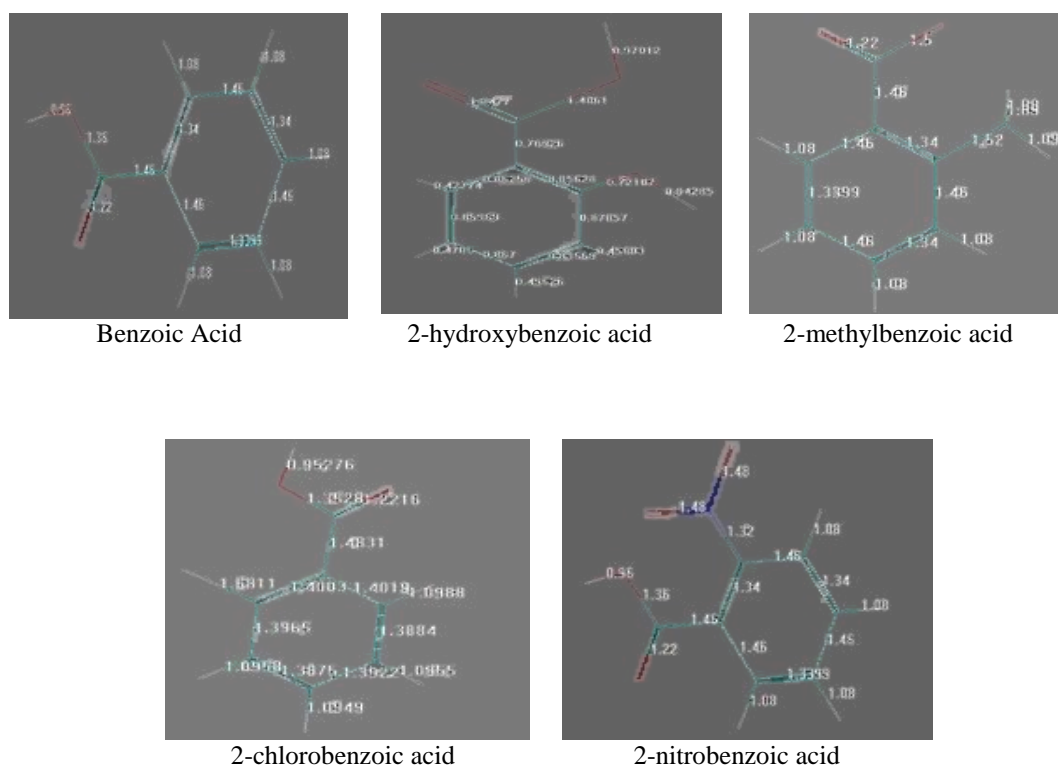


Figure 4. Bond length in different molecules optimized by HyperChem.

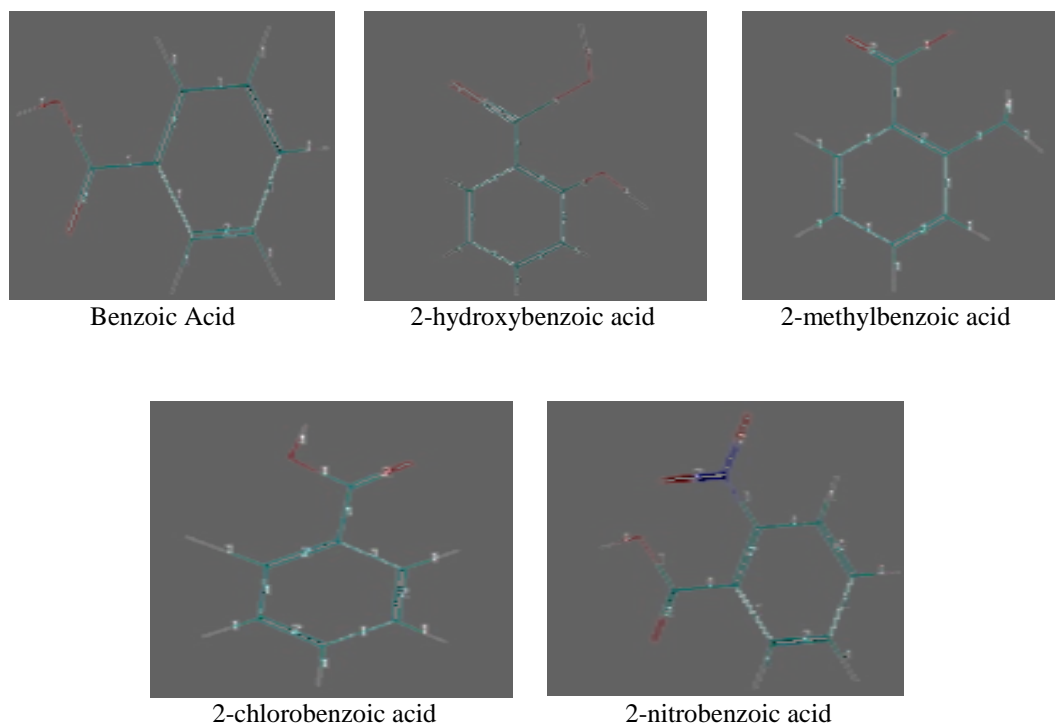


Figure 5. Bond order in different molecules optimized by HyperChem.

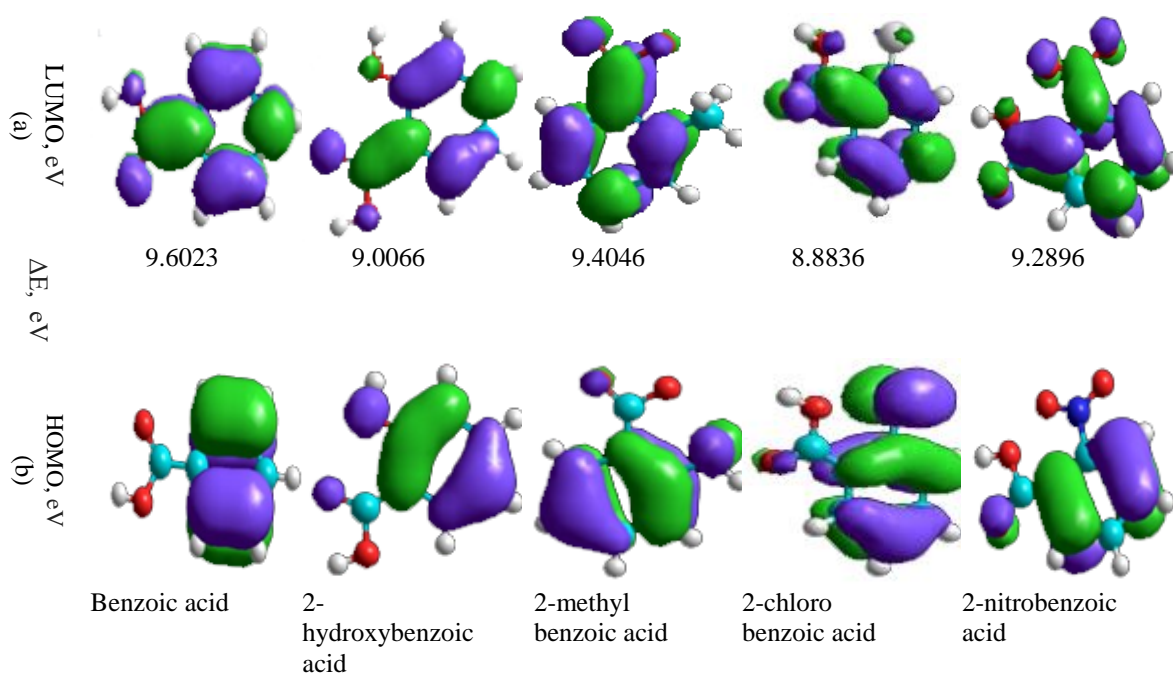


Figure 6. The frontier orbitals: a) LUMO and b) HOMO.

Table 1. Data for HOMO, LUMO, IP, EA, and LUMO- HOMO gap (ΔE)

	Benzoic acid	2-hydroxybenzoic acid	2-methylbenzoic acid	2-chlorobenzoic acid	2-nitrobenzoic acid
HOMO, eV	-10.1358	-9.5180	-10.0681	-9.5955	-10.8299
LUMO, eV	-0.5335	-0.5114	-0.6635	-0.7119	-1.5403
ΔE , (LUMO-HOMO)	9.6023	9.0066	9.4046	8.8836	9.2896
Ionization potential (I), eV	-10.1358	-9.5180	-10.0681	-9.5955	-10.8299
Electron affinity (A), eV	-0.5335	-0.5114	-0.6635	-0.7119	-1.5403

In the Figure 6, all of molecules have almost near HOMO LUMO gap that is from 8.88 to 9.60 eV.

The electrophilic (Positive charge groups or atoms) attack to the most likely to the atomic site with a high density of orbital HOMO, while nucleophilic (Negative charge groups or atoms) attack LUMO that is correlated with atomic high-density of orbital LUMO.

The ionization potential (I) and electron affinity (A) have been estimated from the HOMO and LUMO energy values like as IP = Negative of the energy of HOMO, and EA = Negative of the energy of LUMO (Table 1).

3.6. Thermophysical properties

Thermophysical properties optimized from HyperChem are given in Table 2.

3.7. Characterization by NMR

The ^1H NMR spectroscopy analysis in view of shielding and shift plotting, coupling and shielding tensor which are given in Figure 7. In measurements of nuclear magnetic moments, a correction must be made

for the magnetic field ascending from the motions of the molecular electrons which are induced by the externally applied field. The "chemical effect" which is considered as the chemical shift commonly, was used now for structural determination of molecules. The calculation of the second order paramagnetic contribution is used for shielding calculation perturbation theory. The chemical shift or magnetic shielding as a number associated with each resonant nucleus, in reality, the shielding is a tensor quantity. The shielding phenomena have to be described by a shielding tensor instead of a scalar number to easily calculate the structure of molecules. In Figure 7, if

shields and shift consists of three bars at which blue indicates the shielding, green indicates the chemical shift of proton and paste color indicates the tau. On the other hand, the shielding tensor different color indicates the different proton environment. In the last view, the proton coupling indicates the proton-proton coupling by different color bar.

On the other hand, the shielding tensor different color indicates the different proton environment. In the last view, the proton coupling indicates the proton-proton coupling by different color bar.

Table 2. Thermophysical properties optimized from HyperChem

Properties	Benzoic acid	2-hydroxybenzoic acid	2-methyl benzoic acid	2-chloro benzoic acid	2-nitrobenzoic acid
Total energy, (kcal mol ⁻¹)	-348030.6	-41446.25	-38253.4	-41751.5	-51653.70
Free energy, (kcal mol ⁻¹)	-348030.6	-41446.1	-38253.4	-41751.5	-51653.70
Entropy, (kcal mol ⁻¹ deg ⁻¹)	0	0	0	0	0
Heat capacity, (kcal mol ⁻¹ deg ⁻¹)	0	0	0	0	0
Dipole moment, (D)	0	0	0	0	0
RMS gradient, (kcal mol ⁻¹)	0.9482	0.093	0.6339	0.2354	4.5660
Binding energy, (kcal mol ⁻¹)	-1694.629	-1664.2025	-1975.9445	-1674.881	-1865.970
Heat of formation, (kcal mol ⁻¹)	-66.2537	23.3164	-72.8905	-70.0334	-57.9941
Nuclear energy, (kcal mol ⁻¹)	113121.321	134964.4467	141280.465	139147.969	195423.2914
Electronic energy, (kcal mol ⁻¹)	4	9	9	9	9
Electronic energy, (kcal mol ⁻¹)	-146925.93	-176413.38	-179533.85	-180899.50	-247076.30

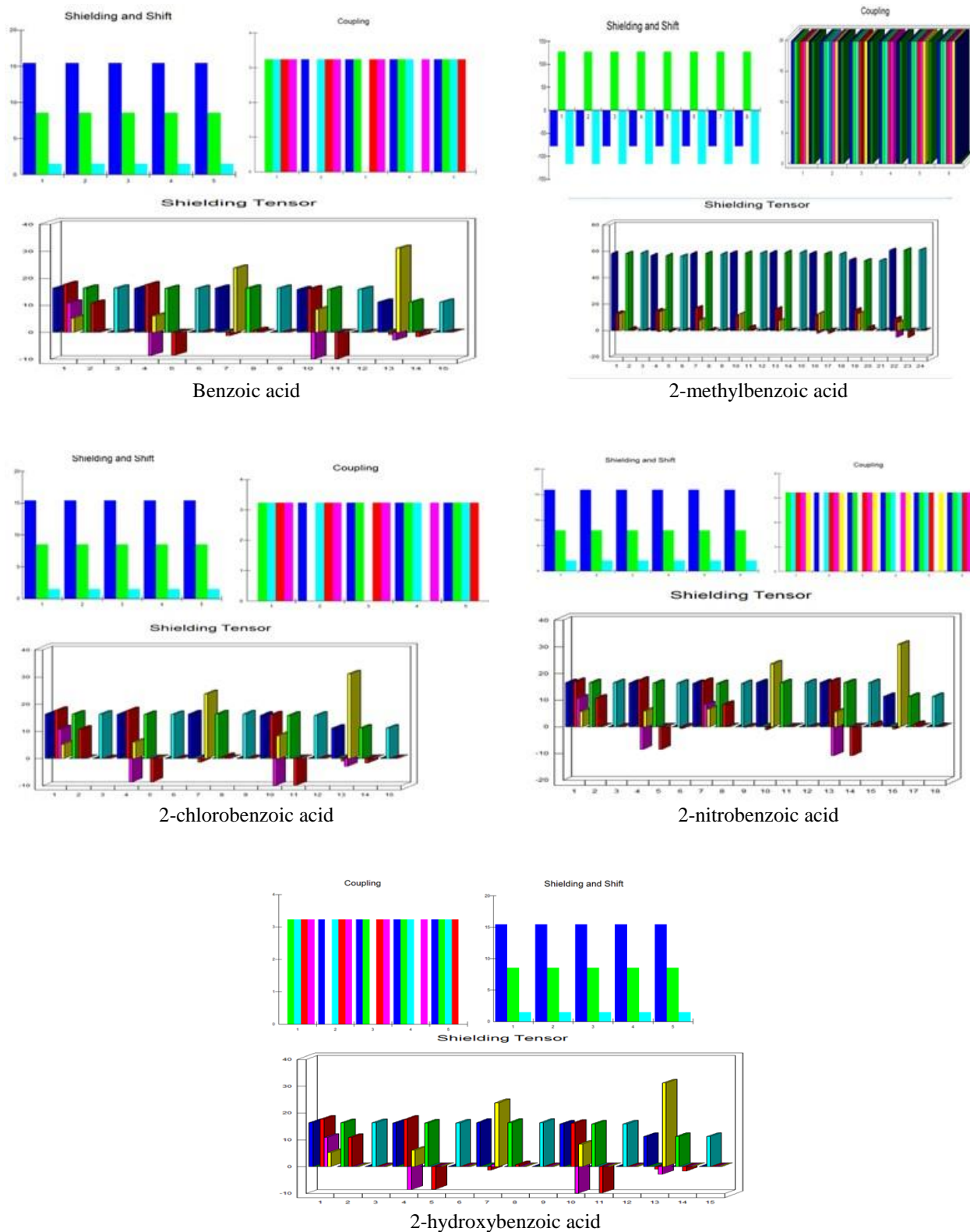


Figure 7. Shielding and shift, coupling and shielding tensor.

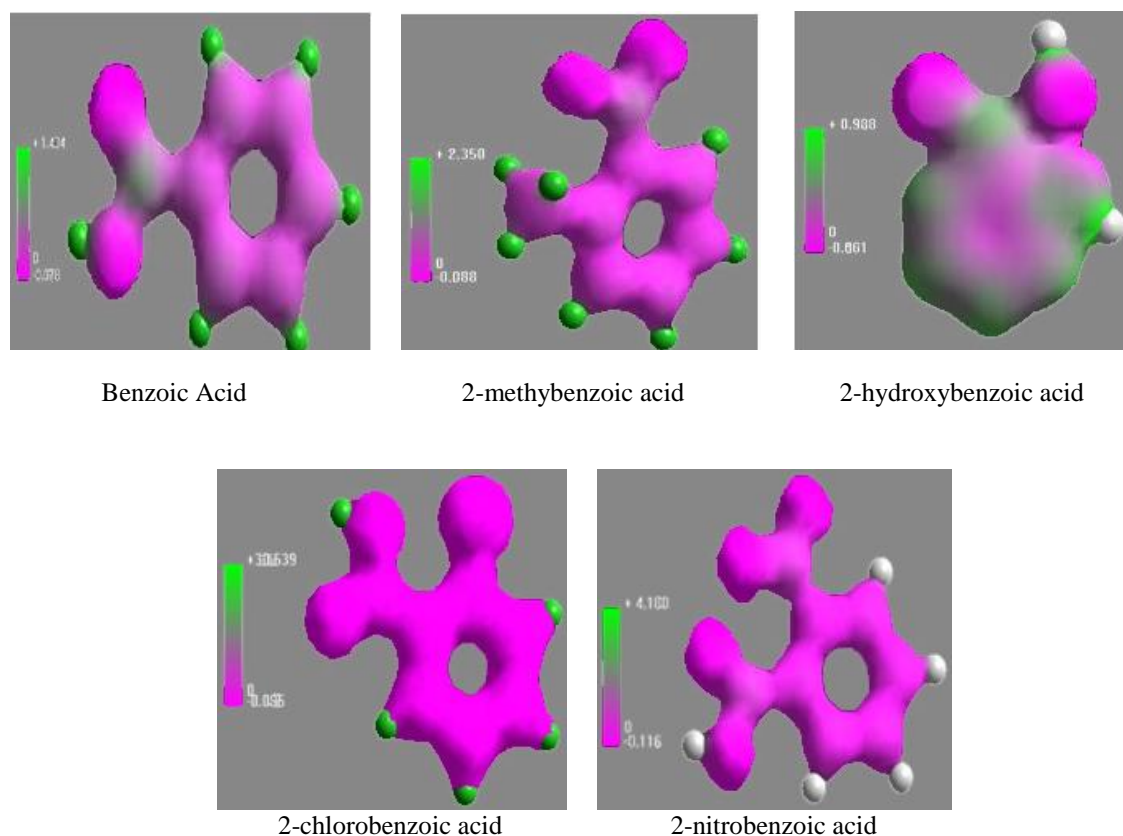


Figure 8. The 3D geometry of the distribution electrostatic potential.

Table 3. Data of electrostatic potential energy difference of two levels

	Benzoic acid	2-hydroxy benzoic acid	2-methyl benzoic acid	2-chloro benzoic acid	2-nitro benzoic acid
E1	1.434	2.350	0.988	30.539	4.180
E2	0.078	0.088	0.061	0.095	0.116
ΔE	1.358	2.262	0.927	30.44	4.064

Here, E1= Electrostatic potential energy in positive value, E2= Electrostatic potential energy in negative value, and ΔE = Electrostatic potential energy difference of two level.

3.8. Biological activity of optimized molecules

3.8.1. The distribution electrostatic potential due to 3D mapped structure

The stability of the studied molecular structure is given by the higher negative values of total energy. The biological activity of a compound can be estimated on the

basis of the energy difference (ΔE) frontier orbitals. This difference, ΔE represents the electronic excitation energy of molecule. According to the mechanism of antimicrobial activity and antimicrobial agents of bioactive molecules, the positive charge end of molecules is responsible for damage the plasma membrane of pathogens.⁴¹ To kill the different human pathogenic microorganisms, the charge region of molecules was used as the biological active part in the molecule. In this case, the most important factors are explained that the higher surface area and higher positive and negative charge is considered as the high antimicrobial active molecule. The electrostatic potential in view of the 3D mapped structure

Table 5. Data of QSAR study

	Benzoic acid	2-hydroxybenzoic acid	2-methyl benzoic acid	2-chloro benzoic acid	2"-nitro benzoic acid
Partial charge (e)	0.0	0.0	0.0	0.0	0.0
Surface Area (grid)	280.25	313.13	297.04	294.48	305.75
Volume, Å ³	407.24	461.61	450.99	442.41	457.69
Hydration Energy	-6.82	13.54	-6.07	-5.27	-11.47
LogP	0.98	-0.04	1.14	0.76	-3.70
Refractivity, Å ³	36.98	38.58	41.24	41.67	42.17
Polarizability, Å ³	12.99	13.63	14.28	14.92	14.83
Mass (amu)	122.12	138.12	136.15	156.57	162.12

indicates positive and negative charge region and the charged surface area in a molecule that is considered as the best tools to estimate the biological activity parameters.⁴²

The three-dimensional geometry of molecular electrostatic potential distribution highlights the existence of three regions with increased electronegativity in which oxygen and chlorine atoms are involved, and which play a role in their coupling to different structures in which ions are positively charged. From Table 4, it is found that the 2-chlorobenzoic acid shows high electrostatic potential energy difference of two levels due to having chlorine and highly bioactive than nitrobenzoic acids.

The surface distribution of molecular electrostatic potential is an indicator of the specific reactive regions of the molecule given in Figure 8.

3. 9. Qquantitative structure-activity relationships (QSAR)

Correlation of the molecular structure or properties are derived from a molecular structure with a particular chemical or biochemical activity. This method is widely used in pharmaceutical chemistry in the environment and in the search for certain properties. Data of QSAR study are given in Table 5.

3.9. 1. Binding Energy

The binding free energy of the optimized molecules is calculated by performing a docking process. The molecule with minimum binding energy will have the maximum binding affinity. The binding free energy of the designed molecules is obtained by eliminating the energy of the main molecule. Having the maximum binding affinity indicates as the best molecule for drug and leads molecules targeting computationally. We can find out the drug binding affinity by using the fitness of the drug, which can bind to the target molecule during the docking process and the second way is to use Gibbs free energy calculations. According to the more negative value, we can consider a more effective drug. As seen from Table 2, it is found that the binding energy, which is almost the same in benzoic acid, 2-hydroxybenzoic acid, and 2- chlorobenzoic acid from-to 1695 (kcal mol⁻¹). On the other hand, the 2-methyl 1664 benzoic acid shows the higher binding energy of -1975.9445 where nitrobenzoic acid has -1865.970 (kcal mol⁻¹).

3.9.2. Surface area

In the case of the biological activity of a molecule, the surface area is considered as the important parameter. Greater charge surface area of a molecule can possible to kill more pathogens. The charged distribution from

electrostatic potential completely depends on the surface area. The greater positive charge surface area means the higher biological activity. As seen from Table 4, it is illustrated that 2-methylbenzoic acid and 2-chlorobenzoic acid are near 195 to 197 where 2-hydroxybenzoic acid has 313 and benzoic acid has 280.

3.9.3. Hydration Energy

The hydration energy is defined as the energy absorbed when the substance is dissolved in water. The lower hydration energy is considered as the greater capacity to dissolve in water so that it acts as the hydrophilic nature and predict the best properties of the drug. The 2-hydroxybenzoic acid and 2-nitrobenzoic acid are -11.0 to 13.0 kcal mol⁻¹ and all other are near about 6.00 kcal mol⁻¹.

3.9.4. LogP

A negative value of LogP indicates the hydrophilicity and positive LogP indicates the hydrophobicity. The both of hydrophilicity and hydrophobicity play an important role in biochemical interactions and bioactivity. Hydrophobic drugs tend to be more toxic because, in general, are kept longer, have a wider distribution in the body, are somewhat less selective in their binding to molecules and finally are often extensively metabolized. Therefore ideal distribution coefficient for a drug is usually intermediate (not too hydrophobic nor too hydrophilic). From the data in Table 4, it can be seen that 2-hydroxybenzoic acid has -0.04 value that indicates lower hydrophobicity, and nitrobenzoic acid show a higher hydrophobicity. All other three molecules show hydrophilicity range from 0.98 to 1.15.

4. CONCLUSIONS

The semi-empirical PM3 method of the program HyperChem 8.010 was used to characterize and compute benzoic acid, 2-nitrobenzoic acid, 2-chlorobenzoic acid, 2-methylbenzoic acid, and 2-hydroxybenzoic acid. The physicochemical parameters and thermodynamic properties were estimated for a specific use to each molecule including 3D structure, bond lengths, the atomic charges, total energy, free energy, entropy, dipole moment, formation energy, binding energy, electrostatic energy, and nuclear energy.

The molecular descriptors QSAR provided the calculation of charge, surface area, volume, hydration energy, LogP, refractivity, polarizability, and molecular mass. The most important properties for biological chemistry, reactivity and drug design, the HOMO, LUMO, LUMO-HOMO gap, ionization potential, electron affinity, and electrostatic potential in case of the charge distribution in molecule were optimized and recorded using semi-empirical modeling methods.

The ¹H NMR was evaluated by molecular modeling programs. Obtaining by modeling the distribution of

molecular electrostatic potential reactive sites leads to the identification and characterization of the molecules. It is summarized that the resulted optimized molecules of aromatic carboxylic acid were developed a comparative study on their chemical reactivity, thermo-chemical profile and biological activity in view of theoretical studies.

ACKNOWLEDGEMENTS

We are thankful to Prof. Dr. Mukbul Ahmed Khan Vice Chancellor of European University of Bangladesh for research opportunity and also thankful to Mr. Zemam Ahmed, Senior IT officer, ICT Department, European University of Bangladesh for all kind of technical supports.

Conflict of interest

Authors declare that there is no a conflict of interest with any person, institute, company, etc.

REFERENCES




- Bridges, J.; French, M.; Smith, R.; Williams, R. *Biochem. J.* **1970**, 118, 47-51.
- Chou, S.; Huang, C. *Chemosphere* **1999**, 38, 2719-2731.
- Nayak, J.; Sahu, S.; Kasuya, J.; Nozaki, S. *Appl. Surf. Sci.* **2008**, 254, 7215-7218.
- Mroz, Z. *Advances in Pork Production* **2005**, 16, 169-182.
- Doherty, H. M.; Selvendran, R. R.; Bowles, D. J. *Physiol. Mol. Plant P.* **1988**, 33, 377-384.
- Hazan, R.; Levine, A.; Abeliovich, H. *Appl. Env. Microbiol.* **2004**, 70, 4449-4457.
- Salmond, C. V.; Kroll, R. G.; Booth, I. R. *J. Gen. Microbiol.* **1984**, 130, 2845-2850.
- Sakata, Y.; Ponec, V. *Appl. Catal A- GEN.* **1998**, 166, 173-184.
- Kluge, H.; Broz, J.; Eder, K. *J. Anim. Physiol. An. N.* **2006**, 90, 316-324.
- Arendt, W. D.; Bohnert, T. J.; Holt, M. S. Google Patents, 2001.
- Stauffer, D.; Puletti, P. Google Patents, 1993.
- McBride, W. D.; Catherine, G.; Linda F.; Ali, M. *The U.S. Department of Agriculture (USDA)*, **2015**, 188.

DOI: <http://dx.doi.org/10.32571/ijct.478179>

ISSN:2602-277X

13. Ritz, J.; Fuchs, H.; Kieczka, H.; Moran, W. C. *Ullmann's Ency. Ind. Chem.* 2000.
14. Talukdar, J.; Wong, E. H. S.; Mathur, V. K. *Sol. Energy* **1991**, 47, 165-171.
15. Zeng, Z.; Zhou, R. Google Patents, 2014.
16. Kyle, A. A.; Dahl, M. V. *Am. J. Clin. Dermatol.* **2004**, 5, 443-451.
17. Akhtar, N.; Verma, A.; Pathak, K. *Curr. Pharm. Design.* **2015**, 21, 2892-2913.
18. Amborabé, B.-E.; Fleurat-Lessard, P.; Chollet, J.-F.; Roblin, G. *Plant. Physiol. Biochem.* **2002**, 40, 1051-1060.
19. Benchea, A. C.; G Marius; Dorohoi, D. O. *Construcții de Mașini.* **2016**, 62, 41-50.
20. Waterman, M. S. *Introduction to computational biology: maps, sequences and genomes*, C. R. C. Press, 1995.
21. Dwyer, M. A.; Looger, L. L.; Hellinga, H. W. *Science* **2004**, 304, 1967-1971.
22. Yap, C. W. *J. Comput. Chem.* **2011**, 32, 1466-1474
23. Gramatica, P.; Papa, E. *QSAR & Combinatorial Science* **2003**, 22, 374-385.
24. Xia, B.; Ma, W.; Zheng, B.; Zhang, X.; Fan, B. *Eur. J. Med. Chem.* **2008**, 43, 1489-1498.
25. Raies, A. B.; Bajic, V. B. *WIREs: Comput. Mol. Sci.* **2016**, 6, 147-172.
26. Shahpar, M.; Esmaeilpoor, S. *Asian J. Green Chem.* **2017**, 2, 116-129.
27. Smith, D. M.; Mitchell, J. *Analyt. Chem.* **1950**, 22(6), 750-755.
28. Kaufman, L.; Cohen, M. *Prog. Met. Phys.* **1958**, 7, 165-246.
29. Shapiro, A. H. *The dynamics and thermodynamics of compressible fluid flow*. Vol.1, Wiley, New York, 1953.
30. Guggenheim, E. A. *Thermodynamics- An advanced treatment for chemists and physicsists*. Amsterdam, North-Holland, p.414, 1985.
31. Von Bertalanffy, L. *Science* **1950**, 111, 23-29.
32. Frank, H. S.; Evans, M. W. *J. Chem. Phys.*, **1945**, 13, 507-532.
33. Bartlett, R. J.; Musiał, M. *Rev. Mod. Phys.* **2007**, 79, 291.
34. McIver Jr, J. W.; Komornicki, A. *Chem. Phys. Lett.* **1971**, 10, 303-306.
35. Yang, W.; Ayers, P. W. In *Computational Medicinal Chemistry for Drug Discovery*; CRC Press, pp. 103-132. 2003.
36. Froimowitz, M. *Biotechniques* **1993**, 14(6), 1010-1013.
37. Evans, D. A.; Mitch, C. H.; Thomas, R. C.; Zimmerman, D. M.; Robey, R. L. *J. Am. Chem. Soc.* **1980**, 102(18), 5955-5956.
38. Howard, A.; McIver, J.; Collins, J. *HyperChem Computational Chemistry*. Hypercube Inc. Waterloo. 1994.
39. Ayala, P. Y.; Scuseria, G. E., *J. Chem. Phys.* **1999**, 110, 3660-3671.
40. Muthu, S.; Maheswari, J. U. *Spectrochim. Acta A: Mol. Biomol. Spect.* **2012**, 92, 154-163.
41. Timofeeva, L.; Kleshcheva, N. *Appl. Microbiol. Biot.* **2011**, 89, 475-492.
42. Böhm, M.; Stürzebecher, J.; Klebe, G. *J. Med. Chem.* **1999**, 42, 458-477.

ORCID

 <https://orcid.org/0000-0001-5136-6166> (A. Kumar) <https://orcid.org/0000-0003-2760-0113> (Md N. Sarker) <https://orcid.org/0000-0001-7739-4018> (S. Paul)



A study on leaching kinetics of chalcopyrite in $KNO_3 + H_2SO_4$ medium

Harun DİKME, Soner KUŞLU*, Özlem KARAGÖZ

on the last page

Department of Chemical Engineering, Faculty of Engineering, Atatürk University, 25240, Erzurum, Turkey

Received: 21 January 2019; Revised: 15 April 2019; Accepted: 20 April 2019

*Corresponding author e-mail: ksoner90@hotmail.com

Citation: Dikme, H.; Kuşlu, S.; Karagöz, Ö. *Int. J. Chem. Technol.* 2019, 3 (1), 38-45.

ABSTRACT

This paper describes the leaching behaviour and dissolution kinetics of chalcopyrite with potassium nitrate in sulphuric acid solutions. Reaction temperature, solid/liquid ratio, stirring speed, chalcopyrite particle size, concentration of sulphuric acid and concentration of potassium nitrate solutions were selected as process parameters. The experimental results were successfully correlated with linear regression using the Statistical package program and dissolution curves were evaluated by the shrinking core models for solid-fluid systems. Finally, it was found that increasing reaction temperature and decreasing solid/liquid ratio caused an increase in the dissolution rate of chalcopyrite. The dissolution extent slightly increased with the increase in the stirring speed rate between 300-900 rpm under the experimental conditions. The activation energy was found as $78.25 \text{ kJ mol}^{-1}$. It was seen that the leaching of chalcopyrite was controlled by surface chemical reactions.

Keywords: Chalcopyrite, KNO_3 , leaching kinetics, shrinking core model.

1. INTRODUCTION

One of the most common minerals in the nature is the compound of sulphur including iron and copper, called chalcopyrite (expressed as $CuFeS_2$ or $Cu_2S.Fe_2S_3$). The use of copper in human history is based on ancient times. Nowadays, even though different metals are used instead of copper in some areas, copper has always kept its importance thanks to its unique properties. High electrical and thermal conductivity, resistance to corrosion and easy processability are some of the important features of copper.

Copper production in the world is carried out by extraction, enrichment and evaluation of copper ores with sulfur and oxides. In general, about 80% of copper

Kalkopiritin $KNO_3 + H_2SO_4$ ortamındaki liçing kinetiği üzerine bir çalışma

ÖZ

Bu makale kalkopiritin sülfürik asit çözeltilerinde potasyum nitrat ile liçing davranışını ve çözünme kinetiğini açıklanmaktadır. Reaksiyon sıcaklığı, katı/sıvı oranı, karıştırma hızı, kalkopirit partikül büyüklüğü, sülfürik asit konsantrasyonu ve potasyum nitrat çözelti konsantrasyonları proses parametreleri olarak seçildi. Deneysel sonuçları, istatistiksel paket programı kullanılarak lineer regresyon ile başarılı bir şekilde ilişkilendirildi ve çözünme eğrileri, katı-akışkan sistemler için büzüşen çekirdek modelleri ile değerlendirildi. Son olarak, artan reaksiyon sıcaklığının ve azalan katı/sıvı oranının, kalkopiritin çözünme hızında bir artışa neden olduğu bulunmuştur. Çözünme derecesi, deneysel koşullarda 300-900 rpm arasındaki karıştırma hızındaki artışla biraz artmıştır. Aktivasyon enerjisi $78.25 \text{ kJ mol}^{-1}$ olarak bulunmuştur. Kalkopiritin liçinginin, yüzey kimyasal reaksiyonlarıyla kontrol edildiği görülmüştür.

Anahtar Kelimeler: Kalkopirit, KNO_3 , liçing kinetiği, büzülen nüve modeli.

production is carried out by pyrometallurgical methods, and hydrometallurgical methods are used at about 20%. Due to the environmental impact, the hydrometallurgical process is becoming an increasing importance. The hydrometallurgical process provides an effective method for processing low-grade ores.¹ The fact that the oxidized sources are preferred more over time, the required chemical materials are with easy and cheap prices, the production facilities can be easily installed where the ore is located, and the low pre-investments and the relatively less damage to the environment increase the popularity of the hydrometallurgical method. For this reason, hydrometallurgical processes are preferred generally for copper extraction. One of the most common minerals in the nature is the compound of sulphur including iron

DOI: <http://dx.doi.org/10.32571/ijct.515611>

E-ISSN:2602-277X

and copper, which is called chalcopyrite (expressed as CuFeS_2 or $\text{Cu}_2\text{S}\cdot\text{Fe}_2\text{S}_3$). Other than the ore veins, it also occurs typically in low copper concentrates. It is a highly refractory material during the hydrometallurgical process.²

Several researchers have reported chalcopyrite leaching. The leaching of chalcopyrite using different leaching solutions has been studied by some investigators (Table 1).

Table 1. Some of the studies aimed at leaching of chalcopyrite in different environments examined by various researchers

Environment	Activation energy (kJ mol^{-1})	Controlling step	Ref.
Water saturated with chlorine	9.06	Controlled by diffusion through the product layer	21
Potassium dichromate	48-54	Chemically controlled	22
By hydrogen peroxide in sulphuric acid	60	The surface reaction controlled	23
In hypochlorite	19.88	By diffusion through the product layer	24
Ferric chloride	68	Chemical reaction	25
Sodium nitrate in sulphuric acid	83	Mixed control	26
Sodium chlorate in hydrochloric acid	60.0 at 298-318 K 57.7 at 318-338 K	By chemical reaction	27

In the hydrometallurgical process, inorganic acids are used as leaching accents.³ This study aims to investigate the kinetic results for leaching and dissolution processes of chalcopyrite with KNO_3 in H_2SO_4 using a mechanical agitation system. The reaction rates for chalcopyrite are very critical for commercial initiatives. Heterogeneous reaction models were used in the analysis of kinetics for dissolution. In the study, reaction temperature, solid/liquid ratio, stirring speed, chalcopyrite particle size, concentration of sulphuric acid and concentrations of potassium nitrate solutions are used as evaluation criteria for leaching process.

2. MATERIALS AND METHODS

2.1. Materials

The chalcopyrite samples obtained from Artvin Murgul Copper Company were first disintegrated. It was then dried under a vacuum and separated into particle sizes using ASTM standard sieves to give fractions of

average dimensions of sizes -50+70, -70+100, -100+120 and -120+140 μm . The chemical analysis of the samples can be seen in Table 2.

Table 2. Chemical analysis of chalcopyrite minerals.

Component	%
Cu	6.70
Ni	0.10
Zn	0.20
SiO_2	45.60
MgO	1.32
CaO	0.28
Fe	18.45
S	19.25
Au	-
Ag	0.0213

2.2. Methods

Atmospheric weather conditions were used to perform the leaching experiments. In the experiments, 500 mL volume glass reactor was used. A constant temperature water circulation device was used to prevent the temperature change during the experiment. A backflow concentrator was used to prevent evaporation. A mechanical mixer was used to obtain a homogenous mixture. The mechanical agitation test system is quite common and it can be seen in Figure 1. Chemical analysis of chalcopyrite with a particle size of -120 + 140 mesh was performed. Each analysis was repeated twice and the mean values were used in kinetic calculations. The EDS graph of the original mineral is given in Figure 2. Cu, Ni, Au, Ag, Fe and Zn analyses were performed using atomic absorption spectrophotometry (Shimadzu AAS-670). SiO_2 and S analyses were done by gravimetric methods. MgO and CaO analyses were completed with complexometric methods with EDTA.

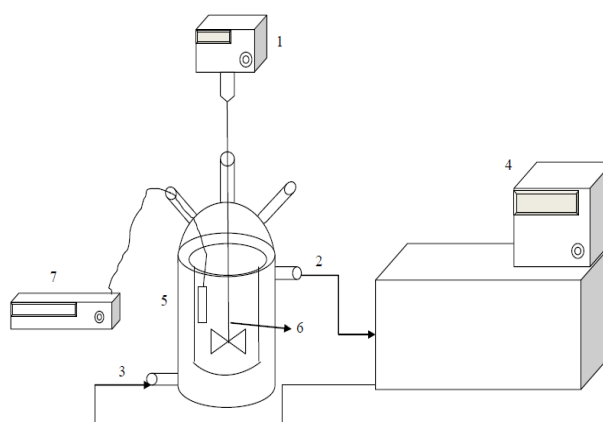


Figure 1. Mechanical Agitation Experimental System. (1. Mechanical agitator, 2. Water output, 3. Water input, 4. Water circulator heater, 5. Glass reactor, 6. stirrer, 7. pH meter).

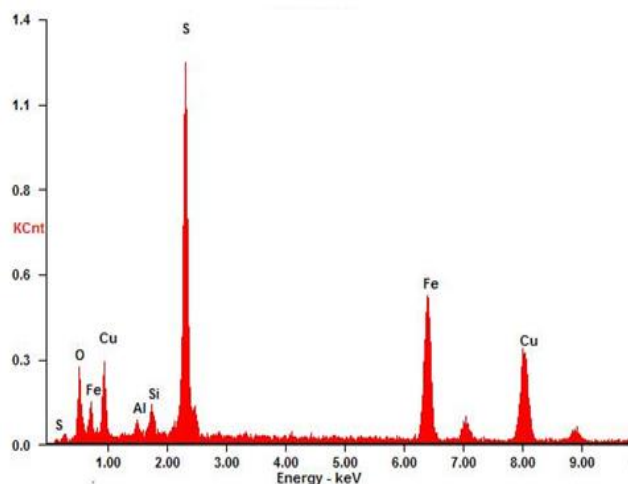


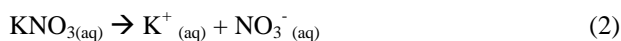
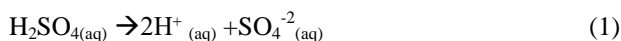
Figure 2. EDS graph of the sample.

3. RESULTS AND DISCUSSION

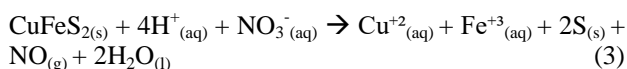
3.1. Dissolution reactions

Reactions occurring in the reactor can be given as follows.⁴⁻⁵

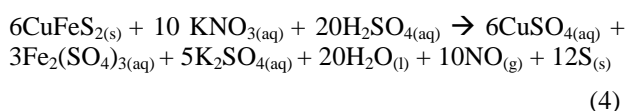
When KNO_3 was used with H_2SO_4 , the following reactions occur.



When chalcopyrite is added to the potassium nitrate solution in the reactor, the reaction can be written as follows:



The total reaction is as follows:



3.2. Effects of parameters

Reaction temperature, solid/liquid ratio, stirring speed, the particle size of chalcopyrite, the concentration of sulphuric acid and the concentration of potassium nitrate solutions were selected as process parameters to measure the effect of chalcopyrite on the dissolution level. Parameter ranges are given in Table 3.

In the experiments, the values of the other parameters were kept constant while the effect of a parameter was examined (see Table 3).

Table 3. Selected parameters and their ranges

Parameter	Values
Temperature (K)	343, 348, 353*, 358
Solid/liquid (g cm^{-3})	1/100*, 1/50, 1/25, 1/10
Stirring speed (rpm)	300, 500*, 700, 900
Particle size (μm)	256, 181, 137.5*, 115.5
Concentration of H_2SO_4 (mol dm^{-3})	2.0*, 3.0, 4.0, 5.0
Concentration of KNO_3 (mol dm^{-3})	1.0, 2.0, 3.0*, 4.0

250 mL of KNO_3 solution was used for any trial in the study. The stirrer had a constant velocity of 500 rpm to produce homogeneous concentrations in the batch reactor. Change graphs between time (t) and conversion values (X) are plotted for each parameter. These change graphs can be seen in Figure 3-8.

A 250 mL solution of potassium nitrate was used for all the experiments. The uniformity of the suspension was obtained at a stirring speed of 500 rpm. Therefore, the mixing speed of 500 rpm was a constant value in all experiments to ensure uniformity in the reactor. The plots of time (t) against conversion (X) were obtained.

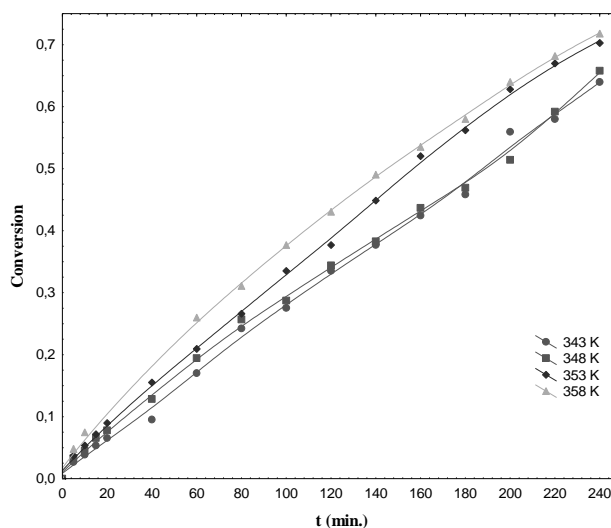


Figure 3. Change graph between time and conversion for different temperatures.

3.2.1. Effect of reaction temperature

There is a significant relationship between the reaction temperature and the speed of the leaching reaction. The experiments were performed at four different temperatures of 343, 348, 353 and 358 K. The curves were plotted as presented in Figure 3.

It is seen that the dissolution at higher temperatures is more effective in removing a greater amount of chalcopyrite.⁶ The quick production of activation energy helps to accelerate the reaction by heating the chemical reactants further only.

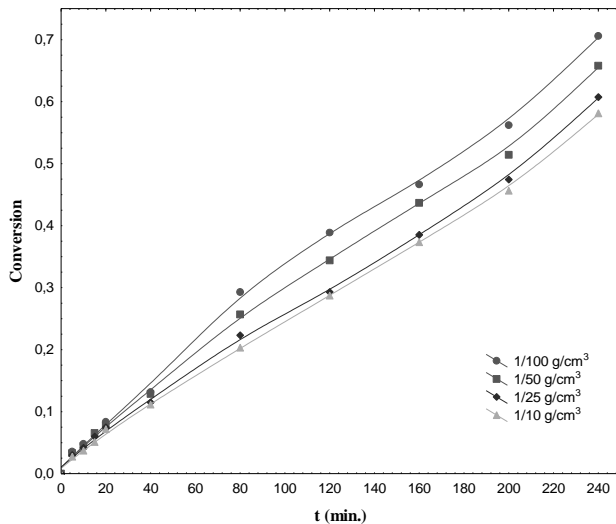


Figure 4. Change graph between time and conversion for different solid-liquid ratios.

3.2.2. Effect of S/L ratio

Changes in the solid / liquid (S / L) ratio allow the observation of the dissolution kinetics of chalcopyrite, such as 1/100, 1/50, 1/25 and 1/10 g cm⁻³, respectively. The dissolution curves are demonstrated in Figure 4. As shown in Figure 4, the dissolution rate changes in reverse with the S / L ratio. The decrease in dissolution rate with increasing solids can be explained by the decrease in the number of chalcopyrite particles per the amount of solution. If the reaction mixture has high solid-to-liquid ratio, the slurry becomes viscous and hampers ion mobility, hence decreasing the leaching efficiency.⁷

3.2.3. Effect of stirring speed

As can be seen from the reactions 3 and 4, the leaching of chalcopyrite is a heterogeneous reaction. This involves mass transfer of the reactants on the chalcopyrite surface.⁸ The effect of the stirring speed on the dissolution rate of chalcopyrite was investigated at 300, 500, 700 and 900 rpm. The change between stirring speed and conversion are shown in Figure 5. It can be seen from Figure 5 that the effect of stirring speed is very small.⁹

3.2.4. Effect of particle size

After fragmentation, four fractions such as -50 + 70, -70 + 100, -100 + 120, and -120 + 140 μm were elimina-

ted. According to the dissolution curves presented in Figure 6, a direct correlation formed between the magnitude of mineral particles and the dissolution rate because the smaller parts have more surface area and less volume.

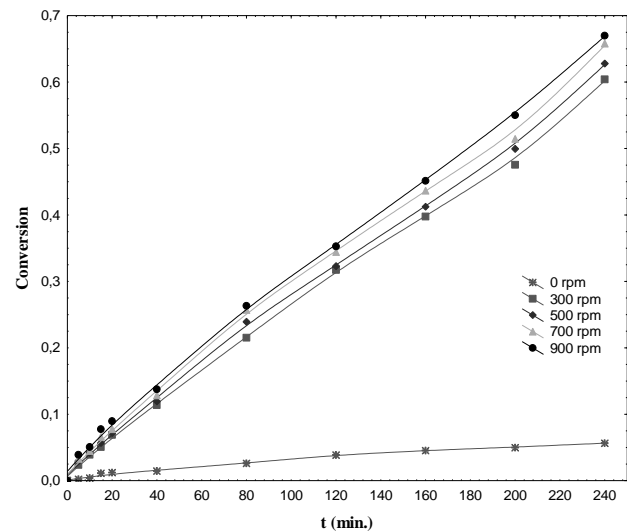


Figure 5. Change graph between time and conversion for different stirring speeds.

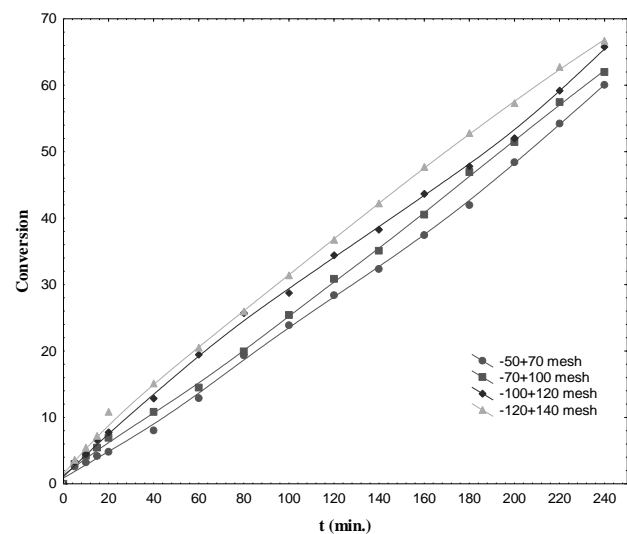


Figure 6. Change graph between time and conversion for different particle sizes.

The high ratio of surface area to volume means that the leaching has more opportunity to contact with the mineral.¹⁰

3.2.5. Effect of H₂SO₄ concentration

In this study, the reagent for the leaching reaction was sulphuric acid. The H₂SO₄ concentration needs to be raised up to a specific value and not beyond that for leac-

hing efficiency. In response to variations of 2.0, 3.0, 4.0 and 5.0 mol dm⁻³, dissolution curves were plotted. The graph can be seen in Figure 7. It was determined that the level of dissolution of the process increased with the increase in the concentration of the sulfuric acid solution. The efficient dissolution reaction is associated with higher H₂SO₄ concentrations.¹¹

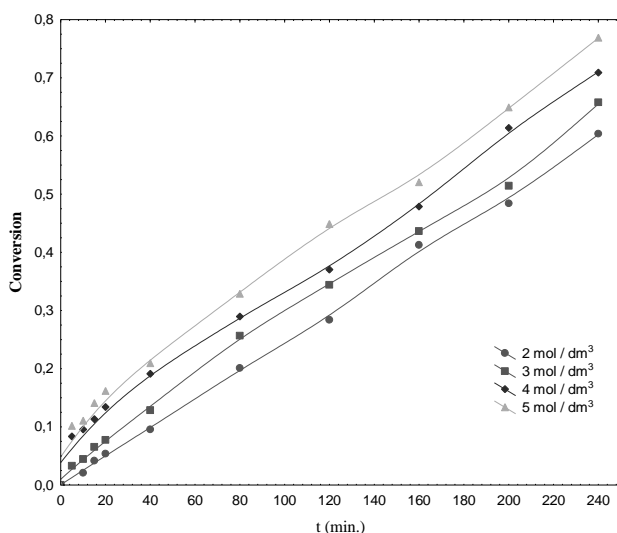


Figure 7. Change graph between time and conversion for different concentrations of H₂SO₄.

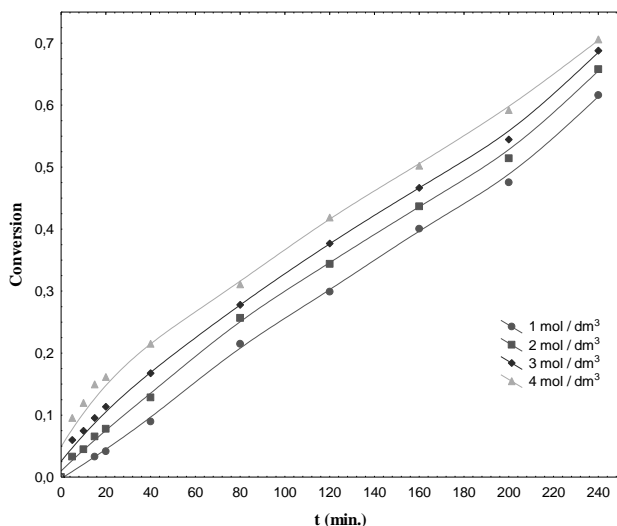


Figure 8. Change graph between time and conversion for different concentration of KNO₃.

3.2.6. Effect of KNO₃ concentration

Potassium nitrate is both a crystalline salt and a strong oxidizer, and it is used especially in gunpowder, fertilizer and medicine. The effect of the KNO₃ concentration on the leaching grade was determined at a KNO₃ concentration between 1.0 and 4.0 mol dm⁻³ and at a time interval of 3 to 240 minutes. The dissolution curves are given in Figure 8. From Figure 8, the level of

dissolution of the process increases with an increase in the concentration of potassium nitrate solution.²¹ Because of the fact that sulphuric acid without oxidants does not react with chalcopryrite, the reaction rate increases with an increase in KNO₃ concentration. The oxidation potential of nitrate ions increases the acidity of the solution. Therefore, this situation increases the leaching rate.³

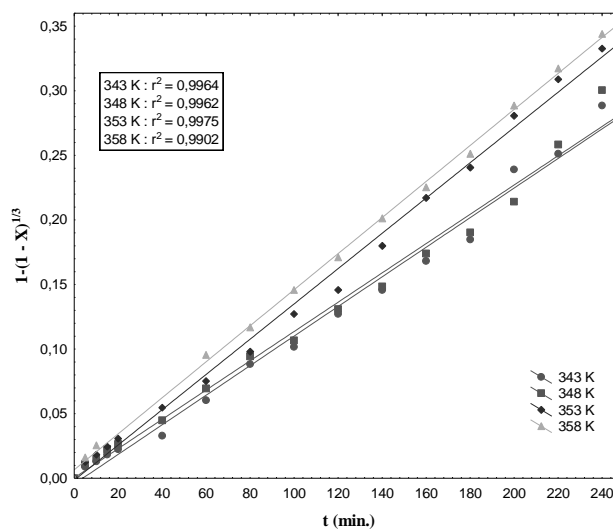


Figure 9. Change between $1-(1-X)^{1/3}$ and t for different reaction temperature.

3.2.7. Kinetics analysis

In order to determine the kinetic parameters and the reaction rate control step of the dissolution reaction between chalcopryrite mineral and sulphuric acid with potassium nitrate solutions, non-catalytic heterogeneous reaction models were applied on experimental data.¹² Heterogeneous reaction model can be used to study the heterogeneous reaction process between solid and liquid. The non-reacting shrinking core model was applied to analyse the trial results and to make an assessment of the speed-limiting step.¹³ Rate equations can be obtained from the heterogeneous reaction model, especially for each control mechanism. The heterogeneous reaction model is numerically and analytically used for solid-liquid heterogeneous systems. The integral ratio equations for the non-reacted shrink core model and other models are presented in Table 4. Following the experiments, the analysis of the results was performed as best practice using the above-mentioned models to evaluate the kinetics of the leaching process. When the film diffusion is much quicker than the chemical reaction, the leaching action refers to the controlled chemical reaction. Also, the regression coefficients of models calculated in the study can be reviewed in Table 4. As a result of the regression analysis, the results of the experiment were found to be in accordance with Eq. (6) in Table 4. Therefore, it can be said that this reaction is controlled by chemical reaction. Starting from this, the leaching process is limited by the chemical reaction. The

Table 4. Integral rate equations for non-reactive shrink core model and other models

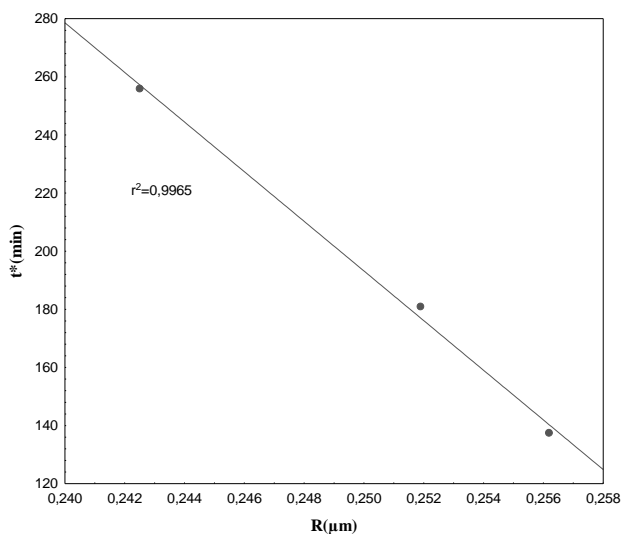
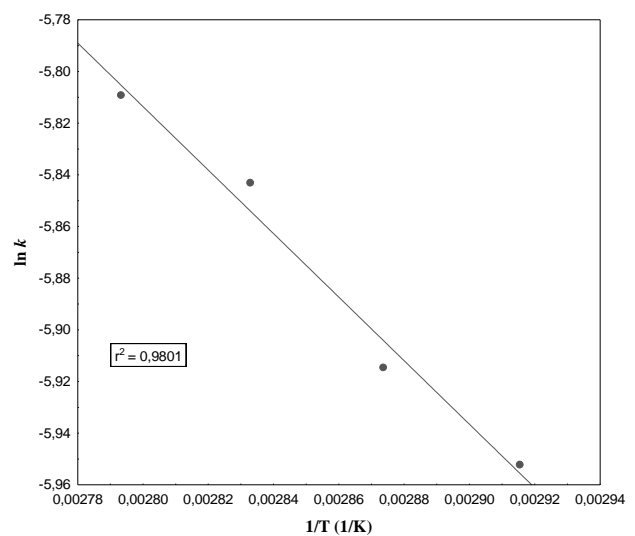
Rate-controlling step	Rate equation	r^2	Equation
Chemical reaction	$t/t^* = [1 - (1 - X_B)^{1/3}]$ $t^* = \rho_B R / bksC_{Ag}$	0.998	(5)
Film diffusion control	$t/t^* = X_B$ $t^* = \rho_B R / 3bkC_{Ag}$	0.961	(6)
Diffusion control through the ash or product layer	$t/t^* = [1 - 3(1 - X_B)^{2/3} + 2(1 - X_B)]$ $t^* = \rho_B R^2 / 6bDeC_{Ag}$	0.941	(7)
First-order pseudo-homogeneous model	$-\ln(1-X) = kt$	0.925	(8)
Second-order pseudo-homogeneous model	$(1-X)^{-1} = kt$	0.912	(9)
Avrami model	$-\ln(1-X) = kt^m$	0.933	(10)

t^* : Reactionary time for full conversion, min.

regression coefficient of the model was calculated as 0.998. This is a fairly high value. For different reaction temperatures, a graph between time and $1 - (1-X)^{1/3}$ can be seen in Figure 9.

In reactions controlled by the chemical reaction, reactionary time for full conversion (t^*) is proportional to the starting radius of a solid particle (R).¹⁴⁻¹⁸ The t^* values versus R were plotted. The high linearity between t^* and R can be seen in Figure 10. The regression coefficient (r^2) between t^* and R was found to be 0.9965. In diffusion controlled reaction, reactionary time for full conversion (t^*) is proportional to square of the starting radius of a solid particle (R^2). The regression coefficient (r^2) between t^* and R^2 was determined to be 0.9566. This situation confirms that rate controlling step for this process is governed by the chemical reaction model. The value of the activation energy helps to estimate the speed

control step. In order to find the activation energy of the reaction, Arrhenius graphs between $\ln k$ and $1/T$ must be plotted. For this reason, the obtained graph can be seen in Figure 11. The correlation coefficient of this graph is 0.9801. The slopes of the straight line give the activation energy of the reaction. The activation energy was found to be 78.25 kJ mol⁻¹. The temperature dependence of diffusion controlled processes is low. The temperature dependence of chemical reaction controlled processes is very high. In diffusion controlled processes, the activation energy varies between about 4 and 12 kJ mol⁻¹.¹² The activation energy of the leaching process controlled by the surface chemical reactions was observed to be more than 40 kJ mol⁻¹.¹⁹ There is matching evidence in literature.^{13,20} Furthermore, this energy level confirms that the dissolution rate for chalcopyrite is measured under the control of a chemical reaction.

**Figure 10.** Linearity change between t^* and R.**Figure 11.** Arrhenius graph.

4. CONCLUSIONS

The dissolution kinetics of chalcopyrite with potassium nitrate in sulphuric acid solutions with the help of a mechanical agitation system was investigated in the work. As process parameters, temperature, S/L ratio, stirring speed, particle size, concentration of sulphuric acid and potassium nitrate solutions were selected.

As a result of the study, it may be concluded that:

- Rate controlling step for this process is the chemical reaction model.
- The activation energy was found to be 78.25 kJ mol⁻¹.
- The higher reaction temperature and smaller S/L ratio has a slight effect on dissolution rate.
- The oxidation potential of nitrate ions increases the acidity of the solution.
- KNO₃ in H₂SO₄ solution can be used for the dissolution of chalcopyrite.

Nomenclature

b	Stoichiometric coefficient
C	Concentration of KNO ₃ solution, mol m ⁻³
C _{Ag}	Concentration of a in the bulk solution, mol m ⁻³
D	Mean particle size, m
D _e	Diffusion coefficient, m ² min ⁻¹
E _A	Activation energy, J mol ⁻¹
k _d	Mass transfer coefficient, m min ⁻¹
k _s	Reaction rate constant for surface reaction, mol min ⁻¹
k _o	Frequency or pre-exponential factor, min. ⁻¹
L	Amount of liquid, dm ³
n	Mol number, mol
r	Correlation coefficient
R	Universal gas constant, J mol ⁻¹ K ⁻¹
R	Initial radius of a particulate solid, m
S	Amount of solid, g
T	Reaction temperature, K
t	Reactionary time, min.
t*	Reactionary time for full conversion, min.
X	Fractional conversion of chalcopyrite
W	Stirring speed, rpm
ρ _B	Molar density of solid reactant, mol m ⁻³

Conflict of interests

Authors declare that there is no a conflict of interest with any person, institute, company, etc.

REFERENCES

1. Dimitrijevic, M.; Antonijevic, M.; Jankovic, Z., *Hydrometallurgy* **1996**, 42 (3), 377-386.

2. Dutrizac, J. E., *Metall. Trans. B* **1978**, 9 (3), 431-439.

3. Vračar, R. Ž.; Vučković, N.; Kamberović, Ž., *Hydrometallurgy* **2003**, 70 (1-3), 143-151.

4. Nemodruk, A. A.; Karalova, Z. K., *Analytical Chemistry of Boron*, Israel Program for Scientific Translations, 1965.

5. Sookg, D.; West, D.; Holler, F., *Saunders College Publishing* **1996**.

6. Naderi, H.; Abdollahy, M.; Mostoufi, N.; Koleini, M.; Shojaosadati, S.; Manafi, Z., *Int. J. Min. Met. Mater.* **2011**, 18 (6), 638-645.

7. Panda, L.; Rao, D.; Mishra, B.; Das, B., *Miner. Metall. Proc.* **2014**, 31 (1), 57-65.

8. Papangelakis, V.; Demopoulos, G., *Hydrometallurgy* **1991**, 26 (3), 309-325.

9. Kurtbas, A.; Kocakerim, M. M.; Küçük, Ö.; Yartasi, A., *Ind. Eng. Chem. Res.* **2006**, 45 (6), 1857-1862.

10. Levenspiel, O., *Wiley-Eastern Limited, New York* **1972**.

11. Aydogan, S.; Ucar, G.; Canbazoglu, M., *Hydrometallurgy* **2006**, 81 (1), 45-51.

12. Demirkiran, N., *Hydrometallurgy* **2009**, 95 (3-4), 198-202.

13. Alkan, M.; Doğan, M.; Namli, H., *Ind. Eng. Chem. Res.* **2004**, 43 (7), 1591-1598.

14. Habashi, F., *Kinetics of metallurgical processes*. 1999.

15. Dönmez, B.; Demir, F.; Laçın, O., *J. Ind. Eng. Chem.* **2009**, 15 (6), 865-869.

16. Kuşlu, S.; Dişli, F. Ç.; Çolak, J. *Ind. Eng. Chem.* **2010**, 16 (5), 673-678.

17. Guliyev, R.; Kuşlu, S.; Çalban, T.; Çolak, S., *J. Ind. Eng. Chem.* **2012**, 18 (4), 1202-1207.

18. Guliyev, R.; Kuşlu, S.; Çalban, T.; Çolak, S., *J. Ind. Eng. Chem.* **2012**, 18 (1), 38-44.

19. Jackson, E., *Hydrometallurgical extraction and reclamation*. Chichester: Horwood; New York, Wiley: 1986.

20. Yartasi, A.; Ozmetin, C.; Kocakerim, M.; Demirhan, M., *Chim. Acta TUR.* **1998**, 26 (2), 7-14.

DOI: <http://dx.doi.org/10.32571/ijct.515611>

E-ISSN:2602-277X

21. Çolak, S.; Alkan, M.; Kocakerim, M. M., *Hydrometallurgy* **1987**, 18 (2), 183-193.
22. Antonijević, M.; Janković, Z.; Dimitrijević, M., *Hydrometallurgy* **1994**, 35 (2), 187-201.
23. Antonijević, M.; Janković, Z.; Dimitrijević, M., *Hydrometallurgy* **2004**, 71 (3), 329-334.
24. Ikiz, D.; Gülfen, M.; Aydın, A., *Minerals engineering* **2006**, 19 (9), 972-974.
25. Al-Harashsheh, M.; Kingman, S.; Al-Harashsheh, A., *Hydrometallurgy* **2008**, 91 (1), 89-97.
26. Sokić, M. D.; Marković, B.; Živković, D., *Hydrometallurgy* **2009**, 95 (3), 273-279.
27. Xian, Y.; Wen, S.; Deng, J.; Liu, J.; Nie, Q., *Can. Metall. Quart.* **2012**, 51 (2), 133-140.

ORCID

 <https://orcid.org/0000-0001-6302-5107> (H. Dikme)

 <https://orcid.org/0000-0003-4830-5949> (S. Kuşlu)

 <https://orcid.org/0000-0003-0431-1861> (Ö. Karagöz)



Synthesis of tetrakis (4-(2-phenylprop-2-yl) phenoxy) substituted phthalocyanines using a new practical method

Mehmet Salih AĞIRTAŞ*, Cihan DURMUŞ, Beyza CABİR

on the last page

Department of Chemistry, Faculty of Science, Van Yüzüncü Yıl University, 65080, Van, Turkey

Received: 23 March 2019; Revised: 05 May 2019; Accepted: 15 May 2019

*Corresponding author e-mail: salihagirtas@hotmail.com

Citation: Ağırtaş, S. M.; Durmuş, C.; Cabir, B. *Int. J. Chem. Technol.* 2019, 3 (1), 46-51.

ABSTRACT

In this study, zinc, cobalt and nickel phthalocyanine compounds bearing the 4-(2-phenylprop-2-yl)phenoxy substituent were prepared. Here, a new practical method for synthesis was used. This method significantly shortens the synthesis time. This method is very effective for the reaction to take place in a short time and at a lower temperature. Additionally, these compounds were examined for their aggregation and photodegradation properties. The aggregation was studied in concentration range of 1×10^{-5} - 1×10^{-6} M in tetrahydrofuran (THF). The photodegradation properties of phthalocyanine complexes under light irradiation were also investigated in chloroform (CHCl_3).

Keywords: Phthalocyanine, synthesis, method, aggregation.

Yeni pratik bir yöntem kullanarak tetrakis (4-(2-fenilprop-2-il) fenoksi) süstitüentli ftalosiyanınların sentezi

ÖZ

Bu çalışmada, 4- (2-fenilprop-2-il) fenoksi süstitüentini taşıyan çinko, kobalt ve nikel ftalosiyanın bileşikleri hazırlandı. Burada sentez için yeni pratik bir metot kullanıldı. Bu metot sentez süresini oldukça kısaltmaktadır. Bu yöntem, reaksiyonun kısa sürede ve daha düşük bir sıcaklıkta gerçekleşmesi için çok etkilidir. Ayrıca, bu bileşikler agregasyon ve fotoregradasyon özellikleri açısından incelenmiştir. Agregasyon tetrahydrofuran (THF) içinde 1×10^{-5} - 1×10^{-6} M konsantrasyon aralığında incelenmiştir. Işık ışınımı altında ftalosiyanın komplekslerinin fotodegradasyon özellikleri de kloroformda (CHCl_3) incelenmiştir.

Anahtar Kelimeler: Phthalocyanine, sentez, yöntem, agregasyon.

1. INTRODUCTION

Phthalocyanines have become an attractive topic for researchers because they find applications such as photodynamic therapy,¹⁻² solar cells,³ catalysts,⁴ dyes,⁵⁻⁶ photocatalysts,⁷ gas sensor⁸, semiconductor materials.⁹ It is known that one of the reasons preventing the widespread use of phthalocyanines in technological areas is aggregation.¹⁰ The synthesis of non-aggregation phthalocyanines have been important for applications. This problem can be solved by attaching appropriate substituents at the peripheral positions of the phthalocyanine core.¹¹⁻¹² Metal phthalocyanines have some advantages for use in both catalyst and other applications. It is the reason for preference in terms of

thermal stability and preparation technique.¹³ These compounds are extremely stable in the chemical direction. This allows them to be used in many reaction environments.¹⁴ The use of phthalocyanine complex as a catalyst in fuel cells has increased interest in these compounds.¹⁵⁻¹⁶ As is known, the catalysts can be used not only in fuel cells but also in the deferring of many reactions and industrial wastes. Phthalocyanine compounds have a photocatalytic effect and can be applied to the breakdown of some organic waste dyes.¹⁷ Phthalocyanine compounds can contribute to the key role in solving these problems. Phthalocyanines have a high photocatalytic performance potential compared to other photocatalytic materials.¹⁸⁻¹⁹

In this study, 4-(2-phenylprop-2-yl) phenoxy) phthalonitrile, which is the starting material, was synthesized for the mentioned phthalocyanine compounds. Zinc, cobalt and nickel phthalocyanine compounds were synthesized by using a more effective new method than conventional and the microwave method. Aggregation and solubility properties were investigated. The photodegradation preliminary studies were tested.

2. EXPERIMENTAL

2.1. General

ZnCl₂, CoCl₂, NiCl₂, K₂CO₃, ethanol, methanol, 4-cumylphenol, acetone, tetrahydrofuran (THF), dichloromethane (CH₂Cl₂), dichloroethane, dimethyl formamide (DMF) were purchased from Merck and Sigma. The solvents were purified according to standard procedure²⁰ and stored over molecular sieves (4 Å). All reactions were carried out under dry nitrogen atmosphere. Melting points were measured on an electrothermal apparatus. Electronic spectra were recorded on a Hitachi U-2900 Spectrophotometer. Routine FT-IR spectra were recorded on a Thermo Scientific FT-IR (ATR sampling accessory) spectrophotometer. ¹H NMR spectra were recorded on a Agilent 400 MHz spectrometer with tetramethylsilane as internal standard.

2.2. 4-(4-(2-phenylprop-2-yl) phenoxy) phthalonitrile (3)

A mixture of 4-cumylphenol 1 (0.6135g, 2.89 mmol) and 4-nitrophthalonitrile 2 (0.500 g, 2.89 mmol) in 25 ml dimethylformamide was stirred at room temperature under nitrogen atmosphere. After stirring for 15 min, K₂CO₃ (2.2 g, 15.92 mmol) was added into the mixture over a period of 2 h. The reaction mixture was further stirred for 48 h at room temperature. The reaction mixture was poured into cold water (150 ml) and stirred. The jelly-like substance which was triturated with hexane. The precipitate was filtered off, washed with water to neutralize it, and dried. The product was recrystallized from ethanol. The product is soluble in diethyl ether, chloroform, acetone, dichloromethane, dichloroethane, acetonitrile, ethyl acetate, THF, DMF and DMSO. Yield; 0.5375 g (55%). Mp: 95°C. ¹H NMR (400 MHz, DMSO-d₆, δ): 8.03, 7.68, 7.30, 7.24, 7.14, 7.06, 3.62, 2.48, 1.62, 1.04. ¹³C NMR (400 MHz, DMSO-d₆, δ): 161.49, 150.31, 148.26, 136.68, 129.10, 128.56, 126.84, 126.15, 122.90, 122.23, 120.16, 117.04, 115.12, 108.39, 42.65, 40.26, 40.06, 39.85, 39.64, 39.43, 39.22, 39.01, 30.82. FT-IR spectrum (cm⁻¹): 3078, 3032, 2970, 2935 2870, 2233, 1589, 1562, 1485, 1446, 1404, 1276, 1249, 1207, 1172, 1083, 1014, 952, 898, 840, 702. Anal calculated for C₂₃H₁₈N₂O: (338.40 g mol⁻¹) C 81.63; H 5.36; N 8.28 %. Found C 81.46; H 5.30; N 8.23%.

2.3. 2(3), 9(10), 16(17), 23(24) – tetrakis (4-(2-phenylprop-2-yl) phenoxy) phthalocyaninato) zinc (II) (4)

4-(4-(2-phenylprop-2-yl) phenoxy) phthalonitrile 3 (0.100 g, 0.295 mmol) and ZnCl₂ (0.020 g) was powdered in a quartz crucible and heated in a sealed glass tube for 6 min under nitrogen at 230°C. After cooling to room temperature, the product was washed with water, ethanol and methanol. It was then purified by column chromatography on silica gel with tetrahydrofuran as the eluent. This compound is soluble acetone, tetrahydrofuran, dichloromethane, dichloroethane and dimethylformamide. Yield: 0.0392 g (37.40%). ¹H NMR (400 MHz, CDCl₃, δ): 7.74, 7.49, 7.33, 7.25, 7.23, 6.92, 6.56, 1.41. Calc. for C₉₂H₇₂N₈O₄Zn: (1418.99 g mol⁻¹) C, 77.87; H, 5.11; N, 7.90%. Found: C, 77.79; H, 5.21; N, 7.84 %. UV-Vis (THF) λ_{max} (log ε): 676 (5.30), 610 (4.72), 352 (5.04). IR spectrum (cm⁻¹):3032, 2962, 2870, 1600, 1473, 1442, 1234, 1168, 1087, 948, 744.

2.4. 2(3), 9(10), 16(17), 23(24) – tetrakis (4-(2-phenylprop-2-yl) phenoxy) phthalocyaninato) cobalt (II) (5)

4-(4-(2-phenylprop-2-yl) phenoxy) phthalonitrile 3 (0.100 g, 0.295 mmol) and CoCl₂ (0.020 g) was powdered in a quartz crucible and heated in a sealed glass tube for 6 min under nitrogen at 230°C. After cooling to room temperature, the product was washed with water, ethanol and methanol. It was then purified by column chromatography on silica gel with tetrahydrofuran as the eluent. This compound is soluble acetone, tetrahydrofuran, dichloromethane, dichloroethane and dimethylformamide. Yield: 0.015 g (14.38%). Calc. for C₉₂H₇₂ Co N₈O₄: (1412.54 g mol⁻¹) C, 78.23; H, 5.14; N, 7.93 %. Found: C, 78.15; H, 5.20; N, 7.91%. UV-Vis (THF) λ_{max} (log ε): 662 (5.25), 600 (4.73) 326 (5.15). IR spectrum (cm⁻¹): 3032, 2962, 2870, 1604, 1504, 1469, 1442, 1441, 1238, 1165, 1118, 1095, 1066, 956.

2.5. 2(3), 9(10), 16(17), 23(24) – Tetrakis (4-(2-phenylprop-2-yl) phenoxy) phthalocyaninato) nickel (II) (6)

4-(4-(2-phenylprop-2-yl) phenoxy) phthalonitrile 3 (0.100 g, 0.295 mmol) and NiCl₂ (0.020 g) was powdered in a quartz crucible and heated in a sealed glass tube for 6 min under nitrogen at 230°C. After cooling to room temperature, the product was washed with water, ethanol and methanol. It was then purified by column chromatography on silica gel with tetrahydrofuran as the eluent. This compound is soluble acetone, tetrahydrofuran, dichloromethane, dichloroethane and dimethylformamide. Yield: 0.022 g (21.15%). ¹H NMR (400 MHz, CDCl₃, δ): 7.52, 7.36,

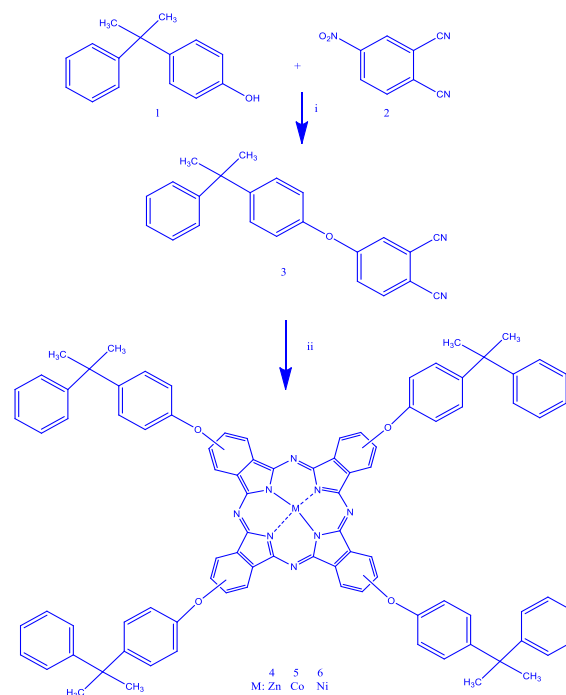
7.25, 6.98, 1.55. Calc. for $C_{92}H_{72}N_8NiO_4$: (1412.30 g mol⁻¹) C, 78.24; H, 5.14; N, 7.93%. Found: C, 78.22; H, 5.10; N, 7.88%. UV-Vis (THF) λ_{max} (log ϵ): 672 (5.27), 608 (4.80), 328 (4.97). IR spectrum (cm⁻¹): 3032, 2966, 2870, 1604, 1535, 1504, 1473, 1415, 1238, 1168, 1118, 1095, 1064, 821, 702.

3. RESULTS AND DISCUSSION

3.1. Synthesis and characterization

The synthesis route of phthalocyanine compounds prepared in this study is shown in Scheme 1. The phthalonitrile compound was obtained by reaction of 4-cumylphenol with 4-nitrophthalonitrile in basic medium. Phthalocyanine compounds were obtained by heating with corresponding metal salts. Phthalocyanine compounds were obtained in the solvent-free medium. These reactions were completed in a very short time such as 6 minute. It was synthesized more practically than the reactions in the solvent environment.²¹ This synthesis method is also advantageous from the synthesis made from the microwave oven. Because, the reaction was completed in a short time. This method facilitates the practical synthesis of phthalocyanines. These compounds obtained by the conventional method were tested for Langmuir-Blodgett monomolecular layer formation.²² In response to the reaction times of 44 to 70 hours for the preparation of phthalocyanine complexes by these conventional synthetic methods, the same compounds were synthesized in only 6 minutes with our method. The synthesis of phthalocyanine compounds, easily and economically, provides the testing opportunity of these compounds in applications such as catalyst, sensor, photocatalytic, photodynamic therapy, dyeing.

The IR spectrum gives information about the vibration bands. This spectral data does support to structure. Compound 3 yields bands 3078, 3032 (Ar-CH₃), 2970 (CH₃), 2233 (CN), 1585-1589-1562 (C=C) 1249 (Ar-O-Ar). Among these bands, the 2233 (CN) band is a peak that separates this compound from phthalocyanines. The equivalent of these functional groups (Ar-CH₃ 3082; CH₃ 2976; CN 2238; Ar-O-Ar 1255; C = C 1563) was reported.²² The data appear to be compatible. The observation in these compounds of the phthalocyanine is considered to be one of the most prominent features. This difference is very much in the literature. In these compounds, they give the appropriate vibration bands according to the literature.^{21,22} The vibration bands of the compounds prepared in this study are given in the experimental part. The ¹H and ¹³C NMR spectra of compound 3 are compatible with the literature values.²² Except for the small shifts caused by the solvent, it is suitable. While the solvent used DMSO-d₆, the previous study used CDCl₃.



Scheme 1. Synthetic pathway of compounds (3-6). Reagents and conditions: (i) DMF, K₂CO₃, 48 h, rt; (ii) ZnCl₂, CoCl₂, NiCl₂, N₂, 230°C.

In the same way, for the NMR spectra of zinc and nickel metal phthalocyanines different solvents from the literature were used. The expected results were obtained. Structural explanation is intended to demonstrate the suitability of the method. The purpose is not to discuss the spectral data. The important thing is that the same compounds are obtained in a shorter time. For example, zinc phthalocyanine was obtained in 6 minutes at 230°C with this method, but it was 70 hours at 280°C by conventional method.²² This comparison clearly demonstrates the advantage of the method.

The electronic absorption spectra of the phthalocyanine compounds obtained in this work were investigated. The absorption spectra recorded in THF give the expected B and Q bands. The electronic properties of the phthalocyanines with delocalized 18 π electron system are explained by the fact that the Q and B bands are useful for binary applications.²³ It also tells you whether there is near red and whether the compound binds to the metal. Yielding Q-bands at 676, 662, and 672 nm, giving Soret bands of a typical phthalocyanine at about 352, 326 and 328 nm for compounds of 4-6 phthalocyanine.

Phthalocyanine compounds show formation ability of H and J type aggregates in organic solvents, especially in aqueous solution, due to intermolecular π - π interactions of electrons on the phthalocyanine rings.²⁴ H type aggregation is more common in phthalocyanine compo-

unds. Q indicates a shift in the band to blue and that the monomers come face to face. The J-type is observed to be more red-shift.

The aggregation behavior are generally displayed by changes in the UV-Vis spectra of phthalocyanines, and mostly based on the analysis of the impact of concentration on absorption spectra. Phthalocyanines (4-6) were examined in THF over a wide concentration range (10^{-6} - 10^{-5} M), respectively. The working ranges of the compounds are from $2.11 \cdot 10^{-5}$ to $3.51 \cdot 10^{-6}$ M for compound 4, from $2.12 \cdot 10^{-5}$ to $3.78 \cdot 10^{-6}$ M for compound 5, from $2.12 \cdot 10^{-5}$ to $3.78 \cdot 10^{-6}$ M for compound 6, respectively. The aggregation studies of these compounds are given in Figures 1-3. When the shapes are examined, it is seen that the compounds are not aggregate in the study range. The Q band intensity was increased with increasing concentrations of phthalocyanines and no new bands were observed due to the aggregated species.

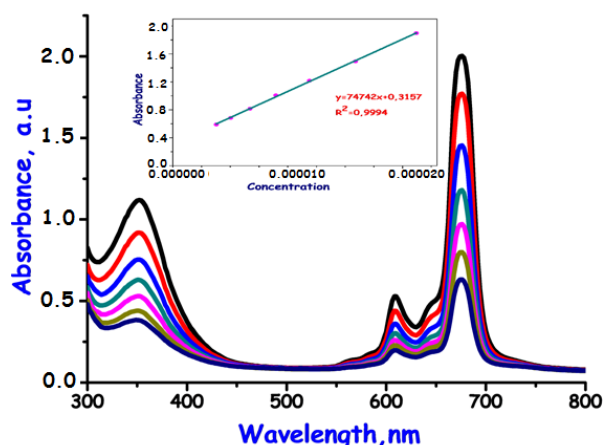


Figure 1. Aggregation study compound 4 in THF ($2.11 \cdot 10^{-5}$, $1.58 \cdot 10^{-5}$, $1.19 \cdot 10^{-5}$, $8.92 \cdot 10^{-6}$, $6.25 \cdot 10^{-6}$, $4.68 \cdot 10^{-6}$, $3.51 \cdot 10^{-6}$ M concentration range).

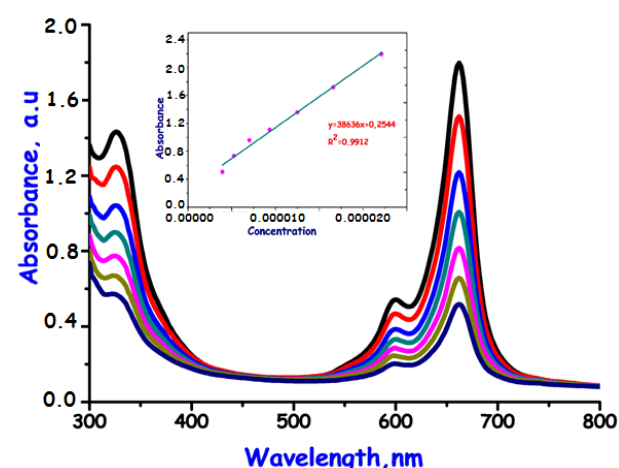


Figure 2. Aggregation study compound 5 in THF ($2.12 \cdot 10^{-5}$, $1.59 \cdot 10^{-5}$, $1.19 \cdot 10^{-5}$, $8.97 \cdot 10^{-6}$, $6.72 \cdot 10^{-6}$, $5.04 \cdot 10^{-6}$, $3.78 \cdot 10^{-6}$ M concentration range).

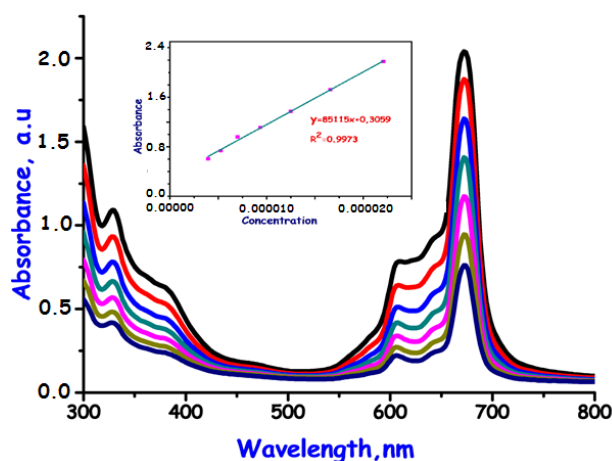


Figure 3. Aggregation study compound 6 in THF ($2.12 \cdot 10^{-5}$, $1.59 \cdot 10^{-5}$, $1.19 \cdot 10^{-5}$, $8.97 \cdot 10^{-6}$, $6.72 \cdot 10^{-6}$, $5.04 \cdot 10^{-6}$, $3.78 \cdot 10^{-6}$ M concentration range).

Looking at the applications of phthalocyanines, it seems to be important to determine the degradation by light. Because, phthalocyanine compounds can be used as paint on many surfaces. The degradation with light effect gives information about the stability and suitability of the paint. This allows compounds of phthalocyanine to be used in many applications. However, it can be a disadvantage in terms of environmental pollution. It is also advantageous in making paint and pigment which is resistant to irradiation.²⁵ Photodegradation studies of phthalocyanine complexes have been investigated as the Q absorbance band versus time. Photodegradation studies are useful for testing these properties of substances. The same method used in the previous study was used for photocatalytic testing.¹⁷ Xenon lamp (XHA-150W) water cooled photoreactor was used in this study. The photodegradation spectral changes observed by irradiation in the CHCl_3 solvent are shown in Figures 4-6. It can be said that these phthalocyanines are highly resistant to photochemical degradation. The photocatalytic degradation effect of these phthalocyanine compounds on substances such as methylene blue can be investigated as another study.

Although phthalocyanine derivatives are widely synthesized, the solubility problem is not completely exceeded.²⁶ Therefore, easy dissolving phthalocyanines are attracted by the researchers.²⁷ The method used and the solubility in a large number of solvents are important advantages. The solubility tests of the prepared phthalocyanine compounds have been found to be readily solved in organic solvents such as acetone, tetrahydrofuran, dichloromethane, dichloroethane and dimethylformamide.

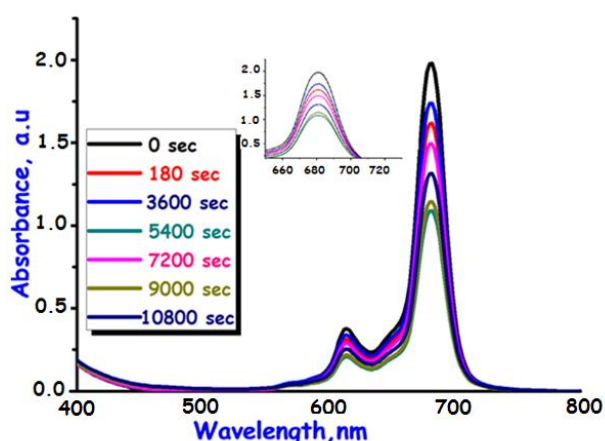


Figure 4. The photodegradation of Zinc (II) Pc (4) in CHCl_3 showing the disappearance of the Q band. Concentration = 1.0×10^{-5} M (Inset: plot of Q band absorbance vs time-sec).

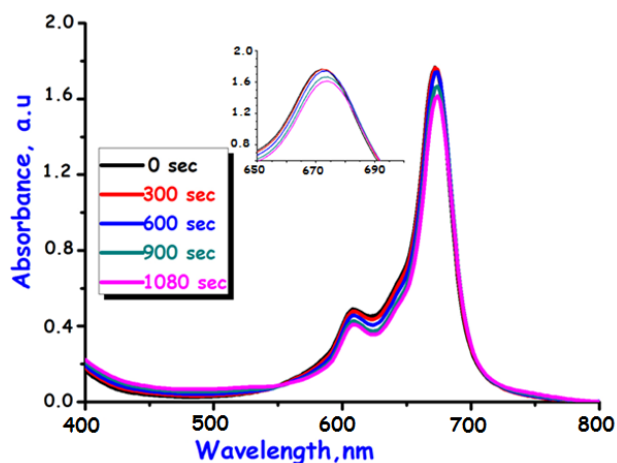


Figure 5. The photodegradation of Cobalt (II) Pc (5) in CHCl_3 showing the disappearance of the Q band. Concentration = 1.0×10^{-5} M (Inset: plot of Q band absorbance vs time-sec).

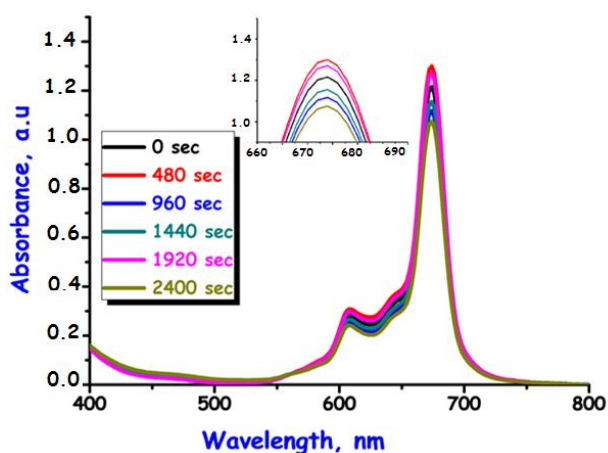


Figure 6. The photodegradation of Nickel (II) Pc (6) in CHCl_3 showing the disappearance of the Q band. Concentration = 1.0×10^{-5} M (Inset: plot of Q band absorbance vs time-sec).

4. CONCLUSIONS

In this study, metallo phthalocyanines compounds bearing (4-(2-phenylprop-2-yl) phenoxy) groups in the peripheral position were prepared by an effective method. These phthalocyanines compounds are readily soluble in solvents such as acetone, tetrahydrofuran, dichloromethane, dichloroethane, dimethyl formamide. These compounds show very good solubility compared to many phthalocyanine derivatives. The solubility simplifies the research for different application. The aggregation and photodegradation properties of the compounds were examined at certain concentrations and solvents. The compounds did not show any aggregation in the studied concentration range. This method shows that many phthalocyanine compounds can be synthesized practically. This method provides advantages such as time and temperature, not solvent usage.

ACKNOWLEDGEMENTS

This study was supported by the Research Fund of Van Yuzuncu Yıl University (FYL-2016-5160).

Conflict of interests




Authors declare that there is no a conflict of interest with any person, institute, company, etc.

REFERENCES

- Mantareva, V.; Durmus, M.; Aliosman, M.; Stoineva I.; Angelov, I. *Photodiagn. Photodyn. Ther.* **2016**, 14, 98-103.
- Duchi, S.; Ramos-Romero, S.; Dozza, B.; Guerra-Rebollo, M.; Cattini, L.; Ballestri, M.; Dambruoso, P.; Guerrini, A.; Sotgiu, G.; Varchi, G.; Lucarelli, E.; Blanco, J. *Nanomedicine.* **2016**, 12, 1885-1897.
- Sfyri, G.; Kumar, C.V.; Wang, Y.L.; Xu, Z.X.; Krontiras C.A.; Lianosa, P. *Appl. Surf. Sci.* **2016**, 360, 767-771.
- Choi, S.A.; Kim, K.; Lee, S.J.; Lee, H.; Babajanyan, A.; Friedman, B.; Lee, K. *J. Lumin.* **2016**, 171, 149-153.
- Ağırtaş, M.S. *Inorg. Chim. Acta* **2007**, 360 (7), 2499-2502.
- McKeown, N.B. *Phthalocyanines Materials—Synthesis, Structure and Functions*, Cambridge University Press, Cambridge, 1998.
- Mele, G.; Annese, C.; Riccardis, A.D.; Fusco, C.; Palmisano, L.; Vasapollo G.; D'Accolti, L. *Appl. Catal. A.* **2014**, 481, 169-172.

8. Ağırtaş, M.S.; Karatas, C.; Gümüş, S.; Okumus, V. *Z. Anorg. Allg. Chem.* **2015**, 641 (2), 442-447.
9. Azzouzi, S.; Ali, M.B.; Abbas, M.N.; Bausells, J.; Zine N.; Errachid, A. *Org. Electron.* **2016**, 34, 200-207.
10. Medyouni, R.; Elgabsi, W.; Naouali, O.; Romerosa, A.; Al-Ayed, A.S.; Baklouti L.; Hamdi, N. *Spectrochim. Acta, Part A.* **2016**, 167, 165-174.
11. Ağırtaş, M.S. *Dyes Pigments* **2007**, 74, 490-493.
12. Ağırtaş, M.S.; Güven, M.E.; Gümüş, S.; Özdemir, S.; Dündar, A. *Synthetic Met.* **2014**, 195, 177-184.
13. Shaabani, A.; Keshipour, S.; Hamidzad, M.; Shaabani, S. *J. Mol. Catal. A: Chem.* **2014**, 395, 494-499.
14. Sevim, A.M.; Ilgün, C.; Gül, A. *Dyes Pigments* **2011**, 89, 162-168.
15. Cui, L.; Lv, G.; Dou, Z.; He, X. *Electrochim. Acta* **2013**, 106, 272-278.
16. Jasinski, R. *Nature*, **1964**, 201, 1212-1213.
17. Cabir, B.; Caner, N.; Yurderi, M., Kaya, M.; Ağırtaş, M.S.; Zahmakıran, M. *Mater. Sci. Eng. B.* **2017**, 224, 9-17.
18. Ebrahimian, A.; Zanjanchi, M.A.; Noei, H.; Arvand, M.; Wang, Y. *J. Environ. Chem. Eng.* **2014**, 2, 484-494.
19. Erickson, E.M.; Thorum, M.S.; Vasic, R.; Marinkovic, N.S.; Frenkel, A.I.; Gewirth A.A.; Nuzzo, R.G. *J. Am. Chem. Soc.* **2012**, 134, 197-200.
20. Armarego W.L.F.; Chai, C.L.L. *Purification of laboratory Chemicals*, 7nd ed., Butterwordh-Heinemann, Oxford, 2013.
21. Liu, M.O.; Tai, C.H.; Wang, W.Y.; Chen, J.R.; Hu A.T.; Wei, T.H. *J. Organomet. Chem.* **2004**, 689, 1078-1084.
22. Snow, A.W.; Jarvis, N.L. *J. Am. Chem. Soc.* **1984**, 106 (17), 4706-4711.
23. Ağırtaş, M.S.; İzgi, M.S. *J. Mol. Struct.* **2009**, 927, 126-128.
24. Dilber, G, Durmuş, M; Kantekin, H. *Dyes Pigments* **2019**,160, 267-284.
25. Erdoğan, A.; Arıcı, M. *J. Fluorine Chem.* 2014, 166, 127-133.
26. Ağırtaş, M.S. *Dyes Pigments* **2008**, 79, 247-251.
27. Bartlett, M.A.; Mark, K.; Sundermeyer, J. *Inorg. Chem. Commun.* **2018**, 98, 41-43.

ORCID

-  <https://orcid.org/0000-0003-1296-2066> (M. S. Ağırtaş)
-  <https://orcid.org/0000-0001-8108-2404> (C. Durmuş)
-  <https://orcid.org/0000-0003-4735-4511> (B. Cabir)



Optimization, isotherm and kinetics studies of the adsorption of azo dyes on eggshell membrane

Ayşe DİNÇER*, Mervecan SEVİLDİK, Tülin AYDEMİR

on the last page

Chemistry Department, Faculty of Science and Arts, Manisa Celal Bayar University, Yunusemre, Manisa, Turkey

Received: 12 March 2019; Revised: 17 May 2019; Accepted: 18 May 2019

*Corresponding author e-mail: ayse.dincer@cbu.edu.tr

Citation: Dinçer, A.; Sevilidik, M.; Aydemir, T. *Int. J. Chem. Technol.* 2019, 3 (1), 52-60.

ABSTRACT

Eggshell membrane (ESM) was used as an adsorbent for adsorption of reactive red 195 (RR195) and reactive black 5 (RB5) dyes from aqueous solutions. The experimental conditions were optimized via batch system experiments for maximum azo dyes removal. Adsorption of the dyes was pH dependent highly, and the maximum adsorption of RR195 and RB5 occurred at pH 3.0 and 2.0, respectively. For both dyes, the adsorption process was seen to be obeyed pseudo-second order kinetic and the Langmuir isotherm models. Maximum adsorption capacities (Q_{max}) of ESM for RR195 dye and RB5 were found as 76.9 and 333.33 mg g⁻¹, respectively. The thermodynamic parameters were calculated and the adsorption of the dyes was found to be as exothermic and spontaneous. Moreover, the structural characterization of the ESM was performed by FTIR and SEM analysis.

Keywords: Eggshell membrane, reactive red 195, reactive black 5, adsorption.

Yumurta kabuğu zarı üzerine azo boyaların adsorpsiyonunun optimizasyon, izoterm ve kinetik incelemeleri

ÖZ

Yumurta kabuğu zarı (ESM), reaktif kırmızı 195 (RR195) ve reaktif siyah 5 (RB5) boyalarının sulu çözeltilerden adsorpsiyonunda bir adsorban olarak kullanıldı. Maksimum azo boya giderimi için deneysel koşullar kesikli sistem deneyleri ile optimize edildi. Boyaların adsorpsiyonları pH'a oldukça bağımlıydı ve RR195 ve RB5'in maksimum adsorpsiyonları sırasıyla pH 3.0 ve 2.0'de gerçekleşti. Her iki boya için adsorpsiyon işleminin yalnızca ikinci mertebeden kinetik ve Langmuir izoterm modellerine uyduğu görüldü. ESM'nin RR195 ve RB5 için maksimum adsorpsiyon kapasiteleri (Q_{max}) sırasıyla 76,9 ve 333,33 mg g⁻¹ olarak bulundu. Termodinamik parametreler hesaplandı ve boyaların adsorpsiyonunun ekzotermik ve kendiliğinden yürüten olduğu bulundu. Ayrıca, ESM'nin yapısal karakterizasyonu FTIR ve SEM analizleri ile gerçekleştirildi.

Anahtar Kelimeler: Yumurta kabuğu zarı, reaktif kırmızı 195, reaktif siyah 5, adsorpsiyon.

1. INTRODUCTION

Dyes are used in many areas including food colorants, printing, cosmetic, textile-processing and pharmaceutical industries and they are deemed as an important class of pollutants.¹ Azo dyes have one or more N=N bonded groups as chromophore group widely used in the textile industries.²⁻⁴ Production of azo dyes are easy but degradation of these dyes are hard. They have toxic effects on health, many of them are considered as carcinogenic and mutagenic.⁵⁻⁶ Also, colorization of water causes reduction in photosynthesis and afterwards

adversely effects many organisms.^{3,7} Reactive red 195 (RR195) is a monoazo, monochlorotriazine and vinylsulfone dye which is extensively used in dyeing processes.⁸ Reactive black 5 (RB5) is one of the most common dyes that have been used in textile industries and falls into the diazo dye category, as it contains two Ar-N = N-Ar bonds in its structure.⁹

Azo dyes are highly soluble in water and decolorization of these dyes has received increasing attention. To remove these dyes from wastewater, ion exchange, electrocoagulation, reverse osmosis, flocculation, adsorption, membrane filtration, ozonation

and photooxidation methods have been used.¹⁰ Adsorption technique is widely used in general wastewater treatment in the industrial processes and has many advantages such as simplicity of operate, cost and high removal efficiency.¹¹⁻¹⁴

In the present work, the removal of RB5 and RR195 dyes from aqueous solutions were studied by using eggshell membrane (ESM). ESM can be easily obtained as a natural waste product in large quantities. Collagen (type I, V and X), sialoprotein and osteopontin are found mainly in the protein structure of ESM.¹⁵ ESM can be used in many areas as an adsorbent because it has high surface area, water-insoluble fibers and mechanical stable.¹⁶ The experiments were performed by batch system and adsorption conditions were optimized. Equilibrium isotherms and thermodynamic parameters were also studied. ESM characterization was done by FTIR and SEM analyses.

2. EXPERIMENTAL

2.1. Materials

2.1.1 Chemicals

RR195 (Synozol Red HF- 6BN 150% C.I. Reactive Red 195) and RB5 were obtained from dyestuff fabric (Figure 1). Methanol, hydrochloric acid, sodium hydroxide and acetic acid were purchased from Sigma Aldrich (USA) grade.

2.2. Preparation of eggshell membrane

The ESM was obtained from eggshells. First, the eggshells were washed and then incubated in 5% (v/v) acetic acid solution until the calcite totally dissolved. After washing with distilled water, the membrane structures were dried at room temperature for 72 h and ground into small pieces using a blender and homogenizer.

2.3. Dye analysis

Standard solutions of the dyes (0.005-0.05 mg ml⁻¹ for RR195 and 0.005-0.04 mg ml⁻¹ for RB5) were prepared with deionized water. Dye removal studies were analyzed by monitoring the absorbance changes at the maximum wavelengths which are 540 nm for RR195 dye and 597 nm for RB5 using a UV-Vis spectrophotometer (Shimadzu UV-1800) with a 1 cm cell.

2.4. Characterization of ESM

FTIR (Spectrum BX, Perkin Elmer) was used to determine the characteristic functional groups of ESM.

The spectra measurements were taken in the range from 4000 to 400 cm⁻¹ at room temperature. The morphology of ESM was examined after dried under vacuum using Scanning electron microscope (SEM) (Quanta 250 FEG/FEI).

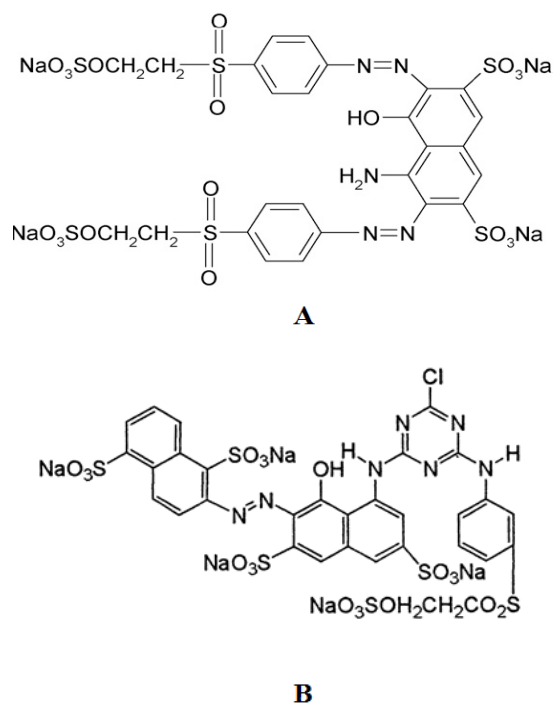


Figure 1. Structures of azo dyes: a) Reactive Black 5, b) Reactive Red 195.

2.5. Adsorption studies

The adsorption studies between RR195 and RB5 dyes and ESM were performed by using batch system at various pH, contact time, temperature and concentrations. The adsorption characteristics of RR195 dye and RB5 were studied by varying pH range from 2.0 to 10.0. Dye removal studies were done at various contact time intervals (5-30 min), temperature values (20-60°C) and the concentrations (0.1-1.2 mg ml⁻¹ for RR195 dye and 0.01-1.75 mg ml⁻¹ for RB5 dye). After the adsorption, the ESM was removed by centrifugation and remaining dye concentration was determined spectrophotometrically.

The amount of dye adsorbed on the ESM was calculated according to Eq. (1).

$$q_e = \frac{(C_0 - C_e) \times V}{m} \quad (1)$$

where q_e is the amount of dye adsorbed (mg g⁻¹), C_0 and C_e is the initial and the equilibrium concentrations of dye (mg ml⁻¹), respectively, V is the volume of solutions (ml) and m is the amount of adsorbent (g).

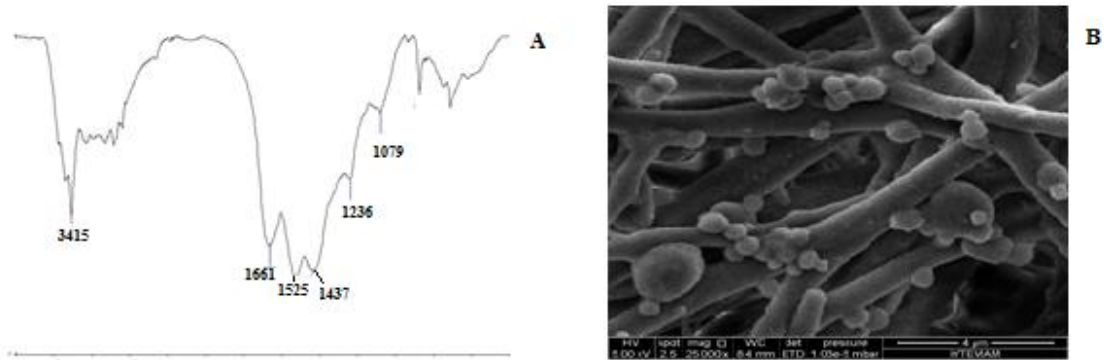


Figure 2. a) FT-IR spectrum of ESM, b) SEM micrograph of ESM.

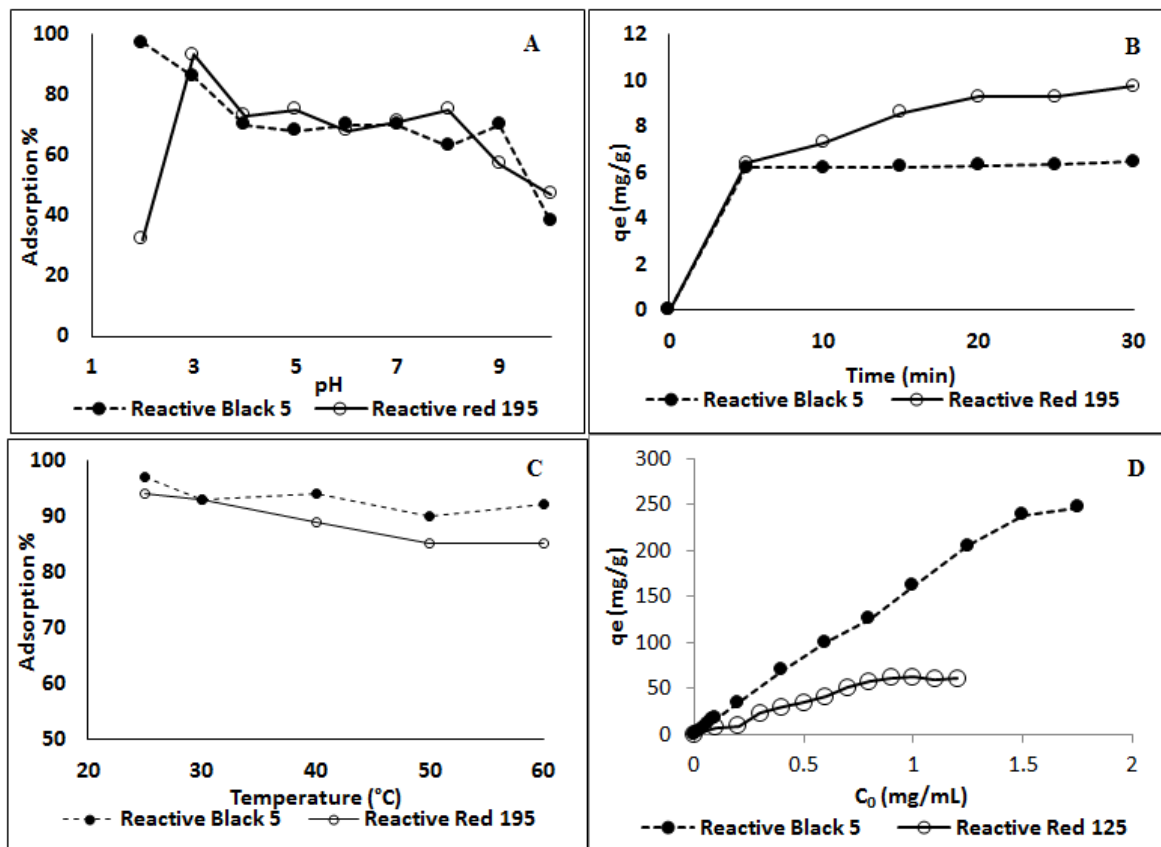


Figure 3. a) Effect of pH on the adsorption of azo dyes on the ESM (contact time 30 min, adsorbent dose 20 mg, temperature 25°C, RB5: 0.04 mg ml⁻¹, RR195: 0.05 mg ml⁻¹); b) Effect of contact time on the adsorption of azo dyes on ESM (RB5: 0.04 mg ml⁻¹, pH 2.0; RR195: 0.05 mg ml⁻¹, pH 3.0; adsorbent dose 20 mg; temperature 25°C); c) Effect of temperature on the adsorption of azo dyes on ESM (RB5: 0.04 mg ml⁻¹, pH 2.0, 15 min; RR195: 0.05 mg ml⁻¹, pH 3.0, 25 min; adsorbent dose 20 mg); d) Effect of initial concentrations of azo dyes on the adsorption (RB5: pH 2.0, 15 min; RR195: pH 3.0, 25 min; adsorbent dose 20 mg; temperature 25°C).

3. RESULTS AND DISCUSSION

3.1 Characterization of the ESM

3.1.1 FT-IR analysis

FT-IR spectrum of ESM was recorded in the range of 4000–400 cm^{-1} (Figure 2a). ESM was first dried for 24 h at 50°C to prevent water related interferences. The peak positions are noticed at 3415, 1661, 1525, 1437, 1236 and 1079 cm^{-1} . The band at 3415 cm^{-1} showed the N–H and O–H groups.¹⁷ The bands at 1661 and 1525 cm^{-1} reflect the amide I (-COO⁻ stretching vibration), amide II respectively. Bands at 1437 cm^{-1} and 1236 cm^{-1} indicate C–C stretching and amide III bands, respectively.¹⁸ The absorption peak at 1079 cm^{-1} probably indicates the presence of C–O stretching/bending vibration (and/or amine C–N stretching) and CH₂ vibration.¹⁹

3.1.2. SEM analysis

Physical properties and the morphology of the adsorbent were characterized by SEM.²⁰ It was used to determine shape, size distribution and porosity of the particle. Scanning electron micrographs of ESM is shown in Figure 2b. ESM has protein fibers which form three-dimensional network structure.¹⁸ ESM has numbers of pores which provide an increase surface area and dye molecules may be easily diffused into these pores.

3.2. Effect of pH

In the adsorption process, pH has critic effect, particularly on adsorption capacity. The pH of the dye solutions was adjusted to 2.0-10.0 by using 0.1 M NaOH or HCl solutions. 20 mg ESM was treated with 0.04 mg ml⁻¹ RB5 and 0.05 mg ml⁻¹ RR195 dye solutions (4 ml) for 30 min. Dye adsorption on ESM was highly dependent to the pH of the medium. The dye adsorption capacity of ESM decreased when the pH values increased from 2.0 to 10.0. Maximum adsorption was reached at pH 3.0 and pH 2.0 for RR195 (93% adsorption) and RB5 (97% adsorption), respectively (Figure 3a). Therefore, further experiments were performed at these pH values. RR195 and RB5 dyes which possess anionic (Dye–SO₃⁻) groups are interacted with the positive charge of the ESM. pH changes affect the net charge of the functional groups of ESM such as carbonyl and amine groups.¹³ Under acidic conditions, the adsorption of two dyes on ESM may be favorable because of the electrostatic interactions. At high pH values, the number of negatively charged groups on ESM increased, so electrostatic repulsion between the adsorbent and dye molecules occurred. Also, at alkaline region, the adsorption of the dye ions may be prevented by OH⁻ ions, so a decrease in adsorption of the dyes were observed.^{21,22}

3.3. Effect of contact time

The contact time between the dye and the adsorbent has an important role in wastewater treatment by adsorption. 20 mg of ESM was added to 0.05 mg ml⁻¹ RR195 (pH 3.0) and 0.04 mg ml⁻¹ RB5 (pH 2.0) solutions. As seen from Figure 3b, in first 5 min of adsorption process, a very fast increase in the adsorption was observed which was due to large number of accessible pores of the adsorbent.^{23,24} The equilibrium was reached at 25 minutes for RR195 and 15 minutes for RB5. At the beginning of the contact time, the adsorption of the dyes was found to be rapid. At 15 and 25 minutes, the adsorption remained almost unchanged and reached to the equilibrium.

3.4. Effect of temperature

In this work, 0.05 mg ml⁻¹ RR195 (pH 3.0) and 0.04 mg ml⁻¹ RB5 (pH 2.0) dye solutions were added to the ESM and shaken gently at various temperature values (25-60°C) for 25 and 15 minutes, respectively. The adsorption percentage of the RR195 and RB5 dyes slightly decreased with an increase in the temperature from 25 to 60°C (Figure 3c). For this reason, the temperature was chosen as 25°C in the following experiments. When the temperature was increased, the solubility of the dyes increased, so stronger interaction forces between dyes and solvent than those between dyes and ESM occurred.^{12,25-27} As the temperature was increased, Brownian movement of dye molecules in solution increased, so the adsorption of both dyes RB5 and RR195 decreased.²⁸ Hydrogen bonding between dye molecules and ESM, which has an important role at the adsorption process, might also lead to be broken because of high temperature.²⁸

3.5. Effects of initial dye concentration

In the experiments, ESM was treated with the solutions of various dye concentration (0.025-0.5 mg ml⁻¹ for RR195 and 0.01-1.75 mg ml⁻¹ for RB5) by mild shaking and the other operational parameters were kept at optimum values. When the initial concentrations of the dyes were increased, the amount of dye adsorbed was found to be increased. The adsorption of RB5 and RR195 reached equilibrium at initial concentrations of 1.75 and 1 mg ml⁻¹ respectively, and then the adsorption remained constant. When the dye concentration was increased, dye adsorption capacities rapidly increased from 1.4 to 247 mg g⁻¹ for RB5 dye and from 4.3 to 60 mg g⁻¹ for RR195 (Figure 3d). An increase in the initial dye concentration may cause an increase in the driving force of the concentration gradient.^{29,30}

3.6. Adsorption thermodynamics

The thermodynamic parameters can be used to estimate effect of temperature on adsorption. The amount of dye adsorbed was calculated from Eq. (2).

$$K_c = X_e / (C_i - X_e) \quad (2)$$

where X_e (mg ml^{-1}) is the concentration of dye adsorbed on ESM at equilibrium, C_i the initial dye concentration, mg ml^{-1} . The equilibrium constant for the adsorption process, K_c , was calculated at various temperatures (298-333 K) according to Eq. (2). Eq. (3) allows to calculate ΔH° and ΔS° of the adsorption by plotting $\ln K_c$ versus $1/T$ in Figure 4.

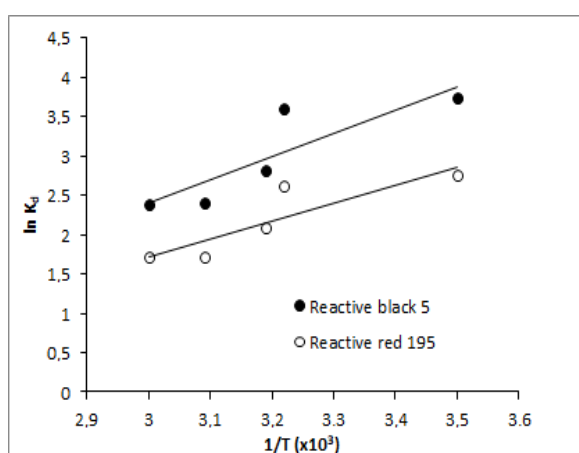


Figure 4. Plots of $\ln K_c$ versus $1/T$. (RB5: 0.04 mg ml^{-1} , pH 2.0, 15 min; RR195: 0.05 mg ml^{-1} , pH 3.0, 25 min; adsorbent dose 20 mg).

$$\ln K_c = (\Delta S^\circ / R) - (\Delta H^\circ / RT) \quad (3)$$

where R ($8.314 \text{ kJ mol}^{-1} \text{ K}^{-1}$) is the gas constant and T is the absolute temperature, respectively. The slope and the intercept of the plots in Figure 4 is equal to $-\Delta H^\circ / R$ and $\Delta S^\circ / R$, respectively. The values of ΔH° and ΔS° for the adsorption of dye on the ESM were calculated from the slope and the intercept of the plots, respectively. ΔG° , ΔH° , ΔS° values obtained are presented in Table 1.

Table 1. Thermodynamic parameters

	T (K)	ΔG° (kJ mol^{-1})	ΔH° (kJ mol^{-1})	ΔS° ($\text{kJ mol}^{-1} \text{ K}^{-1}$)
Reactive Black 5	298	-8.53	-24.6	-0.054
Reactive Red 195	298	-6.72	-24.07	-0.059

The negative value of ΔH° of adsorption indicated an exothermic nature thus is less favorable at higher temperatures. Negative value of ΔS° shows the affinity of the adsorbent for RB5 and RR195 dyes and indicates the randomness adsorption. To calculate the ΔG° value of the adsorption, Eq. (4) was used.

$$\Delta G^\circ = \Delta H - T\Delta S \quad (4)$$

The ΔG° values were calculated as $-8.53 \text{ kJ mol}^{-1}$ and $-6.72 \text{ kJ mol}^{-1}$ for RB5 and RR195, respectively. Negative value of ΔG° shows that the feasibility of the adsorption process is less favored at higher temperatures and nature of the adsorption is spontaneous^{7,31,32} Kyzas and co-workers studied RB5 adsorption on magnetic graphene oxide. They reported negative values of ΔH° ($-21.13 \text{ kJ mol}^{-1}$), ΔG° ($-0.66 \text{ kJ mol}^{-1}$) and ΔS° ($-0.082 \text{ kJ mol}^{-1} \text{ K}^{-1}$) for 300 mg ml^{-1} RB5 concentration at 298 K.³³ From the thermodynamic parameters, Munagapati and co-workers reported that RB5 adsorption on banana peel powder (BPP) was endothermic, feasible and spontaneous.²¹ They found the values of ΔG° , ΔH° , and ΔS° as $-0.198 \text{ kJ mol}^{-1}$, $14.15 \text{ kJ mol}^{-1}$ and $0.056 \text{ kJ mol}^{-1} \text{ K}^{-1}$, respectively.²¹

3.7. Adsorption isotherms

Equilibrium study is important to gain information on the interaction of adsorbate and the adsorbent, so the adsorption capacity of an adsorbent can be evaluated.²⁹ In this work, the experimental data were evaluated by the Freundlich and Langmuir models.³⁴ The logarithmic form of the Freundlich model is defined by Eq.(5).^{12,35}

$$\log q_e = \log K_F + 1/n \log C_e \quad (5)$$

where q_e is the amount dye adsorbed. K_F and n are Freundlich constants. K_F is related to the adsorption capacity and $1/n$ is related to the adsorption intensity. When $\log q_e$ was plotted against $\log C_e$ (Figure 5), $1/n$ and K_F values were calculated from the slope and intercept of the plot and the values at 25°C are given in Table 2.

Another widely used equation in adsorption processes is the Langmuir equation (Eq. (6))³⁵

$$1/q_e = 1/Q^\circ b \cdot 1/C_e + 1/Q^\circ \quad (6)$$

where Q° is the amount of dye adsorbed (mg g^{-1}), which gives the maximum adsorption capacity of ESM and the Langmuir isotherm constant, b (l mg^{-1}) is related to adsorption energy. The calculated Langmuir constants, Q° and b are given in Table 2.

Table 2. Parameters of adsorption isotherms and kinetic models

	Adsorption Isotherms		Kinetic Models		Experimental Capacity (q_{exp})
	Langmuir Isotherms	Freundlich Isotherms	Pseudo-first-order model	Pseudo-second-order model	
	$R^2 = 0.955$	$R^2 = 0.754$	$R^2 = 0.974$	$R^2 = 0.998$	
Reactive Black 5	$Q_{max} = 333.3 \text{ mg g}^{-1}$	$K_F = 56.23 \text{ mg g}^{-1}$	$q_e = 77.1 \text{ mg g}^{-1}$	$q_e = 256.4 \text{ mg g}^{-1}$	247 mg g^{-1}
	$b = 0.11 \text{ ml mg}^{-1}$	$1/n = 0.392$	$k_1 = 0.096 \text{ min}^{-1}$	$k_2 = 2.76 \cdot 10^{-3} \text{ g mg}^{-1} \text{ min}^{-1}$	
	$R^2 = 0.918$	$R^2 = 0.2622$	$R^2 = 0.8922$	$R^2 = 0.9971$	
Reactive Red 195	$Q_{max} = 76.9 \text{ mg g}^{-1}$	$K_F = 63.2 \text{ mg g}^{-1}$	$q_e = 13.25 \text{ mg g}^{-1}$	$q_e = 62.5 \text{ mg g}^{-1}$	62.5 mg g^{-1}
	$b = 2.17 \text{ ml mg}^{-1}$	$1/n = 0.046$	$k_1 = 0.07 \text{ min}^{-1}$	$k_2 = 0.02 \text{ g mg}^{-1} \text{ min}^{-1}$	

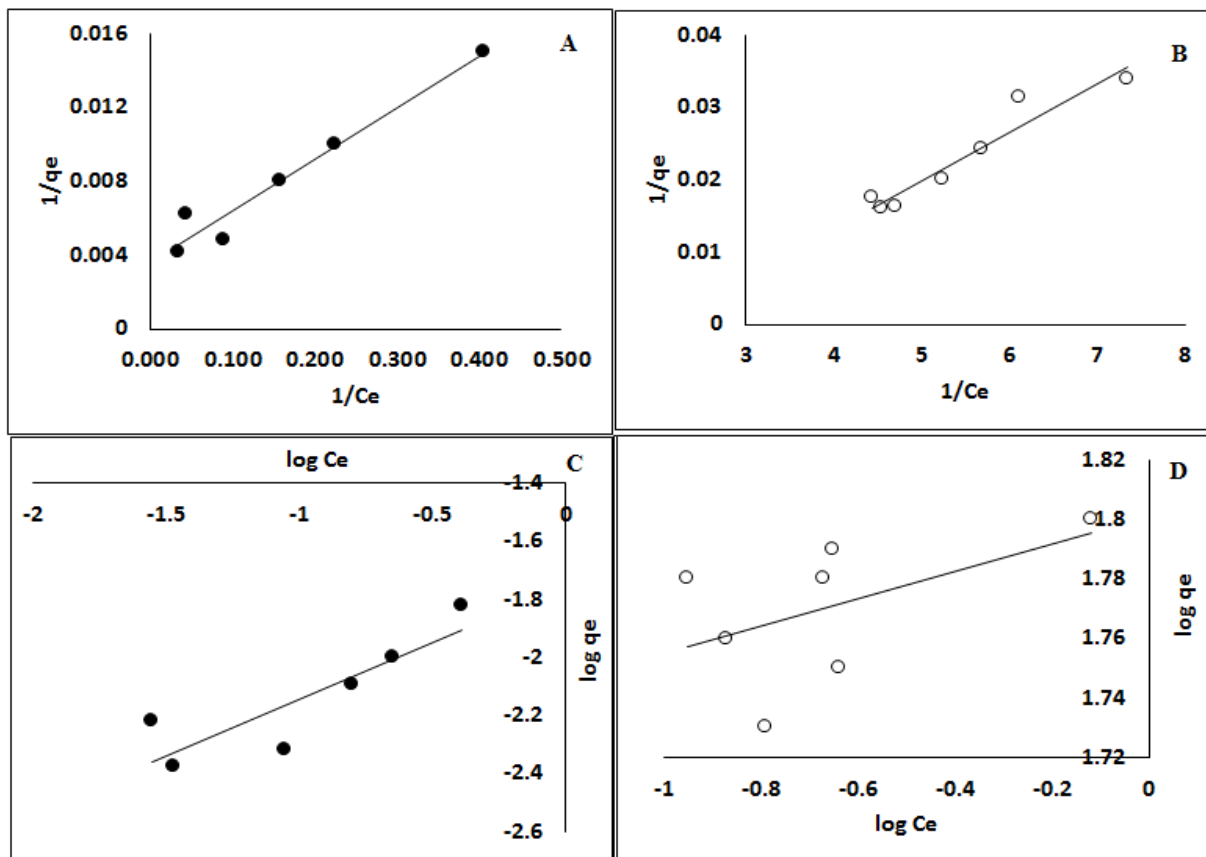


Figure 5. Langmuir (a and b) and Freundlich (c and d) isotherm graphs of RB5 (●) and RR195 (○) dyes.

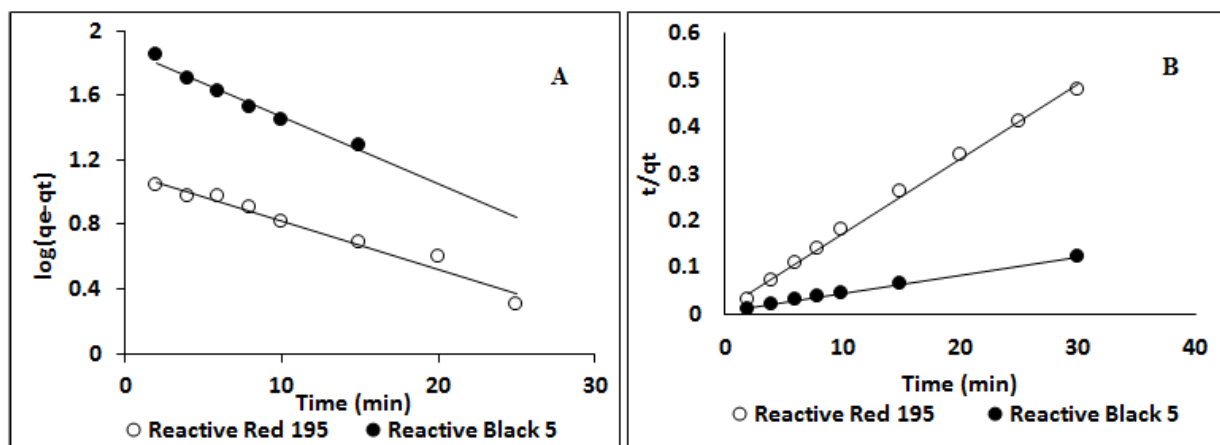


Figure 6. Pseudo first order (a) and pseudo second order (b) kinetics of RB5 (●) and RR195 (○) dyes.

The higher R^2 values of Langmuir over Freundlich model showed the suitability of the Langmuir model than the Freundlich model. The R^2 values from the Langmuir isotherm for the adsorption of RB5 and RR195 are 0.955 and 0.918, respectively. The maximum adsorption capacities obtained from the Langmuir isotherms were found to be 76.9 and 333.33 mg g^{-1} for RR195 and RB5, respectively. Dimensionless separation factor, R_L is used to analyze the adsorption process. When the R_L value is between 0 and 1 or higher than 1, this means the adsorption process is favorable or unfavorable, respectively. If the R_L equals to 1 or 0, it shows the adsorption process linear or irreversible, respectively.³⁵ the R_L can be expressed as:

$$R_L = 1/(1 + bC_0) \quad (7)$$

Where b is the Langmuir constant and C_0 is the initial dye concentration (mg ml^{-1}).

The R_L values for the adsorption of RR195 and RB5 dyes onto ESM was determined as 0.33 and 0.84 respectively, showing that the adsorption process was favorable. Chang and Shih studied the adsorption of RB5 onto magnetic iron oxide nanoparticles (IONPs) and they reported the adsorption process were well compatible with the Langmuir and Freundlich equations.³⁶ They calculated that Langmuir isotherm capacity was 11.29 mg g^{-1} at 25°C. Kyzas co-workers studied the removal of RB5 by magnetic graphene oxide synthesized by impregnation (mGOi) and magnetic graphene oxide synthesized by co-precipitation (mGOp) at 25°C and pH 3.0, and they calculated that the maximum adsorption capacities (Q_{max}) were 164 and 188 mg g^{-1} , respectively.³³ Their results were fitted to the Langmuir model. Munagapati co-workers used banana peel powder (BPP) as an adsorbent to remove reactive black 5 and congo red from aqueous solutions. Their adsorption equilibrium results were compatible with Langmuir

isotherm model and they calculated the adsorption capacity as 49.2 mg g^{-1} .²¹ Belessi co-workers studied adsorption of RR195 dye on TiO_2 surface and they reported that equilibrium data fitted very well with the Langmuir isotherm. At 30°C and pH 3.0, Langmuir adsorption capacity was calculated as 87 mg g^{-1} .¹⁴ Kamranifar and co-workers reported the removal of RR195 using powder and ash of barberry stem. Adsorption isotherm was fitted to both the Freundlich and Langmuir isotherms for the barberry stem powder. However, Freundlich isotherm was compatible for the adsorption of RR195 on barberry stem ash. Q_{max} (mg g^{-1}) values were calculated as 15.72 mg g^{-1} and 6.44 mg g^{-1} for barberry stem (powder) and barberry stem (ash) respectively.⁶

3.8. Adsorption kinetics

To obtain information about the performance of the sorbent material, the pseudo-first-order (Eq. (8)) and the pseudo-second-order (Eq. (9)) kinetic models were used.

$$\log(q_e - q_t) = \log q_e - \frac{k_1}{2.303} t \quad (8)$$

$$\frac{t}{q_e} = \frac{1}{k_2 q_e^2} + \frac{t}{q_e} \quad (9)$$

where q_t (mg g^{-1}) represents the adsorption capacity of dyes adsorbed on eggshell membrane at any time t (min). k_1 (min^{-1}) is the rate constant of the pseudo-first-order model and k_2 ($\text{g mg}^{-1} \text{min}^{-1}$) is the rate constant of the pseudo-second-order model.³⁷⁻³⁸

The results of the pseudo first-order and pseudo second order models for RR195 and RB5 adsorbed on ESM are shown in Figure 6. All the kinetic parameters calculated from the intercepts and the slopes of the plots

in Figure 6 are shown in Table 2. The R^2 (correlation coefficient) of the pseudo first-order kinetic model was determined as 0.974 and 0.8922 for RB5 and RR195, respectively. R^2 values from the pseudo second-order model were found as 0.998 and 0.9971 for RB5 and RR195 respectively. For the adsorption of both dyes, the theoretical q_e values calculated from the pseudo-second order kinetics are much higher than those of the pseudo first order kinetics and they very closed to the experimental q_{exp} values. This situation indicates that the adsorption is a good fit to the pseudo second order kinetic model. Kyzas and co-workers reported that the adsorption kinetics of RB5 on magnetic graphene oxide fitted to the pseudo-second order model.³³ Belessi and co-workers reported the sorption kinetics of RR195 on the surface of TiO₂ nanoparticles fitted to the pseudo-second-order kinetic model.¹⁴

4. CONCLUSIONS

ESM was used as an adsorbent for the removal of RR195 and RB5 dyes. Adsorption conditions were optimized as a function of pH, temperature, contact time and concentrations of the adsorbates. The adsorption of RR195 and RB5 on ESM was very dependent to the pH of the medium and maximum adsorption was observed at pH 3.0 for RR195 and 2.0 for RB5, respectively. The optimum contact time was found as 25 min and 15 min for RR195 and RB5, respectively. The negative values of ΔG° indicate the overall adsorption process is spontaneous. The ΔG° value was calculated as -6.72 kJ mol⁻¹ for RR195 and -8.530 kJ mol⁻¹ for RB5 at 298 K. The negative values of ΔH° showed that the adsorption of RR195 and RB5 by ESM was exothermic. Adsorption isotherm of the ESM was fitted to the Langmuir isotherm model and the Q_{max} value was calculated as 76.9 mg g⁻¹ for RR195 and 333.33 mg g⁻¹ for RB5, respectively. The present work reveals that the ESM is a promising material for the removal of dyes from aqueous solutions.

Conflict of interests

Authors declare that there is no a conflict of interest with any person, institute, company, etc.

REFERENCES

- Hassaan, M.A.; El Nemr, A. *Am. J. Environ. Sci. Eng.* **2017**, 1 (3), 64-67.
- Benkhaya, S.; El Harfi, S.; El Harfi, A. *Appl. J. Envir. Eng. Sci.* **2017**, 3 (3), 311-320.
- Singh, P.K.; Singh, R.L. *Int. J. Appl. Sci. Biotechnol.* **2017**, 5 (2), 108-126.
- El-Naggar, M.E.; Radwan, E.K.; El-Wakeel, S.T.; Kafafy, H.; Gad-Allah, T.A.; El-Kalliny, A.S.; Shaheen, T.I. *Int. J. Biol. Macromol.* **2018**, 113, 248-258.
- Mahmoud, M.E.; Nabil, G.M.; El-Mallah, N.M.; Bassiouny, H.I.; Kumar, S.; Abdel-Fattah, T.M. *J. Ind. Eng. Chem.* **2016**, 37, 156-167.
- Kamranifar, M.; Khodadadi, M.; Samiei, V.; Dehdashti, B.; Sepehr, M.N.; Rafati, L.; Nasseh, N.; *J. Mol. Liq.* **2018**, 255, 572-577.
- Karadağ, D.; Turan, M.; Akgul, E.; Tok, S.; Faki, A. *J. Chem. Eng. Data* **2007**, 52, 1615-1620.
- Nawahwi, M.Z.; Ibrahim, Z.; Yahya, A. *J. Bioremed. Biodeg.* **2013**, 4, 1-7.
- Jager, D.; Kupka, D.; Vaclavikova, M.; Ivanicova, L.; Gallios, G. *Chemosphere* **2018**, 190, 405-416.
- Al-Degs, Y.S.; El-Barghouthi, M.I.; El-Sheikh, A.H.; Walker, G.M. *Dyes Pigments* **2007**, 77 (1), 1-8.
- Ghaedi, M.; Sadeghian, B.; Pebdani, A.A.; Sahraei, R.; Daneshfar, A.; Duran, C. *Chem. Eng. J.* **2012**, 187, 133-141.
- Aljeboree, A.M.; Alshirifi, A.N.; Alkaim, A.F. *Arab. J. Chem.* **2017**, 10, S3381-S3393.
- Arami, M.; Limaee, N.Y.; Mahmoodi, N.M. *Chemosphere.* **2006**, 65, 1999-2008.
- Belessi, V.; Romanos, G.; Boukos, N.; Lambropouloud, D.; Trapalis, C. *J. Hazard. Mater.* **2009**, 170, 836-844.
- Yi, F.; Guo, Z.X.; Zhang, L.X.; Yu, J.; Li, Q. *Biomaterials* **2004**, 25, 4591-4599.
- Tsai, W.T.; Yang, J.M.; Lai, C.W.; Cheng, Y.H.; Lin, C.C.; Yeh, C.W. *Bioresource Technol.* **2006**, 97, 488-493.
- Abdel-Khalek, M.A.; Abdel Rahman, M.K.; Francis, A.A. *J. Environ. Chem. Eng.* **2017**, 5, 319-327.
- Xin, Y.; Li, C.; Liu, J.; Liu, J.; Liu, Y.; He, W.; Gao, Y. *R. Soc. Open sci.* **2018**, 5, 180532.
- Karan, S.K.; Maiti, S.; Paria, S.; Maitra, A.; Si, S.K.; Kim, J.K.; Khatua, B.B. *Mater. Today* **2018**, 9, 114-125.
- Hussien, M.A.; El-Bindary, A.A.; El-Sonbati, A.Z.; Shoaib, A.F.; El-Boz, R.A. *J. Mater. Environ. Sci.* **2016**, 7 (11), 4214-4225.

21. Munagapati, V.S.; Yarramuthi, V.; Kim, Y.; Lee, K.M.; Kim, D.S. *Ecotoxicol. Environ. Saf.* **2018**, 148, 601-607.
22. Aksu, Z.; Dönmez, G. *Chemosphere* **2003**, 50, 1075-1083.
23. Paşka, O.; Ianoş, R.; Păcurariu, C.; Brădeanu, A. *Water Sci. Technol.* **2014**, 69, 1234-1240.
24. Mohebali, S.; Bastani, D.; Shayesteh, H. *J. Mol. Struct.* **2019**, 1176, 181-193.
25. Dotto, G.L.; Lima, E.C.; Pinto, L.A. *Bioresour. Technol.* **2012**, 103, 123-130.
26. Zhou, L.; Jin, J.; Liu, Z.; Liang, X.; Shang, C. *J. Hazard. Mater.* **2011**, 185, 1045-1052.
27. Zhou, Z.; Lin, S.; Yue, T.; Lee, T. *J. Food Eng.* **2014**, 126, 133-141.
28. Li, H.; Huang, G.; An, C.; Hu, J.; Yang, S. *Ind. Eng. Chem. Res.* **2013**, 52, 15923-15931.
29. Chiou, M.S.; Li, H.Y. *J. Hazard. Mater.* **2002**, 93, 233-248.
30. Sun, D.; Zhang, X.; Wu, Y.; Liu, X. *J. Hazard. Mater.* **2010**, 181, 335-342.
31. Özcan, A.; Öncü, E.M.; Özcan, A.S. *J. Hazard. Mater.* **2006**, 129, 1-3.
32. Nawi, M.A.; Sabar, S.; Jawad, A.H.; Sheilatina, Wan Ngah W.S. *Biochem. Eng. J.* **2010**, 49, 317-325.
33. Kyzas, G.Z.; Travlou, N.A.; Kalogirou, O.; Deliyanni, E.A. *Materials* **2013**, 6, 1360-1376.
34. Adane, B.; Siraj, K.; Meka, N. *Green Chem. Lett. Rev.* **2015**, 8 (3-4), 1-12.
35. Foo, K.Y.; Hameed, B.H. *Chem. Eng. J.* **2010**, 156, 2-10.
36. Chang, M.; Shih, Y. *J. Environ. Manage.* **2018**, 224, 235-242.
37. Xue Z, Zhao S, Zhao Z, Li, P.; Gao, J. *J. Mater. Sci.* **2016**, 51, 4928-4941.
38. Chen A, Li Y, Yu Y, Li, Y.; Xia, K.; Wang, Y.; Li, S. *J. Mater. Sci.* **2016**, 51, 7016-7028.

ORCID

 <https://orcid.org/0000-0001-6158-1775> (A. Dinçer)

 <https://orcid.org/0000-0001-6883-8748> (M. Sevilcik)

 <https://orcid.org/0000-0002-2968-4456> (T. Aydemir)



Stress behaviours of viscoelastic flow around square cylinder

Guler Bengusu TEZEL^{1*}, Kerim YAPICI², Yusuf ULUDAG³

on the last page

¹Department of Chemical Engineering, Faculty of Engineering and Architecture, Abant Izzet Baysal University, 14280, Bolu, Turkey²Department of Chemical Engineering, Faculty of Engineering and Architecture, Suleyman Demirel University, 32260, Isparta, Turkey³Department of Chemical Engineering, Middle East Technical University, 06800 Ankara, Turkey

Received: 8 April 2019; Revised: 20 May 2019; Accepted: 21 May 2019

*Corresponding author e-mail: gulerbengusutezel@ibu.edu.tr

Citation: Tezel, G.B.; Yapici, K.; Uludag, Y. <i>Int. J. Chem. Technol.</i> 2019, 3 (1), 61-66.
--

ABSTRACT

In this study, it is aimed the numerically investigation of the flow of liner PTT (Phan-Thien-Tanner) fluid, which is a viscoelastic fluid model over limited square obstacle by finite volume method. The finite volume method has been used for simultaneous solution of continuity, momentum and fluid model equations with appropriate boundary conditions. The effects of the inertia in terms of Reynolds number, Re , ($0 < Re < 20$) and the of elasticity in terms of Weissenberg number, We , ($1 < We < 15$) of PTT flow on vertical and shear stress areas are examined in detail.

Keywords: Square cylinder, confined channel, viscoelastic flow, PTT fluid.

Kare silindir etrafındaki viskoelastik akışın stres davranışları

ÖZ

Bu çalışmada viskoelastik akışkan modeli olan liner PTT (Phan-Thien-Tanner) akışkanın sınırlandırılmış kare engel üzerinden olan akışının sonlu hacimler yöntemi ile nümerik olarak incelenmesi hedeflenmiştir. Sonlu hacimler yöntemi, uygun sınır koşulları ile birlikte, süreklilik, momentum ve akışkan model eşitliklerinin eş zamanlı çözümü için kullanılmıştır. PTT akışın Reynolds sayısı, Re , ($0 < Re < 20$) cinsinden eylemsizliğinin ve Weissenberg sayısı, We , ($1 < We < 15$) cinsinden elastisitesinin, dikey ve kayma gerilim alanları üzerine olan etkileri detaylı bir şekilde incelenmiştir

Anahtar Kelimeler: Kare silindir, sınırlandırılmış kanal, viskoelastik akış, PTT akışkan.

1. INTRODUCTION

Flow of fluids over the square obstacles is present in many engineering processes such as fins in heat exchangers, coating processes, cooling towers, extruders and membrane processes.¹ With such crucial industrial implications, hydrodynamics of such flows has been subject of many computational studies in the literature. There are many studies on Newtonian fluid flow around a circular obstacle. For instance, Hassanzadeh and co-workers.² performed numerical study on the flow around a sphere using finite volume method. They presented flow structures around sphere in terms of velocity,

streamlines, pressure distributions at high Re (Reynolds number) numbers. Their numerical predictions were also confirmed by the experimental visualizations. As an experimental visualization method, particle image velocimetry was used in this study. Particle Image Velocimetry (PIV) is used to carry out flow field measurements experimentally. This technique enables the qualitative and quantitative flow visualization of the flow field.² Pioneer study on this geometry was given by Breuer and co-workers.³ They analyzed laminar two-dimensional Newtonian flow around a square cylinder using finite volume and lattice Boltzmann methods.

In this study, blockage ratio B , is the ratio over the

obstacle dimension and channel height, was 1/8. The results obtained from two methods were also good agreement. They observed bigger wake size with increased Re . In the analysis by Sen and co-workers,⁴ with $B = 1/100$ Newtonian flow over a square obstacle for $Re \leq 40$ was studied using a finite element formulation. They also modelled the flows over the cylinders of circular and elliptical ones. They reported effect of Re on the flow structure. In their recent study Puig-Aranega and co-workers⁵ searched Newtonian flow around a square cylinder obstacle using lattice Boltzmann method for $50 \leq Re \leq 100$. They reported strong impact of imposed boundary conditions on the stress field around the cylinder. However, in the literature studies on non-Newtonian flow (inelastic flow) case over the obstacles are smaller than those Newtonian flows. Dhiman and co-workers⁶ employed power-law fluids flow around a confined square cylinder using finite volume method. Other study of Dhiman and co-workers⁷ showed stronger impact of power law fluids at low values of Re compared as to the high values of Re . Ehsan and co-workers⁸ also studied the inertia effects on the flow fields under both laminar and turbulent conditions. Their main finding was that decreasing drag effects was observed when the inertial effects increased. Moreover, Nilmarkar and co-workers⁹ obtained numerically Bingham plastic fluid flow past a square cylinder at $Re = 0$. The effect of Bingham number, B_i considered as a yielding stress parameter, on the stress and pressure fields was reported in their study. They observed the weaker dependence of flow fields on B_i at its increased values.

On the other hand, viscoelastic flow hydrodynamics are also significant for the industrial implications due to revealing both viscous and elastic effects on the flow field. Hence, this study mainly deals with the flow of a viscoelastic linear PTT (Phan-Thien-Tanner) fluid, around a confined square obstacle numerically.

2. NUMERICAL METHODOLOGY

Two-dimensional flow of linear PTT fluid around a confined square is considered in this study under the isothermal conditions. The flow system is sketched as in Figure 1. The blockage ratio is 1/4. The continuity, momentum and constitutive PTT equations in rectangular coordinates (x, y) are presented in Equations (1) and (2). For a two-dimensional flow system equation can be given as:

Continuity

$$\frac{\partial u}{\partial x} + \frac{\partial v}{\partial y} = 0$$

x-momentum

$$\frac{\partial}{\partial x} \left(Re uu - (1 - w_r) \frac{\partial u}{\partial x} \right) + \frac{\partial}{\partial y} \left(Re vu - (1 - w_r) \frac{\partial u}{\partial y} \right) = - \frac{\partial p}{\partial x} + \frac{\partial \tau_{xx}}{\partial x} + \frac{\partial \tau_{xy}}{\partial y} \tag{1}$$

y-momentum

$$\frac{\partial}{\partial x} \left(Re uv - (1 - w_r) \frac{\partial v}{\partial x} \right) + \frac{\partial}{\partial y} \left(Re vv - (1 - w_r) \frac{\partial v}{\partial y} \right) = - \frac{\partial p}{\partial y} + \frac{\partial \tau_{xy}}{\partial y} + \frac{\partial \tau_{yx}}{\partial x}$$

Eq. (2) gives viscoelastic constitutive linear PTT mode.1.¹⁰ This viscoelastic model serves shear thinning and normal stress effects in the flow field. Dimensionless forms of the stress components τ_{xx} , τ_{yy} , τ_{xy} are given as follows:

Phan-Thien-Tanner (PTT) constitutive equation:

Stress components of τ_{xx}

$$\left(1 + \varepsilon \frac{We}{w_r} (\tau_{xx} + \tau_{yy}) \right) \tau_{xx} + \frac{\partial}{\partial x} (We u \tau_{xx}) + \frac{\partial}{\partial y} (We v \tau_{xx}) = We \left(\frac{\partial u}{\partial y} - \frac{\partial v}{\partial x} \right) \tau_{xy} + 2We \frac{\partial u}{\partial x} \tau_{xx} + We \left(\frac{\partial u}{\partial y} + \frac{\partial v}{\partial x} \right) \tau_{xy} + 2w_r \frac{\partial u}{\partial x} \tag{2}$$

Stress components of τ_{yy}

$$\left(1 + \varepsilon \frac{We}{w_r} (\tau_{xx} + \tau_{yy}) \right) \tau_{yy} + \frac{\partial}{\partial x} (We u \tau_{yy}) + \frac{\partial}{\partial y} (We v \tau_{yy}) = We \left(\frac{\partial v}{\partial x} - \frac{\partial u}{\partial y} \right) \tau_{xy} + 2We \frac{\partial v}{\partial y} \tau_{yy} + We \left(\frac{\partial u}{\partial y} + \frac{\partial v}{\partial x} \right) \tau_{xy} + 2w_r \frac{\partial v}{\partial y}$$

Stress components of τ_{xy}

$$\left(1 + \varepsilon \frac{We}{w_r} (\tau_{xx} + \tau_{yy}) \right) \tau_{xy} + \frac{\partial}{\partial x} (We u \tau_{xy}) + \frac{\partial}{\partial y} (We v \tau_{xy}) = - \frac{1}{2} We (\tau_{xx} - \tau_{yy}) \left(\frac{\partial u}{\partial y} - \frac{\partial v}{\partial x} \right) + w_r \left(\frac{\partial u}{\partial y} + \frac{\partial v}{\partial x} \right) + \frac{1}{2} We (\tau_{xx} + \tau_{yy}) \left(\frac{\partial u}{\partial y} + \frac{\partial v}{\partial x} \right)$$

where u, v are the velocities, p is the pressure, $w_r = 1 - \beta$ and the parameter β is the ratio of the retardation and relaxation time and ε is extensibility parameter. The Reynolds number (Re) and the Weissenberg number (We) which is defined as the ratio of characteristic fluid relaxation time to characteristic time scale in the flow are given through ($Re = \rho UH / \eta_0$), where η_0 is the total viscosity of polymer and solvent, and $We = \lambda u / H$, where λ is relaxation constant of the viscoelastic fluid. Re is important dimensionless number to characterize flow pattern and it compares the inertial and viscous forces in the flow field. We is the other dimensionless number that describes the dominance of elastic forces over viscous forces of the flow. The material parameters β and ε are set as 0.2 and 0.25, respectively.

A finite volume method^{11,12} is used to obtain discrete form of the flow equations. Convective terms in the PTT equations are computed by using of CUBISTA¹³ scheme. The detailed numerical methods have been also presented in the study of Tezel and co-workers.¹⁴

3. RESULTS AND DISCUSSION

Nonhomogeneous structured mesh is employed to simulate the flow field with $B = 1/4$. Smallest mesh size is used near the obstacle walls in order to resolve thin boundary layers and high gradients in the flow as depicted in Figure 1. Minimum size of the mesh has $\Delta_x = 0.02$ and $\Delta_y = 0.01$. Total number of the cells is 372 x 162.

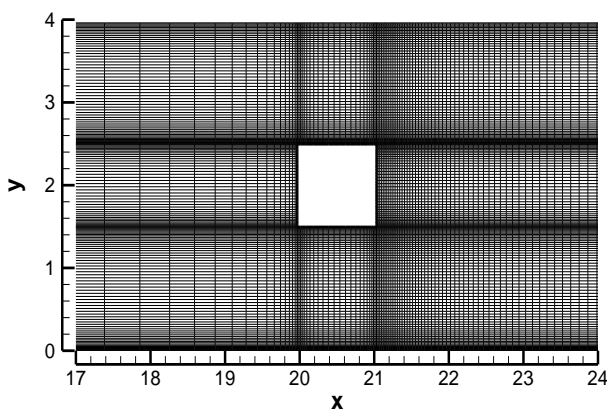


Figure 1. Non-uniform mesh structure around the square obstacle.

Viscoelastic fluids have normal stresses (τ_{xx}) due to revealing the elastic effects of the fluid flow rather than Newtonian flow. Normal stresses are resulted from velocity (ux) changings through the flow direction. Figures 2a and 2b depict the impact of the We numbers on the normal stress component τ_{xx} at creeping flow. In these figures dimensionless stress values are -0.1 and 1.

Symmetric normal stress field is observed. In the flow direction, normal stresses go further at the top and bottom of the obstacle. As We is increased, normal stress contours stretch longer distances in the behind of the obstacle (wake region). Otherwise, at the channel wall there is no amending normal stress profile with respect to We . When We is 15, the impact of elasticity seems to be by the extent of the shear thinning compared to the case of $We = 5$. As in Figure 2b negative normal stresses occur around the obstacle. These stresses dominantly develop in front of the object. When at $We = 15$, there is no observation of a negative normal stress as in Figure 2b due to high elasticity of the flow. At the front of the obstacle, sudden separated flows near the front of the obstacle cause the formation of Hoop stresses. It can be explained as larger normal stress changings through the tangential direction in the flow field due to stretching of elastic forces over the surface of the square cylinder. Similar findings are also offered for the circular cylinder by Oliveira and co-workers.¹³ This formation of Hoop stresses comes from the sudden velocity changings in front surface of the square cylinder.

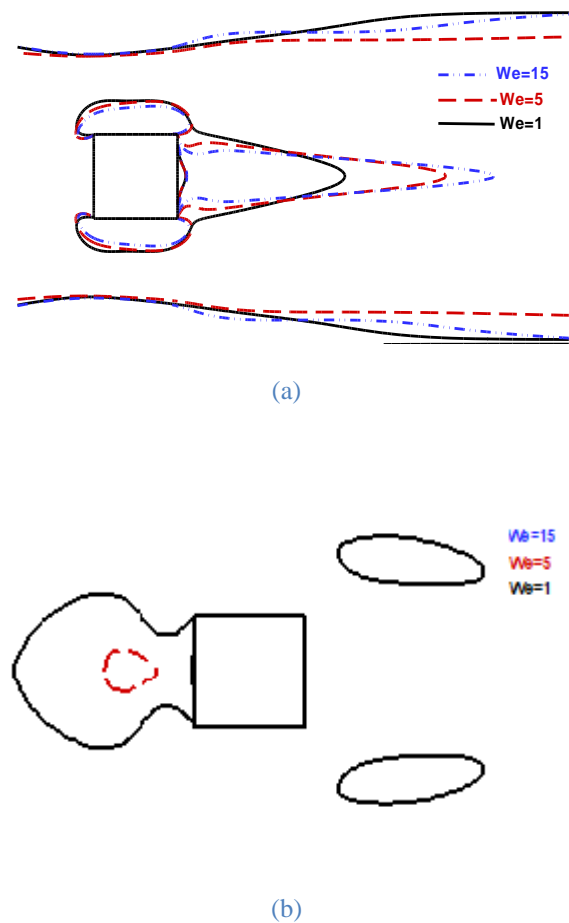
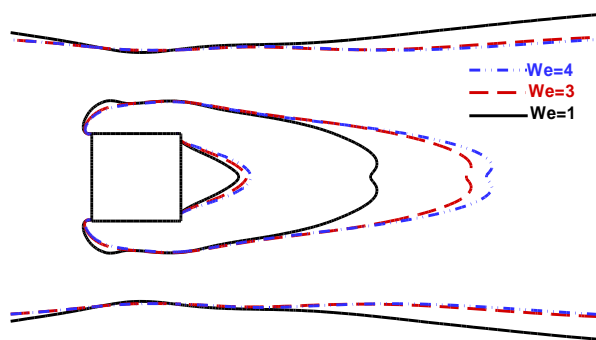
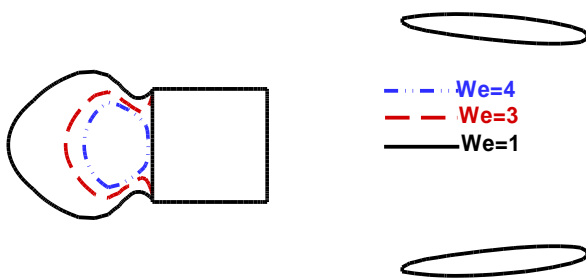


Figure 2. Normal stress profile for $Re = 0$ at contour values a) 1 b) -0.1.

Figures 3 and 4 depict the normal stress field at $Re = 10$ and $Re = 20$, respectively. Due to the stability problems encountered in the numeric solutions, We was capped at 4. As increased Re , behind the obstacle (in the wake region), normal stress field grows up to bigger size. As shown in Figure 4a, at $Re = 20$, normal stress divides into two symmetric fields in the wake region. Negative stress fields occur in this region since dominance of Hoop stresses. Due to the We ranges in Figures 3b and 4b, an increase in the extent of the stress fields is observed near the channel wall suggesting weaker shear thinning effects than $We = 15$ case in Figure 2b. With the higher values of We , normal stresses modify progressively around the cylinder reported as in Norouzi and co-workers's study.¹⁵

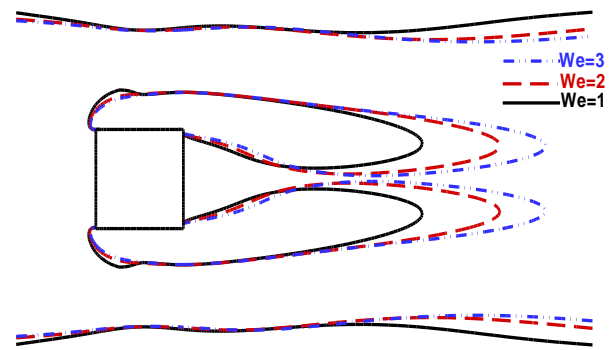


(a)

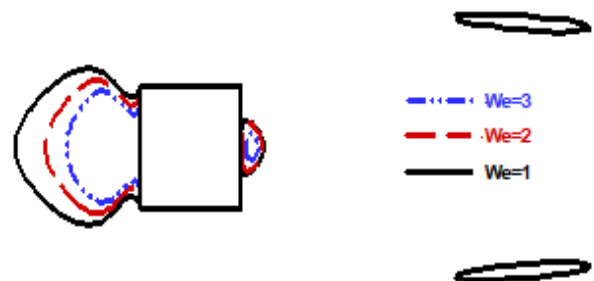


(b)

Figure 3. Normal stress profile for $Re = 10$ at the contour value a) 1, b) -0.1.



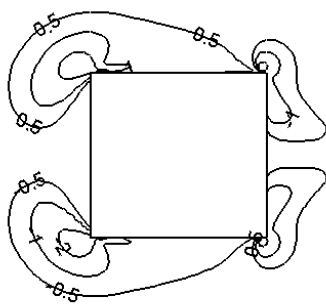
(a)



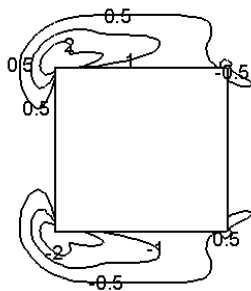
(b)

Figure 4. Normal stress profiles for $Re = 20$ at the contour value a) 1, b) -0.1.

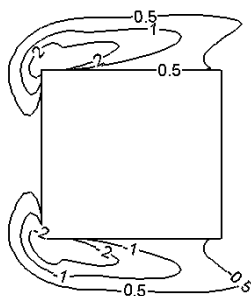
Figure 5 shows the effect of the Re on the shear stress field, τ_{xy} . Shear stress is caused by viscous forces between the fluid molecules. Hence, u_x changes with respect to the perpendicular direction to the flow field. At the front corners of obstacle, hoop stresses cause the higher shear stress distribution due to instantaneous variation in viscoelastic flow velocity. At creeping flow, as shown in Figure 5a, at the back corners of the obstacle shear stresses also occur. As Re increases, at the front corners' higher values of the shear stress distend to the upper and lower surfaces of the obstacle as in Figure 5b and 5c due to flow separation effect of viscoelastic flow especially in the front corners.



(a)



(b)



(c)

Figure 5. Shear stress profile for $We = 3$, a) $Re = 0$, b) $Re = 10$, c) $Re = 20$.

4. CONCLUSIONS

In the present study, normal and shear stresses distribution of viscoelastic fluid flowing over the obstacle is studied using numerical method. The results of the study can be summarized as follows.

- For stable solutions, at higher value of Re there is the lowest limit of We and at lower value of Re there is highest limit of We .
- Low We and high Re conditions supply the occurrence of negative normal stresses in the flow field.

- When the fluid inertia increases, in the wake region normal stresses get bigger size and the stress region is observed at the top and bottom surfaces of the pipe.
- Shear stresses occur in the flow region when the fluid flow is tangential to the boundaries of the obstacle at increased Re

Conflict of interests

Authors declare that there is no a conflict of interest with any person, institute, company, etc.

REFERENCES

1. Liang, C.; Papadakis, G.; Luo, X. *Comput. Fluids* **2009**, 38, 950-964.
2. Hassanzadeh, R.; Sahin, B.; Ozgoren, M. *Int. J. Comput. Fluid D.* **2011**, 25, 535-545.
3. Breuer M.; Bernsdorf, M.; Zeiser, T.; Durst, T. *Int. J. Heat Fluid Fl.* **2000**, 21, 186-196.
4. Sen, S.; Mittal, S.; Biswas, G. *Int. J. Numer. Meth. Fl.* **2011**, 67, 1160-1174.
5. Puig-Aranega, A.; Burgos, J.; Cito, S.; Cuesta, I.; Saluena, C. *Int. J. Comput. Fluid D.* **2015**, 29, 434-446.
6. Dhiman, A.K.; Chhabra, R.P.; Eswaran, V. *J. Non-Newton. Fluid Mech.* **2008**, 148, 141-150.
7. Dhiman, A.K.; Chhabra, R.P.; Eswaran, V. *J. Chem. Eng. Res. Des.* **2006**, 84, 300-310.
8. Ehsan, I.; Mohammad, S.; Reza, N.; Ali, J. *Int. J. Phys. Sci.* **2012**, 7, 988-1000.
9. Nirmalkar, N., Chhabra R.P.; Poole R.J. *J. Non-Newton. Fluid Mech.* **2012**, 171-172, 17-30.
10. Phan-Thien, N.; Tanner, R.I. *J. Non-Newton. Fluid Mech.* **1977**, 2, 353-365.
11. Patankar, S.V.; Spalding, D.B. *Int. J. Heat Mass Tran.* **1972**, 15, 1787.
12. Versteeg H. K.; Malalasekera W. An introduction to computational fluid dynamics: The finite volume method, 2nd Edition, Prentice Hall, USA, 1995.
13. Alves, M.A., Oliveira P.J.; Pinho F.T. *Int. J. Numer. Meth. Fl.* **2003**, 4, 47-75.

DOI: <http://dx.doi.org/10.32571/ijct.549930>


E-ISSN:2602-277X


14. Tezel, G. B.; Yapici, K.; Uludag, Y. *Period Polytech. Chem. Eng.* **2019**, 63, 190-199.

15. Norouzi, M.; Varedi, S.R.; Zamani, M. *Korea-Aust. Rheol. J.* **2015**, 27, 213-225.

ORCID

 <https://orcid.org/0000-0002-0671-208X> (G.B. Tezel)


 <https://orcid.org/0000-0002-3902-9375> (K. Yapici)

 <https://orcid.org/0000-0002-2151-5818> (Y. Uludag)



Enhancing the adsorption of disinfection by-products onto activated carbon using TiO₂ nanoparticles

Rafat MOUSTAFA^{1,*}, Ahmed HESHAM²

 on the last page

¹ Department of Chemistry, Faculty of Science, Al-Azhar University, Cairo, Egypt

² Department of Chemistry, Faculty of Science, Suez Canal University, Ismailia, Egypt.

Received: 01 November 2018; Revised: 10 May 2019; Accepted: 11 May 2019

*Corresponding author e-mail: Rafat.moustafa@outlook.com

Citation: Moustafa, R.; Hesham, A. *Int. J. Chem. Technol.* 2019, 3 (1), 67-71.

ABSTRACT

The removal of contaminants from consumable waters by the traditional water treatment techniques is highly difficult. Disinfection of water alludes to the inactivation or pulverization of unsafe living pathogenic beings, which living in the water. Occurrence of disinfection by products (DBPs) during disinfection normally demonstrates lethal impacts on human health. Granular activated carbon (GAC) has the oldest history of decreasing of organic matters, but its role is reducing by time. TiO₂ is used to accelerate the removal of the DBPs. TiO₂ nanoparticles have good adsorption phenomena on the removal of those organic compounds at various pHs and temperatures and give good results. This study proved that TiO₂ nanoparticles enhanced the efficiency of GAC to remove DBPs from water. While the elimination of trihalomethanes (THMs), dichloroacetic acid (DCAA) and trichloroacetic acid (TCAA) using 0.5 g of GAC was determined as 61.7, 69.8 and 83.2% respectively, the elimination of them by 0.1 g of TiO₂ nanoparticles:GAC (1:1) was estimated as 100, 96 and 100%, respectively.

Keywords: Disinfection by-products, drinking water, nanoparticles TiO₂, THMs.

TiO₂ nanopartikülleri kullanılarak dezenfeksiyon yan ürünlerinin aktif karbon üzerine adsorpsiyonunun artırılması

ÖZ

Geleneksel su arıtma teknikleri ile kirletici maddelerin tüketilebilir suların uzaklaştırılması oldukça zordur. Suyun dezenfekte edilmesi, suda yaşayan, güvensiz yaşayan patojenik varlıkların etkisizleştirilmesine veya toz haline getirilmesine yol açar. Dezenfeksiyon sırasında dezenfeksiyon yan ürünlerin (DBP'lerin) oluşması normalde insan sağlığı üzerinde ölümcül etkiler göstermektedir. Granül aktif karbon (GAC) organik maddeleri azaltma da en eski geçmişine sahiptir, ancak onun rolü zamanla azalmaktadır. TiO₂, DBP'lerin uzaklaştırılmasını hızlandırmak için kullanılmaktadır. TiO₂ nanopartikülleri, çeşitli pH'larda ve sıcaklıklarda bu organik bileşiklerin uzaklaştırılmasında iyi adsorpsiyon olgusuna sahiptir ve iyi sonuçlar vermektedir. Bu çalışma, TiO₂ nanopartiküllerinin DBP'leri sudan uzaklaştırmak için GAC'nin etkinliğini arttırdığını ispatlamıştır. 0.5 g GAC kullanılarak trihalometanlar (THM'ler), dikloroasetik asit (DCAA) ve trikloroasetik asit (TCAA)'in eliminasyonu sırasıyla % 61.7, 69.8 ve 83.2 olarak belirlenirken, bunların 0.1 g TiO₂ nanopartikülleri:GAC (1:1) ile giderilmesi sırasıyla % 100, 96 ve % 100 olarak belirlenmiştir.

Anahtar Kelimeler: Dezenfeksiyon yan ürünler, içme suyu, nanopartiküller TiO₂, THMs.

1. INTRODUCTION

The disinfection procedure of drinking water plans to execute as well as inactivate pathogens may have the unintended outcome of framing disinfection by-products (DBPs).¹ At the point when the disinfectant free chlorine is utilized, more than 500 disinfections by-products (DBPs) have been recognized. Trihalomethanes (THMs)

and haloacetic acids (HAAs) account for a significant portion of the total DBPs formed in the reaction of free chlorine with natural organic matter (NOM) in water and are related with human health concerns.² They are directed in numerous nations according to world health organization (WHO) regulation. DBP formation can be overseen in metropolitan drinking water frameworks through antecedent expulsion and modification of disin-

fection parameters.³ Disinfection parameters that may affect DBP formation include concentration and type of disinfectant, pH, temperature and contact time. DBP precursors, especially those of THMs and HAAs, include humics (hydrophobic) and other compounds with UV254 absorbance.⁴ Upgraded coagulation is the best available technique that is economically for removal of DBP precursors (hydrophobic NOM), where coagulation parameters are acclimated to accomplish greatest DBP precursor removal.⁵ Advanced oxidation processes combining ozone, H₂O₂, and/or UV light are also emerging as effective ways to degrade contaminants in water including DBP precursors.⁶ TiO₂ nanomaterial is promising with its high potential and outstanding performance in photocatalytic environmental applications TiO₂ photo catalysis has been shown to reduce THM and HAA formation by degrading DBP precursors and also by providing disinfection capability.⁵ TiO₂ absorbs light and dissipates it through the excitation of an electron to its conduction band, creating what is termed an electron/hole pair.⁷ The electrons and holes can then directly degrade NOM in the water or can create reactive oxygen species (ROS) such as the hydroxyl and superoxide radicals that can then degrade NOM.⁸ TiO₂ requires low chemical and energy inputs; needing only UV light and the TiO₂ catalyst. Elimination of NOM and DBPs from drinking water using photo catalytically regenerable nanoscale adsorbents has been developed by Stephanie and others during 2019.⁹

2. EXPERIMENTAL

2.1. Materials

Pentane 99 % – sodium thiosulfate anhydrous 99% assay–sulfuric acid 99%. Methyl tert-butyl ether (MTBE) 99%-Ultra pure water. All chemicals, reagents and reference materials of THM, HAAs, and inorganic chemicals used were of high purity grade. They were obtained from Acustander Co., Riedel Co, Sigma Aldrich Co. and Fluka Co. GAC purchased from Calgon Carbon Corporation, particle sizes of 1.18–2.36 mm – Mexico, TiO₂ nano particles purchased from Reinste Co. -India, 99+%, 20 nm. Activated carbon loaded by TiO₂ nanoparticles were prepared by direct mixing in (1:1) ratio.

2.2. Methods

2.2.1. Determination of Trihalomethane (THM)

The THM species (chloroform, bromodichloromethane, dibromochloromethane, and bromoform) were measured according to EPA method 551^{10,11}, sample was collected in 40 ml brown glass bottle with screw cap, and then 15 ml was discarded from each sample bottle. A micro extraction technique was

used, for each bottle, 4 ml pentane were added, then the Sample bottle was shaken for 1 minute, and left for 10 minutes. About 1 ml from the organic upper layer was transfer into autosampler vial for injection using gas chromatography Gas chromatography Varian CP- 3800, split/spitless injector, Electron Captures Detector, CP-8400 Autosampler, and Galaxie Chromatography Data System for acquisition and data analysis have Primary column - CP SIL 5 CB 30 m X 0.32 mm, 0.25µm film thickness.¹² While the carrier gas was He of 99.999 % purity. Gas chromatography was performed under the following condition: - Inlet condition: split mode, initial temperature 250°C, pressure 33 psi, split ratio 20:100. The instrument was calibrated by using THM standards at 8, 16, 32, 48 and 64 µg l⁻¹ to construct calibration curve.

2.2.2. Determination of Haloacetic Acids (HAAs)

A micro extraction technique with methyl tert-butyl ether (MTBE) as the extraction solvent, the HAAs species (Dichloroacetic acid, Trichloroacetic acid) were measured according to EPA method 552.2, and GC chromatography was performed under the following condition: - Inlet condition: split mode, initial temperature 35°C, pressure 33 psi, split ratio 100:20 and Carrier gas type Helium.^{13,14} The instrument was calibrated by using HAA standards at 8, 16, 32, 48 and 64 µg l⁻¹ to construct calibration curve.

3. RESULTS AND DISCUSSION

Standard THM have been prepared equal concentration from all (Chloroform, bromodichloromethane, dibromochloromethane, bromoform), taken suitable volume as (100 ml) treated with granular activated carbon (GAC), shacking 20 min as duration at pH 6.9 and temperature 25°C, filtrated by micro filter have pore size 0.47 µm, extraction and injection on the system which determine DBPs, the removal of DBPs from treated water by using activated carbon in bench scale experiment found that an increase of GAC dosage have a significant in DBPs removal.

GAC has been used to adsorb the DBPs from water using 0.025, 0.05, 0.1 and 0.5 g. as different dose of adsorbent. The removal of THMs was 18.4, 26.3, 36.5 and 61.7% respectively while the removal of DCAA was 25.3, 31.7, 50.5 and 69.8% respectively and the removal of TCAA was 27.8, 43.6, 58.9 and 83.2% as shown in Table 1, Figures 1, 2 and 3 respectively.

Then 1:1 mixture of GAC and TiO₂ nanoparticles has been used to adsorb the DBPs from water using 0.02, 0.04, 0.06 and 0.1 g. as different dose of adsorbent, the results were as shown in Table 2. The removal of THMs was 34.8, 50.5, 83.3 and 100% respectively as shown in Figure 4, while the removal of DCAA was 27.8, 40.2, 63 and 96% respectively as shown in Figure 5, and the

Table 1. Removal % of DBPs using GAC

GAC (g)	THMs µg l ⁻¹	DCAA µg l ⁻¹	TCAA µg l ⁻¹	THMs Removal %	DCAA Removal %	TCAA Removal %
0	63	28.1	28	0.0	0.0	0.0
0.025	51.4	21	20.22	18.4	25.3	27.8
0.05	46.4	19.2	15.8	26.3	31.7	43.6
0.1	40	13.9	11.5	36.5	50.5	58.9
0.5	24.1	8.5	4.7	61.7	69.8	83.2

Table 2. Removal % of DBPs using GAC with TiO₂ nanoparticles

(1:1) GAC + TiO ₂ g.	THMs µg l ⁻¹	DCAA µg l ⁻¹	TCAA µg l ⁻¹	THMs Removal %	DCAA Removal %	TCAA Removal %
0	63	28.1	27.8	0.0	0.0	0.0
0.02	41.1	20.3	18.9	34.8	27.8	32.0
0.04	31.2	16.8	14.16	50.5	40.2	49.1
0.06	10.5	10.4	8.45	83.3	63.0	69.6
0.1	0	1.11	0	100.0	96.0	100.0

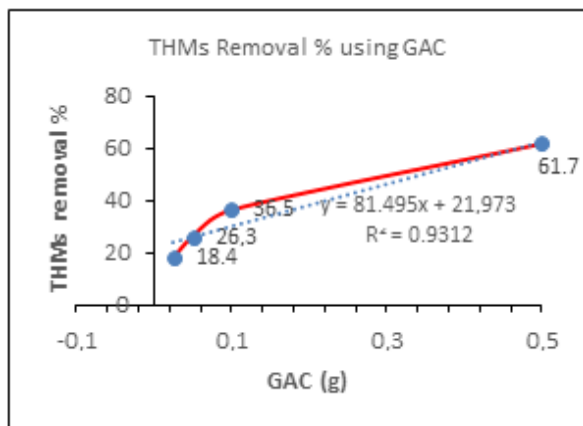


Figure 1. Removal % of THMs using GAC.

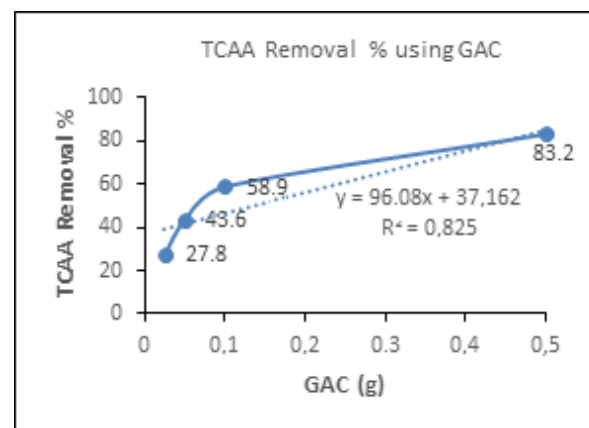


Figure 3. Removal % of TCAA using GAC.

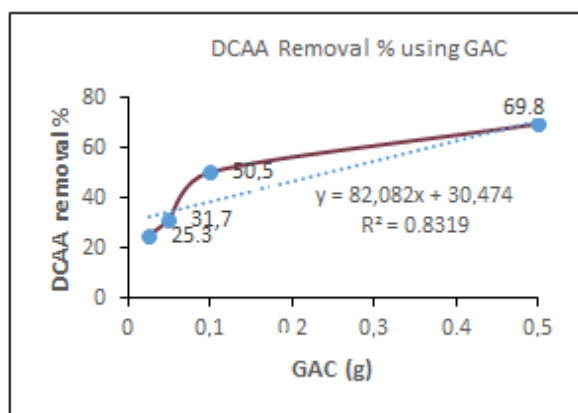


Figure 2. Removal % of DCAA using GAC.

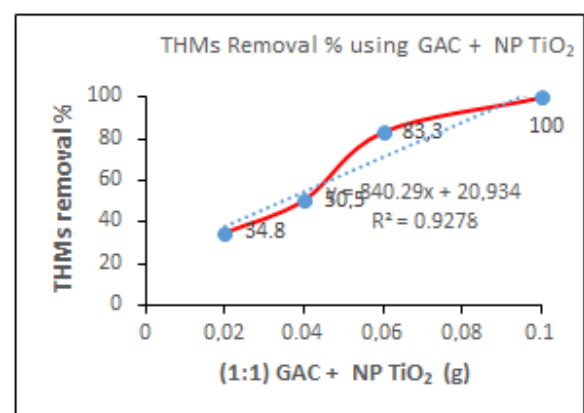


Figure 4. Removal % of THMs using (1:1) GAC + NP TiO₂.

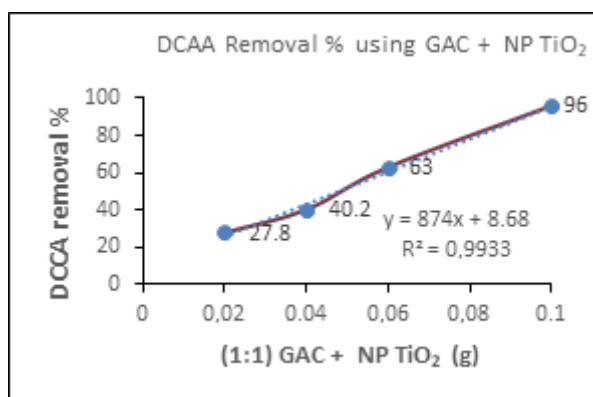


Figure 5. Removal % of DCAA using (1:1) GAC + NP TiO₂.

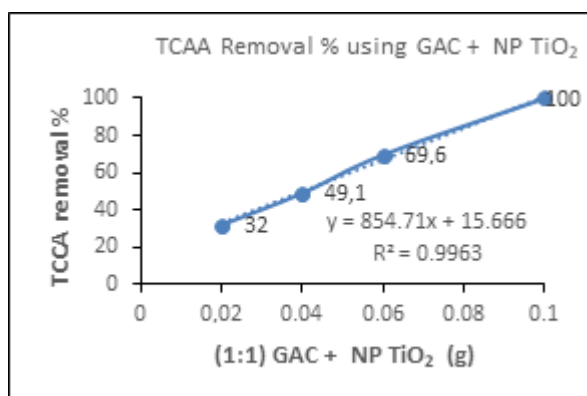


Figure 6. Removal % of TCAA using (1:1) GAC + NP TiO₂.

removal of TCAA was 32, 49.1, 69.6 and 100% respectively as shown in Figure 6. It is very clear that TiO₂ nanoparticles improved the efficacy of GAC in DBPs adsorption, this enhancement of the GAC activity will reduce the required QTY of GAC to adsorb the pollutants from the water.

4. CONCLUSIONS

The study proved that addition of TiO₂ nanoparticles improved the efficiency of the GAC to remove DBPs from water. The maximum removal of THMs, DCAA and TCAA was 61.7, 69.8 and 83.2% respectively using 0.5 g of GAC. The full removal of THMs and THAA was achieved using 0.1 g. (1:1) of GAC:TiO₂ nanoparticles, while the same QTY was achieved 96% removal of DCAA. This due to the properties of TiO₂ and its Photocatalysis / surface phenomenon, which consider a critical step in intervening in the effectiveness of photodegradation and adsorption of pollutants on the photocatalyst surface. Even the results of DBPs removal using 0.1 g. (1:1) of GAC:TiO₂ nanoparticles was very

promising we recommend further investigation about TiO₂ nanoparticles residues and its toxicity, also risk assessment for overall process for large scale applications.

Conflict of interests

Authors declare that there is no a conflict of interest with any person, institute, company, etc.

REFERENCES

- Rakness, K. L. *Ozone in drinking water treatment: process design, operation, and optimization*, 1st ed.; American Water Works Association, Colorado, USA, 2005.
- Alexandrou, L.; Meehan, B. J.; Jones, O. A. *Sci. Total Environ.* **2018**, 637, 1607-1616.
- Selvam, R.; Muniraj, S.; Duraisamy, T.; Muthunarayanan, V. *Appl. Water Sci.* **2018**, 8 (5):135.
- Fakour, H.; Lo, S. L. *Sci. Rep.* **2018**, 8(1), 5709.
- Tak, S.; Vellanki, B. P. J. *Water Health* **2018**, 16(5), 681-703.
- Sharma, A.; Ahmad, J.; Flora, S. J. S. *Environ. Res.* **2018**, 167, 223-233.
- Deb, A. Photocatalytic degradation of Benzophenone 3 in aqueous media under UV light irradiation. Master's Thesis, Lappeenranta University of Technology School of Engineering Science, Finland, 2018.
- Dong, R.; Cai, Y.; Yang, Y.; Gao, W.; Ren, B. *Accounts Chem. Res.* **2018**, 51(9), 1940-1947.
- Gora, S. L.; Andrews, S. A. *Chemosphere*, **2019**, 218, 52-63.
- US EPA, Method 551. Determination of chlorination disinfection by-products and chlorinated solvents in drinking water by liquid-liquid extraction and gas chromatography with electron-capture detection, Environmental Monitoring Systems Laboratory, Office of Research and Development, Cincinnati, 1990.
- Toroz, I.; Uyak, V. *Desalination* **2005**, 176 (1-3),
- Flickinger, B.; Hinshaw, J. V. GC instruments and accessories at the 54th Pittsburgh Conference. LC-GC: magazine of liquid and gas chromatography, 21 (5), 446-457, North America, 2003, 127-141.


DOI: <http://dx.doi.org/10.32571/ijct.481482>


E-ISSN:2602-277X

13. Saini, H. K. U.S. Patent No. 9,903,844. Washington, DC: U.S. Patent and Trademark Office, 2018.

14. Andersson, A.; Ashiq, M. J.; Shoeb, M.; Karlsson, S.; Bastviken, D.; Kylin, H. *Environ. Sci. Pollut. R.* **2019**, 26 (8), 7305-7314.

ORCID

 <https://orcid.org/0000-0003-3017-7037> (R. Moustafa)

 <https://orcid.org/0000-0002-0202-6664> (A. Hesham)



Rapid isolation of rosmarinic acid from *Ocimum basilicum* using flash chromatography

Hüseyin AKŞİT^{1,*}, Mehmet KEÇECİ², İbrahim DEMİRTAŞ³, Nusret GENÇ²

on the last page

¹Department of Analytical Chemistry, Faculty of Pharmacy, Erzincan Binali Yıldırım University, 24250, Erzincan, Turkey.

²Department of Chemistry, Faculty of Science and Art, Gaziosmanpaşa University, 60100, Tokat, Turkey

³ Department of Chemistry, Faculty of Science, Çankırı Karatekin University, 18400, Çankırı, Turkey

Received: 12 June 2019; Revised: 26 June 2019; Accepted: 27 June 2019

*Corresponding author e-mail: huseyinaksit@gmail.com

Citation: Akşit, H.; Keçeci, M.; Demirtaş, İ.; Genç, N. *Int. J. Chem. Technol.* 2019, 3 (1), 72-76.

ABSTRACT

In this study; it was aimed at the isolation of rosmarinic acid (RosA) from *Ocimum basilicum* (OB) with a selective extraction and rapid isolation technique using flash chromatography (FC). For this purpose, dried leaves of OB were extracted with n-hexane, dichloromethane, and methanol, respectively. The methanol extract (ME) was extracted with dichloromethane and ethyl acetate using separation funnel by suspending with water. The ethyl acetate layer was dried with anhydrous Na₂SO₄ and the solvent was evaporated to give a rosmarinic acid-rich extract. Then the ethyl acetate extract (EAE) was separated over silica gel column using FC, and thus RosA was isolated with high purity.

Keywords: Rosmarinic acid, flash chromatography, *Ocimum basilicum*.

Flash kromatografi kullanarak Reyhan bitkisinden rosmarinik asitin hızlı izolasyonu

ÖZ

Bu çalışmada, Reyhan bitkisinden (*Ocimum basilicum*) seçici bir ekstraksiyon ve hızlı izolasyon tekniği ile flash kromatografi kullanılarak rosmarinik asitin izolasyonu amaçlanmıştır. Bu amaçla; kurutulmuş reyhan yaprakları sırası ile hekzan, diklorometan ve metanol ile ekstrakte edildi. Methanol ekstraktı su ile çözülerek ayırma hunisinde diklorometan etil asetat ile ekstrakte edildi. Etil asetat fazı susuz Na₂SO₄ ile kurutuldu ve rosmarinik asitçe zengin ekstrakt vermek üzere çözücü evapore edildi. Daha sonra, etil asetat ekstraktı flash kromatografi kullanarak silika jel ile ayırma tabi tutuldu ve böylece rosmarinik asit yüksek saflıkta elde edildi.

Anahtar Kelimeler: Rosmarinic asit, flash kromatografi, Reyhan bitkisi.

1. INTRODUCTION

Natural products play an important role for drug discovery and development process due to their bioactive contents.¹⁻⁸ *Ocimum basilicum* belongs to the *Lamiaceae* family known to be rich sources of polyphenolic compounds, particularly phenolics acids.⁹ The plant extensively includes substances that high antioxidant activity due to the content of phenolic acids especially rosmarinic acid as a major constituent.¹⁰ RosA is an ester of caffeic acid and 3,4-dihydroxyphenyl lactic acid and is a widely occurring natural antioxidant in many plant kingdom with interesting biological activities e.g.

antitumor,¹¹ antidiabetic,¹² antioxidant,¹³ antiproliferative,^{14,15} antiviral and anti-inflammatory.¹⁶ Antioxidants were called as bioactive substances that prevent the formation of free radicals or neutralize free radicals in living organisms.^{17,18} To prevent oxidative degradation of food, synthetic antioxidants such as butylated hydroxyanisole (BHA), butylated hydroxytoluene (BHT), and tertbutylhydroquinone (TBHQ) are widely used in the food industry, but BHA and BHT are suspected of being responsible for liver damage and carcinogenesis.¹⁹ Therefore, the development and utilization of more effective antioxidants from the natural origin are desired.

2. EXPERIMENTAL

2.1. Plant material

Ocimum basilicum was cultivated in Gaziosmanpasa University Field Crops in Faculty Application sites, and harvested in July 2011.

2.2. Extraction of RosA

The air-dried aerial parts of plant material (400 g) were extracted sequentially with hexane, dichloromethane and methanol (every 24 hours, 4 Lx3). The methanol extract (13 g) suspended in water and partitioned between dichloromethane and water. The organic layer was removed. Then the water phase was partitioned between water and ethyl acetate. The ethyl acetate phase was separated and concentrated using evaporator after drying with anhydrous sodium sulfate to give slurry extract (6.30 g) (Figure 1).

2.3. Flash Chromatography conditions

Flash chromatography is a useful technique for separation in both natural and synthetic products. The constant flow rate of mobile phases and enabling

detection with UV detector increases the efficiency of separation and reproducibility when compared with common column chromatography techniques. A Combiflash companion Flash chromatography instrument was used for purification of RosA. The UV detector was set up at 330 nm. As a mobile phase, dichloromethane-ethyl acetate system was used with a linear gradient system at 10 mL/min flow rate. A manually packed with silica gel GF₂₅₄ glass column (5 cm X 50 cm, diameter X length) was used. The detected fractions at 330 nm were collected in 10 mL volumes.

2.4. LC-TOF-MS analysis

LC-TOF-HRMS analysis was performed using an Agilent 6210 LC-TOF instrument according to the method described previously.²⁰ Briefly; elution was performed using Poroshell column 120 EC-C18 (3.0 × 50 mm, 2.7 μm I.D.). The mobile phases were water with 0.1% formic acid and 5 mM ammonium format (Solvent A) and acetonitrile (solvent B) with 0.7 mL/min flow rate. The gradient program was used as follows: 0–1 min, 10% B; 1–8 min, 10% B; 8–11.1 min, 95% B; 11.1–13 min, 10% B; 13–14 min, 10% B. TOF analyses were carried out in negative ion mode; gas temperature, 325 °C and column temperature, 35 °C; drying gas flow, 0.7 ml/min; fragmentor voltage, 175 V.

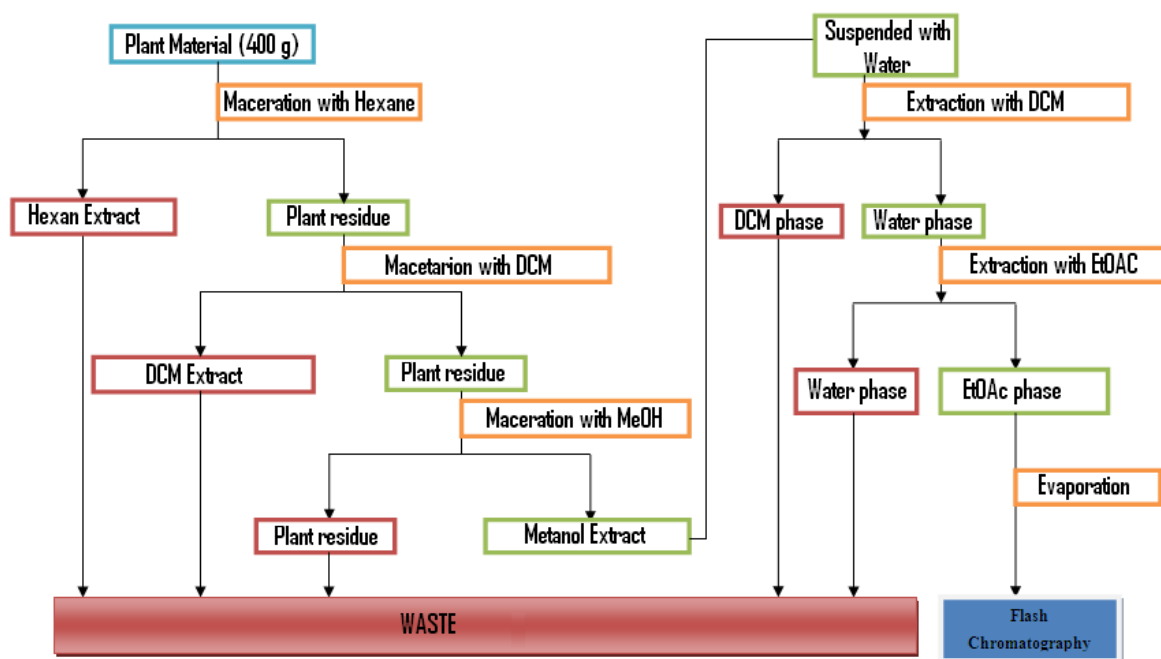


Figure 1. Extraction flowchart of RosA from *O. basilicum*.

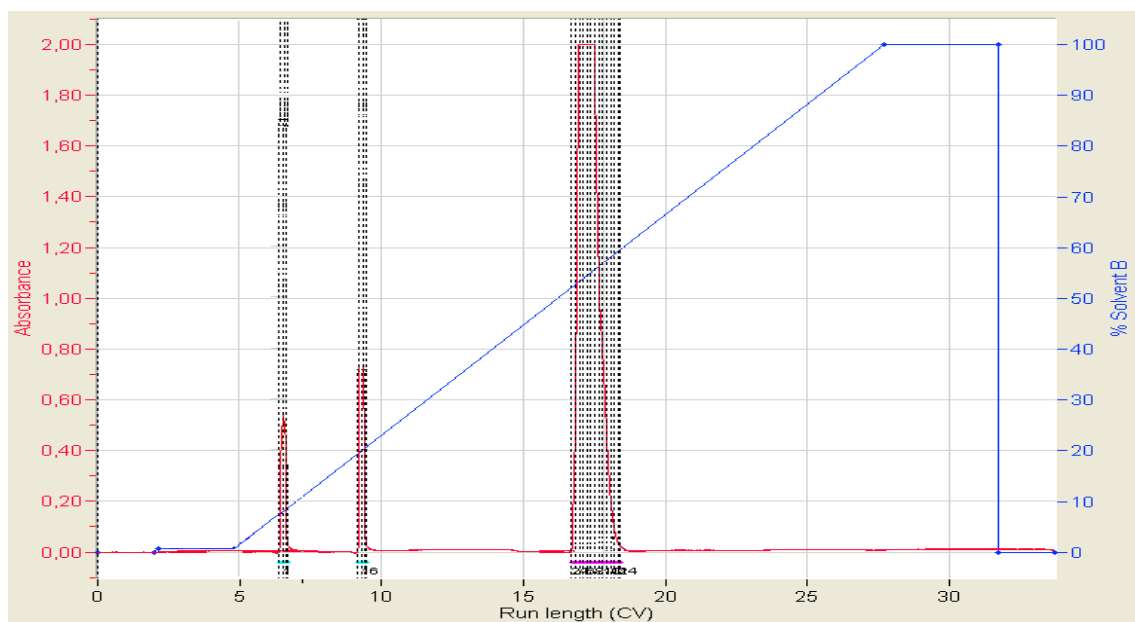


Figure 2. Flash chromatography chromatogram of the ethyl acetate phase.

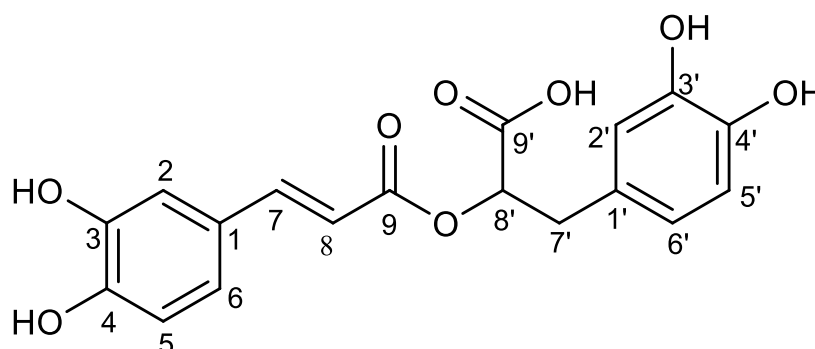


Figure 3. Chemical structure of RosA.

3. RESULTS AND DISCUSSION

The collected fractions during 16-18 CV (column volume) were combined and evaporated to give yellowish amorphous solid (The main peak observed on LC-chromatogram: See Figure 2).

20 mg of collected fractions were solved in DMSO- d_6 and recorded 1H and ^{13}C -NMR spectra. The data obtained as follows:

1H -NMR (400 MHz, DMSO- d_6) δ_H : d 7.46 (*d*, 1H, H-7, $J=15.8$ Hz), 7.06 (*d*, 1H, H-2, $J=1.4$ Hz), 7.02 (*d*, 1H, H-6, $J=8.12$ Hz), 6.79 (*d*, 1H, H-5, $J=8.12$ Hz), 6.69 (*d*, 1H, H-2', $J=1.5$ Hz), 6.54 (*d*, 1H, H-5', $J=7.92$ Hz), 6.65 (*d*, 1H, H-6', $J=7.92$ Hz), 6.24 (*d*, 1H, H-8, $J=15.8$ Hz),

5.08 (*dd*, 1H, H-8', $J=10$ Hz, $J=2.8$ Hz), 2.98 (*dd*, 1H, H-7a', $J=10.1$ Hz, $J=1.10$ Hz), 2.98 (*d*, 1H, H-7b', $J=10$ Hz); ^{13}C -NMR (100 MHz, DMSO- d_6) δ_C : d 171.33 (C-9'), 166.43 (C-9), 146.07 (C-4), 149.10 (C-3), 146.39 (C-7), 144.50 (C-3'), 145.41 (C-4'), 127.7 (C-1'), 125.9 (C-1), 122.02 (C-6), 115.85 (C-6'), 117.17 (C-2'), 116.23 (C-5), 120.53 (C-5'), 115.28 (C-2), 113.66 (C-8), 73.18 (C-8'), 36.61 (C-7'). According to 1H and ^{13}C -NMR data, the compound identified as RosA with good agreement with data given in the literature.^{21,22}

The LC-TOF-HRMS chromatogram of crude ethyl acetate extract, isolated RosA and standard RosA is given in Figure 4. LC-TOF analysis showed that the molecular weight of RosA was 360.0848 g/mol (calc. for $C_{18}H_{16}O_8$:360.0845 g/mol) with high purity.

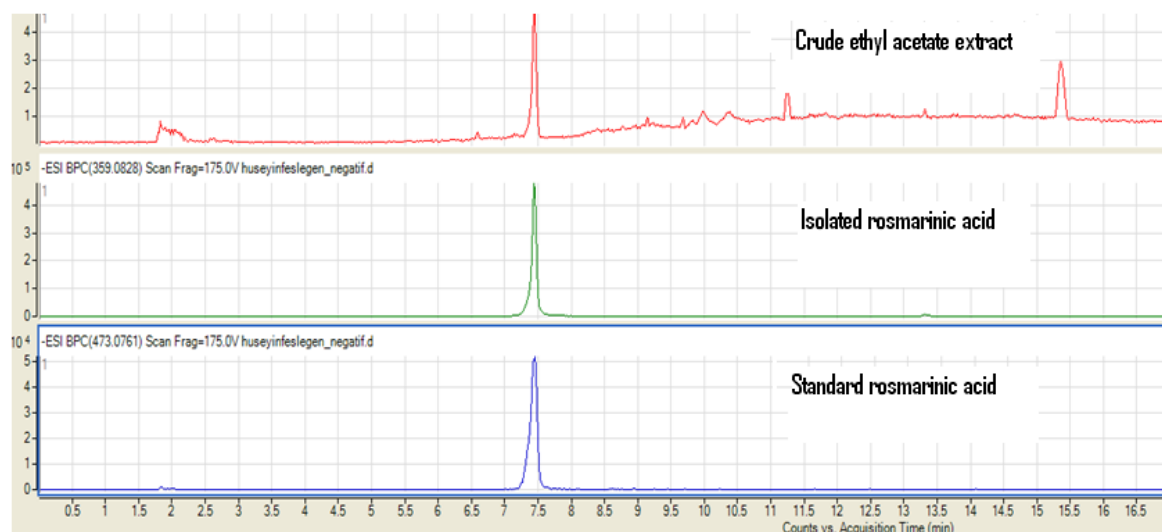


Figure 4. Chromatogram of TOF-LC/MS instrument of crude ethyl acetate extract, isolated RosA and standard RosA.

4. CONCLUSIONS

In this study, rosmarinic acid was extracted from *Ocimum basilicum* using a selective extraction technique. Purification of RosA was achieved by using flash chromatography. The extraction and purification process can be suggested to the isolation of RosA rapidly and efficiently from natural sources.

Conflict of interests

Authors declare that there is no a conflict of interest with any person, institute, company, etc.

REFERENCES

- Erenler, R.; Telci, I.; Elmastaş, M.; Akşit, H.; Gül, F.; Tüfekçi, A. R.; Kayır, Ö. *Turk. J. Chem.* **2018**, 42(6), 1695-1705.
- Karan, T.; Erenler, R. *Trop. J. Pharm. Res.* **2018**, 17(10), 1977-1982.
- Erenler, R.; Demirtaş, I.; Karan, T.; Gül, F.; Kayır, O.; Karakoc, O. C. *Trends Phytochem. Res.* **2018**, 2(2), 91-96.
- Karan, T.; Yıldız, I.; Aydın, A.; Erenler, R.; *Rec. Nat. Prod.* **2018**, 12(3), 273-283.
- Karan, T.; Erenler, R. *Pharmacogn. Mag.* **2017**, 13, 723-725.
- Güzel, A.; Akşit, H.; Elmastaş, M.; Erenler, R. *Pharmacogn. Mag.* **2017**, 13(50), 316-320.
- Erenler, R.; Meral, B.; Şen, Ö.; Elmastaş, M.; Aydın, A.; Eminağaoğlu, O.; Topçu, G. *Pharm. Biol.* **2017**, 55(1), 1646-1653.
- Erenler, R.; Şen, Ö.; Şahin Yağlıoğlu, A.; Demirtaş, I.; *Comb. Chem. High T. Scr.* **2016**, 19(1), 66-72.
- Capecka, E.; Mareczek, A.; Leja, M. *Food Chem.* **2005**, 93, 223-226.
- Kwee, E. M.; and Niemeyer, E. D. *Food Chem.* **2011**, 128, 1044-1050.
- Sharmila, R.; Manoharan, S. *Indian J. Exp. Biol.* **2012**, 50, 187-194.
- Jiang, W. L.; Xu, Y.; Zhang, S. P.; Hou, J.; Zhu, H. B. *Basic Clin. Pharmacol. Toxicol.* **2012**, 110, 390-395.
- Perez-Tortosa, V.; Lopez-Orenes, A.; Martinez-Perez, A.; Ferrer, M.A.; Calderon, A.A. *Food Chem.* **2012**, 130, 362-369.
- Erenler, R.; Şen, Ö.; Yıldız, I.; Aydın, A. *Rec. Nat. Prod.* **2016**, 10(6), 766-770.
- Zhang, J. J.; Wang, Y. L.; Feng, X. B.; Song, X. D.; Lu, W.B. *Biol. Pharm. Bull.* **2011**, 34, 343-348.
- Swarup, V.; Ghosh, J.; Ghosh, S.; Saxena, A.; Basu, A. *Antimicrob. Agents Ch.* **2007**, 51, 3367-3370.
- Erenler, R.; Yılmaz, S.; Akşit, H.; Sen, O.; Genç, N.; Elmastaş, M.; Demirtaş, İ. *Rec. Nat. Prod.* **2014** 8(1), 32-36.

18. Erenler, R., Telci, I., Ulutaş, M., Demirtaş, I., Gül, F., Elmastaş, M., Kayır, Ö. *J. Food Biochem.* **2015**, 39(5), 622-630.


19. Grice, H. C. *Food Chem. Toxicol.* **1986**, 24, 1127-1130.

20. Demirtaş, İ.; Erenler, R.; Elmastaş, M.; Göktaşoğlu, A. *Food Chem.* **2013**, 136, 34-40.

21. Woo E. R.; Piao, M. S. *Arch. Pharm. Res.* **2007**, 27, 173-176.

22. Wang, M. F.; Li, J. G.; Rangarajan, M.; Shao, Y.; LaVoie, E. J.; Huang T.C.; Ho, C. T. *J. Agr. Food Chem.* **1998**, 46, 4869-4873.

ORCID

 <https://orcid.org/0000-0002-1509-851X> (H. Akşit)

 <https://orcid.org/0000-0002-0420-5316> (M. Keçeci)

 <https://orcid.org/0000-0001-8946-647X> (İ. Demirtaş)

 <https://orcid.org/0000-0003-3685-1344> (N. Genç)